TITLE:

Studies on Novel Light Emitting Materials Based on Random Systems(Dissertation_全文)

AUTHOR(S):

Meng, Xiangeng

CITATION:

Meng, Xiangeng. Studies on Novel Light Emitting Materials Based on Random Systems. 京都大学, 2008, 博士(工学)

ISSUE DATE:

2008-09-24

URL:

https://doi.org/10.14989/doctor.k14165

RIGHT:

京都大学学術情報リポジトリ
KURENAI 紅
Kyoto University Research Information Repository

Studies on Novel Light Emitting Materials Based on Random Systems

Xiangeng Meng

2008

Department of Material Chemistry,
Graduate School of Engineering,
Kyoto University

General introduction

Light emitting materials have attracted considerable attention because they are widely used in displays, telecommunications, medicine, storage, and so on.[1-6] The light emitting materials generally consist of light emitting centers and host materials; the former includes rare-earth ions (REs), transition metal ions (TMs), semiconductors, and so on,[7-19] and the latter can be categorized into amorphous and crystalline materials.[20-26] Luminescent properties of TMs are very sensitive to environmental configurations of anions and ligands so that the luminescence is usually observed as a broad emission spectrum; thus, TMs have been widely used in tunable broad laser sources and fiber amplifiers.[27-32] Glasses are important host materials for REs, TMs, semiconductor quantum dots, and laser dyes.[33-36] Glasses doped with the above-mentioned light emitting centers have found many commercial applications to date, such as optical fibers, lasers, displays, and so on. Among TMs, there is a specific group which has vacant d orbitals; herein they are called d^0 ions. The d^0 ions described in this thesis are Ti^{4+}, Zr^{4+}, Nb^{5+}, Ta^{5+}, Mo^{6+}, and W^{6+}. Their electronic configurations are Ti^{4+}: $[Ar]3d^0$; Zr^{4+}: $[Kr]4d^0$; Nb^{5+}: $[Kr]4d^0$; Ta^{5+}: $[Xe]4f^{14}5d^0$; Mo^{6+}: $[Kr]4d^0$, and W^{6+}: $[Xe]\ 4f^{14}5d^0$. Crystalline compounds including d^0 ions have arrested much attention in recent years since they demonstrate intense nonlinearity and attractive luminescent properties.[37-41] However, little attention has been paid to d^0 ion-doped glass materials although glass materials have the above-mentioned advantageous points. In this work, the author has prepared d^0 ion-doped glass materials and systematically examined their luminescent properties to search for novel light emitting materials based on random systems.

Lasers have played an important role since Maiman developed the first ruby laser in 1960.[29] Lasers consist of three important components, i.e., working medium, oscillation cavity, and pump source. Such lasers are regular lasers for which lasing

modes are determined by the oscillation cavity instead of working media. Light scattering centers should be avoided in regular lasers since they will scatter light out of the oscillation cavity and degrade laser performance. However, in 1967, Russian scientists predicted that a novel laser source based on light scattering would be possible if the strength of light scattering could be manipulated to some extent.[42] This prediction has been evidenced experimentally and becomes a very hot topic nowadays.[43-83] The term "random laser" was first introduced by Lagendijk and Wiersma in 1995 when discussing the work of Lawandy.[53,54] Random lasers are designed more simply when compared with regular lasers, while a high gain is expected in such lasers. Random lasers not only find potential applications in displays, lasers, sensors, and so on but also bring about a very important physical topic: the Anderson localization of light, owing to which random lasers have received considerable attention nowadays.[84-86] The key point of random lasers for practical applications is whether a coherent feedback is involved or not since the emergence of a coherent feedback implies a high optical gain. The feedback in random lasers is given by multiple scattering instead of reflection unlike the regular lasers so that the scattering strength of random media is crucial to types of feedback. Generally, weak scattering strength results in a gradual narrowing of emission spectrum with a linewidth in several nanometers scale, while strong scattering strength gives rise to discrete sharp peaks with a linewidth less than one nanometer that are superimposed on a broad amplified spontaneous emission band. In order to achieve the coherent feedback, dielectric materials having high refractive index (e.g. GaP, TiO_2, and ZnO) are usually utilized because large difference in refractive index between scattering centers and environmental medium significantly contributes to the strong scattering according to the Mie scattering theory.[87-89] However, the strong scattering of dielectrics also results in a giant loss because the material loses transparency. The pump light incident on strong scattering media is mostly scattered instead of being absorbed to excite the gain medium, leading to a drastic reduction of the pump efficiency.[66] Because of the above demerit

of dielectrics, it is necessary to search for new random lasing systems that combine high gain with high transparency in emission wavelength region. The author is interested in metal nanostructures since they take the following advantages over dielectrics in applications of random lasers. Firstly, metal nanostructures possess much larger scattering strength than dielectric structures when they have the same dimensions as each other.[81-83] Secondly, they can spatially confine light near the metal surface and provide high gain for lasing oscillation.[81-83] Therefore, metal nanostructures are potential candidates for random lasers with high gain. However, little attention has been paid to the metal nanostructures in the field of random lasers. In this thesis, the author describes the development of novel random lasing systems based on metal nanostructures and observations of distinct laser actions with coherent feedback for the first time.

In Chapter 1, the author briefly introduces fundamentals of interactions of light with matters that include light emission and absorption, multiphoton-excited fluorescence, light scattering, random lasers, and surface plasmon resonance. Light scattering can be divided into single scattering and multiple scattering. The history, development, and applications of random lasers, as well as fundamentals of light transport in amplifying random media, the effect of scattering strength on random lasers, and how to tell the coherent feedback are depicted.

In Chapter 2, the author describes the sample preparation, characterization, and fluorescence properties of glasses doped with d^0 ions. Such glasses can be readily prepared by using a conventional melt quenching method in air. Optical absorption, fluorescence, electron spin resonance, and fluorescence decays are used to characterize optical properties of d^0 ion-doped glasses. Two important observations are obtained in this work: tunable visible emissions caused by ultraviolet light excitation and those induced by a near-infrared femtosecond pulsed laser excitation. The emission wavelength strongly depends on the kinds of d^0 ions. The profile of emission spectrum obtained by excitation with ultraviolet light is almost identical to that excited by the

near-infrared femtosecond laser for Ta^{5+}, Ti^{4+}, and Nb^{5+}-doped glasses. However, it is not the case for the other d^0 ions. The effect of host materials on the optical properties of Ta^{5+} is examined. The profiles of optical absorption and emission spectra are maintained but the emission intensity is varied. The mechanism for the observations of tunable visible emissions is discussed and a model of d^0 energy state responsible for such observations is proposed.

In Chapter 3, the author describes the preparation and characterization of various metal nanostructures. Anisotropic silver nanoparticles and nanoprisms are prepared through solution routes and polymer films in which anisotropic silver nanoparticles and nanoprisms are dispersed are prepared by spin coating or cell-casting technique. An *in situ* route is introduced to prepare polymer films containing superfine silver nanoparticles, in which the distribution of silver nanoparticles could be controlled by the annealing time, annealing temperature, and initial concentrations of Ag^+ ions. The samples are characterized by optical absorption, X-ray diffraction, scanning electron microscopy, and transmission electron microscopy.

In Chapter 4, the author describes random laser operation of three above-mentioned samples, i.e., polymer films containing anisotropic silver nanoparticles, polymer films containing silver nanoprisms, and *in situ* synthesized polymer films in which superfine silver nanoparticles are dispersed. All the samples in this study are highly transparent so that the optical excitation is efficient. In other words, all the samples operate in rather weakly scattering regimes; nevertheless, random lasers with coherent feedback are observed for all the samples. The effects of pump energy, the spot size of pump beam on the sample, concentration of dye, and number density of silver nanoparticles, on properties of random lasers are discussed. The incident angular dependence of laser emission is examined. The Fourier transform of the spectrum is utilized to analyze the oscillation cavity length for lasing. The results indicate that the scattering mean free path is much larger than the oscillation cavity length, which has been rarely reported thus far. The mechanism responsible for the

coherent laser emission observed in this work is discussed. The author surmises that the lasing oscillation is closely associated with the surface plasmon resonance of silver nanostructures.

Finally, the author briefly summarizes the experimental results and discussions in this thesis, including glasses doped with d^0 ions and random lasers induced by metal nanostructures.

References

1. G. Blasse and B. C. Grabmaier, *Luminescent materials*, Springer-Verlag Berlin, Heidelberg, 1994.
2. S. Tanabe and X. Feng, *Appl. Phys. Lett*. **77**, 818 (2000).
3. K. Hirao, S. Todoroki, D. Cho, and N. Soga, *Opt. Lett*. **18**, 1586 (1993).
4. K. Hirao, *J. Non-Cryst. Solids* **196**, 16 (1996).
5. J. Qiu, K. Miura, T. Suzuki, T. Mitsuyu, and K. Hirao, *Appl. Phys. Lett*. **74**, 10 (1999).
6. L. Hood, J. Heath, M. Phelps, and B. Lin, *Science* **306**, 640 (640).
7. B. Judd, *Phys. Rev.* **127**, 750 (1962).
8. G. Ofelt, *J. Chem. Phys*. **37**, 511 (1962).
9. K. Machida, G. Adachi, and J. Shiokawa, *J. Lumin*. **21**, 101 (1979).
10. K. Wei, D. P. Machewirth, J. Wenzel, E. Snitzer, and G. H. Sigel Jr., *Opt. Lett*. **19**, 904 (1994).
11. V. K. Tikhomirov, K. Iakoubovskii, P. W. Hertogen, and G. J. Adriaenssens, *Appl. Phys. Lett*. **71**, 2740 (1997).
12. J. Y. Allain, M. Monerie, and H. Poignant, *Electron. Lett*. **25**, 1660 (1989).
13. T. Izumitani, H. Toratani, and H. Kuroda, *J. Non-Cryst. Solids*, **47**, 87 (1982).
14. J. Qiu, N. Sugimoto, Y. Iwabuchi, and K. Hirao, *J. Non-Cryst. Solids* **209**, 200 (1997).

15. A. G. Okhrimchuk and A. V. Shstakov, *Phys. Rev. B* **61**, 988 (2000).
16. S. E. Stokowski and A. L. Schawlow, *Phys. Rev.* **178**, 457 (1969).
17. M. H. Huang, S. Mao, H. Feick, H. Yan, Y. Wu, H. Kind, E. Weber, R. Russo, and P. D.Yang, *Science* **292**, 1897 (2001).
18. F. A. Ponce and D. P. Bour, *Nature (London)* **386**, 351 (1997).
19. Z. Y. Tang, N. A. Kotov, and M. Giersig, *Science* **297**, 237 (2002).
20. J. A. Mares, M. Nikl, K. Nitsch, N. Solovieva, A. Krasnikov, and S. Zazubovich, *J. Lumin*. **94-95**, 321 (2001).
21. M. F. Churbanov, I. V. Scripachev, V. S. Shiryaev, V. G. Plotnichenko, S. V. Smetanin, E. B. Kryukova, Y. N. Pyrkov, and B. I. Galagan, *J. Non-Cryst. Solids* **326-327**, 301 (2003).
22. J. H. Yang, L. Y. Zhang, L. Wei, S. X. Dai, L. L. Hu, and Z. H. Jiang, *J. Appl. Phys*. **95**, 3020 (2004).
23. H. Jeong, K. Oh, S. R. Han, and T. F. Morse, *Chem. Phys. Lett*. **367**, 507 (2003).
24. X. L. Zou, A. Shikida, H. Yanagita, and H. Toratani, *J. Non-Cryst. Solids* **181**, 100 (1995).
25. M. J. Weber, M. Bass, and G. A. Demars, *J. Appl. Phys*. **42**, 301 (1971).
26. G. A. Kumar, R. Riman, and E. Snitzer, *J. Appl. Phys*. **95**, 40 (2004).
27. H. Eilers, W. M. Dennis, W. M. Yen, S. Kuck, K. Peterman, G. Huber, and W. Jia, *IEEE J. Quan. Electron*. **29**, 2508 (1993).
28. C. Y. Lo, K. Y. Huang, J. C. Chen, C. Y. Chuang, C. C. Lai, S. L. Huang, Y. S. Lin, and P. S. Yeh, *Opt. Lett*. **30**, 129 (2005).
29. T. H. Maiman, *Nature (London)* **187**, 493 (1960).
30. M. J. Weber, M. Bass, K. Andringa, R. R. Monchamp, and E. Comperch, *Appl. Phys. Lett*. **15**, 342 (1969).
31. L. F. Johnson, R. E. Dietz, and H. J. Guggenheim, *Appl. Phys. Lett*. **5**, 21 (1964)
32. L. F. Johnson and H. J. Guggenheim, *J. Appl. Phys*. **38**, 4837 (1967)
33. D.R. Simons, A.J. Faber, and H. de Waal, *J. Non-Cryst. Solids*, **185**, 283 (1995)

34. C. R. Mendonca, B. J. Costa, Y. Messaddeq, and S. C. Zilio, *Phys. Rev. B*, **56**, 2483 (1997)
35. Y. L. Yu, Y. S. Wang, D. Q. Chen, P. Huang, E. Ma, and F. Bao, *Nanotechnology*, **19**, 055711 (2008).
36. L. Iizoo and C. Josephine, United States Patent 5329540.
37. P. S. Pizani, E. R. Leite, F. M. Pontes, E. C. Paris, J. H. Rangel, E. J. H. Lee, E. Longo, P. Delega, and J. A. Varela, *Appl. Phys. Lett*. **77**, 824 (2000).
38. M. Gaft. L. Nagli, G. Waychunas, and D. Weiss, *Phys. Chem. Minerals* **31**, 365 (2004).
39. Y. Takahashi, K. Kitamura, Y. Benino, T. Fujiwara, and T. Komatsu, *Appl. Phys. Lett*. **86**, 091110 (2005).
40. E. Orhan, J. A. Varela, A. Zenatti, M. F. C. Gurgel, F. M. Pontes, E. R. Leite, and E. Longo, *Phys. Rev. B* **71**, 085113 (2005).
41. Y. Takahashi, K. Kitamura, N. Iyi, and S. Inoue, *Appl. Phys. Lett*. **88**, 151913 (2006).
42. R. V. Ambartsumian, N. G. Basov, P. G. Kryukov, and V. S. Letokhov, *IEEE J. Quantum Electron. QE*-**2**, 442, (1966).
43. C. Genet and T. W. Ebbesen, *Nature (London)* **445**, 39 (2007).
44. A. J. Cox, A. J. DeWeerd, and J. Linden, *Am. J. Phys*. **70**, 620 (2002).
45. P. B. Johnson and R. W. Christy, *Phys. Rev. B* **6**, 4370 (1972).
46. V. P. Drachev. U. K. Chettiar, A. V. Kildishev, H. K. Yuan, W. Cai, and V. M. Shalaev, *Opt. Exp.* **16**, 1186 (2008).
47. H. Cao, *Lasing in disordered media*, in "Progress in Optics", ed. E. Wolf, North-Holland, 2003, Vol. **45**.
48. V. S. Letokhov, *Zh. Eksp. Teor. Fiz*. **53**, 1442 (1967).
49. V. M. Markushev, V. F. Zolin, and Ch. M. Briskina, *Zh. Prikl. Spectroscopy*. **45**, 847 (1986).
50. R. V. Ambartsumyan, P. G. Kryukov, and V. S. Letkhov, *Sov. Phys. JETP*, **24**, 1129

(1967).

51. V. M. Markushev, V. F. Zolin, and C. M. Briskina, *Sov. J. Quantum Electron*. **16**, 281 (1986).
52. V. F. Zolin, *J. Alloys and Compounds*, **300-301**, 214 (2000).
53. N. M. Lawandy, R. M. Balachandran, A. S. L. Gomes, and E. Saultravioletain, *Nature (London)* **368**, 436 (1994).
54. D. S. Wiersma, M. P. van Albada, and A. Lagendijk, *Nature (London)* **373**, 203 (1995).
55. D. S. Wiersma and A. Lagendijk, *Phys. Rev. E* **54**, 4256 (1996).
56. H. Cao, Y. G. Zhao, S. T. Ho, E. E. Seeling, Q. H. Wang, and R. P. H. Chang, *Phys. Rev. Lett*. **82**, 2278 (1999).
57. S. V. Frolov, W. Gellerman, M. Ozaki, K. Yoshino, and Z. V. Vardeny, *Phys. Rev. Lett*. **78**, 729 (1997).
58. H. Cao, J. Y. Xu, S. H. Chang, S. T. Ho, E. W. Seeling, X. Liu, and R. P. H. Chang, *Phys. Rev. Lett*. **84**, 5584 (2000).
59. H. Cao, Y. Ling, J. Y. Xu, C. Q. Cao, and P. Kumar, *Phys. Rev. Lett*. **86**, 4524 (2001).
60. K. L. van der Molen, R. W. Tjerkstra, A. P. Mosk, and A. Lagendijk, *Phys. Rev. Lett*. **98**, 143901 (2007).
61. G. van Soest, F. J. Poelwijk, R. Sprik, and A. Lagendijk, *Phys. Rev. Lett*. **86**, 1522 (2001).
62. A. Yu. Zyuzin, *Europhys. Lett*. **26**, 517 (1994).
63. S. Mujumdar and H. Ramachandran, *Opt. Commun*. **176**, 31 (2000).
64. X. Jiang and C. M. Soukoulis, *Phys. Rev. Lett*. **85**, 70 (2000).
65. C. W. J. Beenakker, *Phys. Rev. Lett*. **81**, 1829 (1998).
66. A. L. Burin, H. Cao, and M. A. Ratner, *IEEE J. Sel. Top. Quantum Electron*. **9**, 124 (2003).
67. A. V. Akimov, A. Mukherjee, C. L. Yu, D. E. Chang, A. S. Zibrov, P. R. Hemmer, H.

Park, and M. D. Lukin, *Nature (London)* **450**, 402 (2007)

68. Y. Ling, H. Cao, A. L. Burin, M. A. Ratner, X. Liu, and R. P. H. Chang, *Phys. Rev. A* **64**, 063808 (2001).
69. R. C. Polson, A. Chipouline, and Z. V. Vardeny, *Adv. Mater*. **13**, 760 (2001).
70. R. C. Polson and Z. V. Vardeny, *Phys. Rev. B* **71**, 045205 (2005).
71. R. C. Polson and Z. V. Vardeny, *Phys. B* **338**, 219 (2003).
72. S. John, Localization of light (in dielectric microstructures), *Phys. Today* **44**, 32 (1991).
73. M. P. van Albada and A. Lagendijk, *Phys. Rev. Lett*. **55**, 2692 (1985).
74. A. Z. Genack and N. Garcia, *Phys. Rev. Lett*. **55**, 2696 (1985).
75. D. S. Wiersma, P. Bartolini, A. Lagendijk, and R. Righini, *Nature (London)* **390**, 671 (1997).
76. W. Sha, C. H. Liu, and R. Alfano, *Opt. Lett*. **19**, 1922 (1994).
77. H. Cao, J. Y. Xu, S. H. Chang, and S. T. Ho, *Phys. Rev. B* **61**, 1985 (2000).
78. K. Geetha, M. Rajesh, V P N Nampoori, C P G Vallabhan, and P Radhakrishnan, *J. Opt. A: Pure Appl. Opt*. **6**, 379 (2004).
79. K. Ishikawa and T. Okubo, *Appl. Phys. Lett*. **83**, 2536 (2003).
80. M. A. Noginov, H. J. Caulfield, N. E. Noginova, and P. Venkateswarlu, *Opt. Commun.* 118, 430 (1995).
81. G. D. Dice, S. Mujumdar, and A. Y. Elezzabi, *Appl. Phys. Lett*. **86**, 131105 (2005).
82. O. Popov, A. Zilbershtein, and D. Davidov, *Appl. Phys. Lett*. **89**, 191116 (2006).
83. N. Lawandy, *Appl. Phys. Lett*. **85**, 5040 (2004).
84. A. Yamilov, X. Wu, H. Cao, and A. L. Burin, *Opt. Lett*. **30**, 2430 (2005).
85. H. Cao, Optics & Photonics News, January 2005.
86. H. Cao, *J. Phys. A: Math. Gen*. **38**, 10497 (2005).
87. D. S. Wiersma, M. P. van Albada, B. A. Tiggelen, and A. Lagendijk, *Phys. Rev. Lett*. **74**, 4193 (1995).
88. K. L. van der Molen, R. W. Tjerkstra, A. P. Mosk, and A. Lagendijk, *Phys. Rev. Lett*.

98, 143901 (2007).

89. G. van Soest, F. J. Poelwijk, R. Sprik, and A. Lagendijk, *Phys. Rev. Lett*. **86**, 1522 (2001).
90. S. F. Yu and E. S. P. Leong, *IEEE J. Quantum Electron*. **40**, 1186 (2004).

Chapter 1 Interaction of Light with Random Media

This chapter mainly describes light emission and absorption, light scattering, defects in glasses, random lasers, and surface plasmon resonance.

1.1 Emission and absorption of light

A matter comprises atoms composed of nuclear and electrons. Electrons move along various orbitals with specific energy levels, as initially suggested by Bohr. The orbital with the lowest energy is called the ground state, in which an electron is stable. In contrast, the orbitals with higher energies are called the excited states, in which an electron lives for a short period and eventually relaxes to the ground state. Now supposing that a beam of monochromatic light with photon energy hv is incident on the matter and the photon satisfies $hv=E_2-E_1$, where E_1 and E_2 are the energies of the ground and excited states, respectively, the electron will be excited from E_1 to E_2 after absorbing one photon energy hv. One can say that light is absorbed in this process. The light absorption in a medium obeys the Beer-Lambert law $I=I_0\exp(-\alpha z)$, where z is the light pass in the medium, I is the light intensity at z, I_0 is the incident light intensity, and α is the absorption coefficient. Namely, the light intensity I exponentially decreases against the length of light path z in the medium.

A period for which an electron occupies the E_2 state is rather short; therefore, the electron in the E_2 state quickly relaxes to E_1. The way to transfer one electron from E_2 to E_1 can be radiative or nonradiative process, the former refers to energy loss via lattice vibration, while the latter is characterized by output of a photon. The radiative process corresponds to light emission. The process to excite the electron to one excited state is called excitation. The excitation process can be achieved via many routes such as electromagnetic wave, energetic electrons, electric filed, mechanical energy, X-rays, and so on. The corresponding luminescences are called photoluminescence,

cathodoluminescence, electroluminescence, and X-ray luminescence. In principle, this radiative transition should follow the energy conservation. That is, the energy of the emitted photon should satisfy $h\nu=E_2-E_1$. The concept of light absorption and emission is presented in Fig. 1.1. An atom excited to the E_2 state can be also stimulated to decay to the E_1 state by interacting with a photon with energy $h\nu$. This process will result in emission of two photons with the same energy, phase, and direction. This is the basis of stimulated emission. Light sources such as sun light only emit photons without phase matching, which is called the spontaneous emission. Laser is the light source with unidirectional, monochromatic emission properties, and thus it can have high energy. Laser is the consequence of stimulated emission, as named from light amplification by stimulated emission of radiation.

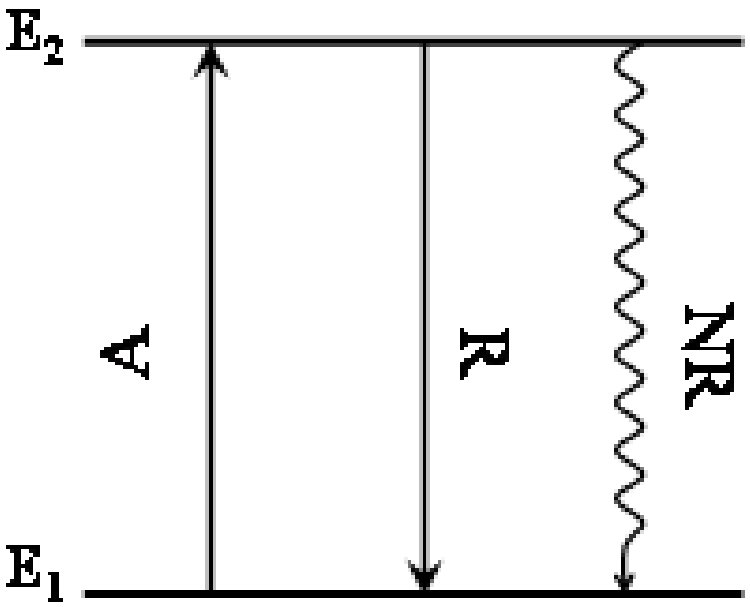

Fig. 1.1: Light absorption and emission processes. E_1 and E_2 represent the ground state and excited state, respectively. A, R, and NR denote light absorption, radiative (emission), and nonradiative processes

1.2 Multiphoton-excited fluorescence

As mentioned above, the photon energy of fluorescence is usually less than that of excitation light due to energy loss via lattice vibration. However, in some specific cases, it is feasible to obtain light emission with larger photon energy by excitation with smaller photon energy. This process is called upconversion fluorescence. For the upconversion fluorescence to occur, multiple photons must be involved in the excitation process; thus the upconversion fluorescence is also called multiphoton−excited fluorescence. Fig. 1.2 shows a simple upconversion process, in which E_1 is the ground state, E_2 and E_3 the excited states, respectively. If the energy separation between E_1 and E_2 is close to that between E_2 and E_3, the electron that absorbs a photon and transits to E_2 can absorb another excitation photon to be excited into E_3. In such a situation, emission of a photon with energy larger than the energy of an excitation photon is feasible when the electron in E_3 radiatively relaxes to E_1. Here, two photons successively excite the electron to E_2 and then E_3; hence, this process is two-photon excited fluorescence. In practical, three and four photon excitations are possible to give rise to upconversion fluorescence. There are many practical upconversion processes. Here the author just iterates those summarized by Blasse as schematically shown in Fig. 1.3.[1]

1. Upconversion by energy transfer sometimes called the APTE effect (Addition de Photons par Transfer d'Energie). Here A ions transfer successively their excitation energy to B ions which can then relax from a higher level to emit a photon.

2. Upconversion by two-step absorption, which needs only one ion which can absorb and emit photons.

3. Upconversion by cooperative sensitization: two A ions transfer simultaneously their excitation energy to one B ion which has no energy level at the position of the excited level of A. Emission occurs from the excited level of B.

4. Cooperative luminescence: two A ions combine their excitation energy to convert into

one quantum which is emitted (note, however, that there are no real emitting levels).

5. Second-harmonic generation (frequency doubling) in which the frequency of the irradiated light is doubled (without any transition by absorption taking place).

6. Two-photon absorption in which two photons are simultaneously absorbed without using any real intermediate energy level at all. One photon is emitted from the excited energy level.

Therefore, to tell the exact upconversion process is not easy. Nevertheless, the following characteristics can be summarized. In case of processes 1 and 3, a second ion is present to provide energy transfer, while it is not for the other processes. There are no real emitting levels for processes 4, 5, and 6. These points are useful to distinguish the above processes. Actually, the process is rather complicated. For instance, a three−photon absorption excitation process can be divided into several cases. This will be discussed below.

The number of photons for excitation involved in the upconversion process abides by a simple formula,[2] $I \propto P^n$, where I is the integrated emission intensity of upconversion fluorescence, P is the excitation power and n the number of photons for excitation. If n=2, one can say that the upconversion process results from a two-photon excited fluorescence. Therefore, in order to determine the value of n, a log-log plot between I and P is usually required.

Materials doped with REs such as Er^{3+}, Tm^{3+}, and Pr^{3+} are upconversion media widely studied,[3] for which commercial semiconductor lasers in near-infrared wavelength regions such as 800 and 980 nm are usually used as pumping sources to obtain upconversion fluorescence. In contrast, semiconductor lasers are not sufficient to realize upconversion fluorescence in case of TMs-doped materials, for which ultrafast and ultrashort lasers such as femtosecond lasers are usually used as pumping sources.[4-6] Upconversion fluorescence can find applications in areas of optical storage, optical marks of invisible light sources like infrared beam, and short-wavelength lasers.

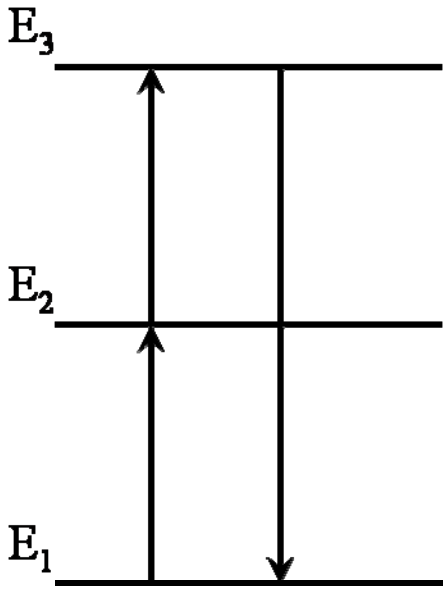

Fig. 1.2: Principle of a simplified upconversion process.

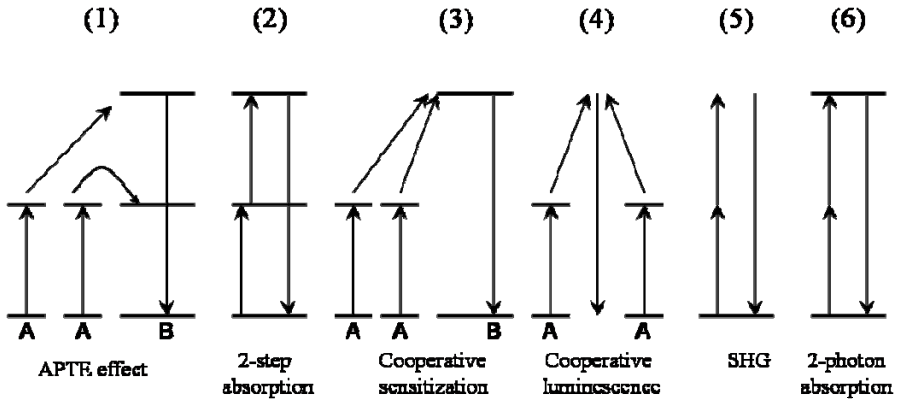

Fig. 1.3: Several upconversion processes according to Auzel[1].

1.3 Defects in silica glass

In this section, the author makes a brief introduction of defects in silica glasses to facilitate the understanding of fluorescence mechanism of d^0 ion-doped silicate glasses that will be presented later. These defects have important influence on optical and electronic properties of glasses. The formation of various defects is closely related to the chemical bond in random glass networks. In case of oxide glasses, the glass formers can be SiO_2, GeO_2, B_2O_3, Al_2O_3, and P_2O_5, for which dominant glass networks are totally different from each other.[7] This thesis will mainly treat the case of SiO_2. Pure silica glasses comprise random network of SiO_4 tetrahedra, in which every O^{2-} ion is bound to two Si^{4+} ions. The O^{2-} ion acts as a bridge between two neighboring Si^{4+} ions, hence O^{2-} ion is also called the bridging oxygen. The influence of addition of alkaline oxides such as Na_2O on the glass network structure can be simply given by

$$\equiv Si-O-Si\equiv + Na_2O \rightarrow \equiv Si-O-Na + Na-O-Si\equiv$$

A portion of O^{2-} ions no longer provides the bridges to the neighboring Si^{4+} ions; hence, they are called non-bridging oxygens. Similarly, the influence of addition of alkaline-earth oxides on the glass networks can be described as

$$\equiv Si-O-Si\equiv + CaO \rightarrow \equiv Si-O-Ca-O-Si\equiv$$

In both cases of alkaline and alkaline-earth oxide addition, the SiO_4 tetrahedra are broken partially and a portion of O^{2-} ions are no longer bridging oxygens but non-bridging oxygens. The formation of non-bridging oxygen can be one of the origins of defects in silicate glasses.

Oxygen-associated defects in silica glasses significantly affect the optical properties such as optical absorption and fluorescence. The defects with unpaired electrons are called paramagnetic defects which can be detected via ESR measurements,

while those having no unpaired electrons are called diamagnetic defects incapable to detect by ESR. The optical absorption bands ascribed to defects is presented in Fig. 1.4. Some of the defects shown in this Fig. have been already confirmed by experiments, while the others are still tentatively proposed ones.[8-10] What are concerned in this work are the defects with absorption bands located within a range of 4~6 eV that are marked by 7 to 12 since the absorption bands of d^0 ion-doped glasses are in principle present in this regime. Among these defects, E′ (≡Si↑, ↑ means one unpaired electron)[11] and divalent Si (O-Si↑↑-O)[10] belong to oxygen vacancy-related defects; non-bridging oxygen hole center (NBOHC, ≡Si-O↑)[12] and peroxy radical (POR, ≡Si-O-O↑)[13] are excessive oxygen-related defects while ozone (O_3)[10] is an interstitial chemical species. Chlorine molecule (Cl_2)[10] should be ruled out since chlorine is not contained in raw materials and not used in the experimental procedures in this work.

Nevertheless, it is hard to distinguish these five defects from each other only based on their absorption spectra since their bands are overlapped with each other. Another useful way is to analyze fluorescence properties. For instance, NBOHC can give rise to an emission band at 1.9 eV by 6.4 or 2.0 eV excitation, while divalent Si can yield two emission bands at 4.4 and 2.7 eV by 5.0 eV excitation.[14-16] O_3 shows a photostimulated phosphorescence band at around 0.974 eV by excitation at 7.9 eV.[17] The fluorescence properties of E′ and POR defects have not been reported yet up to now.

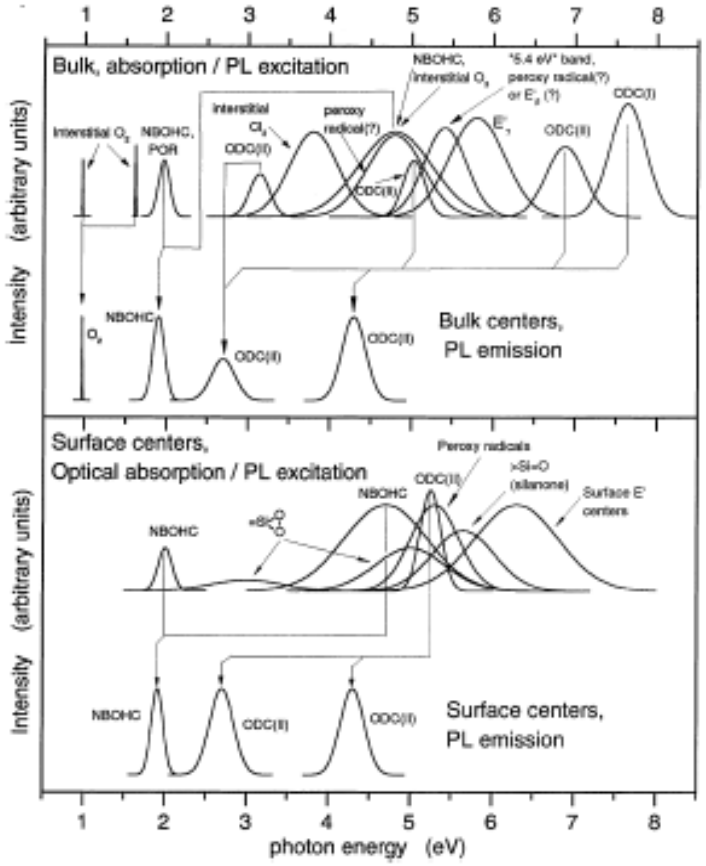

Fig. 1.4: Overview of major optical absorption, excitation, and emission bands of defect centers in synthetic silica (top) and of centers on the surfaces of SiO_2 (bottom). The relationship between the emission and excitation bands is indicated. The band intensities shown are arbitrary, and the positions and halfwidths correspond to their respective reported value.

1.4 Light scattering

In this section, light scattering behaviors of single scattering event are first described, and then extended to multiple scattering.

1.4.1 Single scattering

The treatment of light scattering by a single particle the size of which is much smaller than the wavelength of light is relatively easy although the actual physical process is rather complex. The incident light will induce a polarization in the particle, which will consequently result in an internal electric field in the particle. The resultant internal electric field has an influence on behaviors of the outgoing light. Therefore, the outgoing light results from the complex interaction between external and internal electric fields. For a particle much smaller than the wavelength of light, the scattering behavior can be described by the Rayleigh scattering theory. The parameter to characterize the particle size is usually defined as[18]

$$x = \frac{2\pi r}{\lambda} = kr \,, \tag{1.1}$$

where r is the radius of the particle, λ is the wavelength of light in the medium, and k is the wavevector in the medium $k=2\pi/\lambda$. The criterion often used for Rayleigh scattering is the condition that $n_{\text{particle}}x/n_{\text{surrounding}}<<1$, where n_{particle} and $n_{\text{surrounding}}$ are the refractive indices of the particle and surrounding matrix, respectively. The scattering strength of a single particle is characterized by the term of cross section. The concept of cross section is used in physics to quantify the probability of particle-particle interactions such as scattering, absorption and emission (In case of interaction between light and particle, photons can be viewed as quasi-particles). It stands for the virtual area around the particle, through which the flux of incident beam passing is equal to the flux that is concerned (e.g., absorption, scattering, emission). For instance, the flux of scattered

light can be given by

$$F_s(\omega) = \sigma_s F_{inc}(\omega)\,, \tag{1.2}$$

where $F_s(\omega)$ is the scattered flux, $F_{inc}(\omega)$ is the incident flux. Similarly, the absorption cross section is defined as the area through which the incident flux passing is absorbed. The extinction cross section (σ_e) of a particle is composed of the absorption (σ_a) and scattering cross section (σ_s), which is given by

$$\sigma_e = \sigma_a + \sigma_s\,. \tag{1.3}$$

The scattering coefficient Q_s is expressed as the scattering cross section divided by the geometrical area of the particle; i.e., $Q_s=\sigma_s/\pi r^2$. Usually, Rayleigh scattering shows angular dependence. The angular distribution of light intensity via Rayleigh scattering is given by[19]

$$I = I_0 \frac{1+\cos^2\theta}{2R^2}\left(\frac{2\pi}{\lambda}\right)^4\left(\frac{n^2-1}{n^2+2}\right)^2 r^6\,, \tag{1.4}$$

where I_0 is intensity of the incident light, R is the distance from the light to the particle, θ is the scattering angle, λ is the wavelength of incident light in vacuum, n is the relative refractive index of the particle to the surrounding medium, and r is the radius of particle. One can see that the scattering shows both wavelength dependence and particle size dependence. The term, $1+\cos^2\theta$ denotes the angular distribution of Rayleigh scattering, which is symmetric in a plane normal to the incident light so that the forward scattering equals to the backward scattering. Integrating Eq. (1.4) over the sphere surrounding the particle gives rise to the Rayleigh scattering cross section σ_s:

$$\sigma_s = \frac{2^7\pi^5}{3}\frac{r^6}{\lambda^4}\left(\frac{n^2-1}{n^2+2}\right)^2\,. \tag{1.5}$$

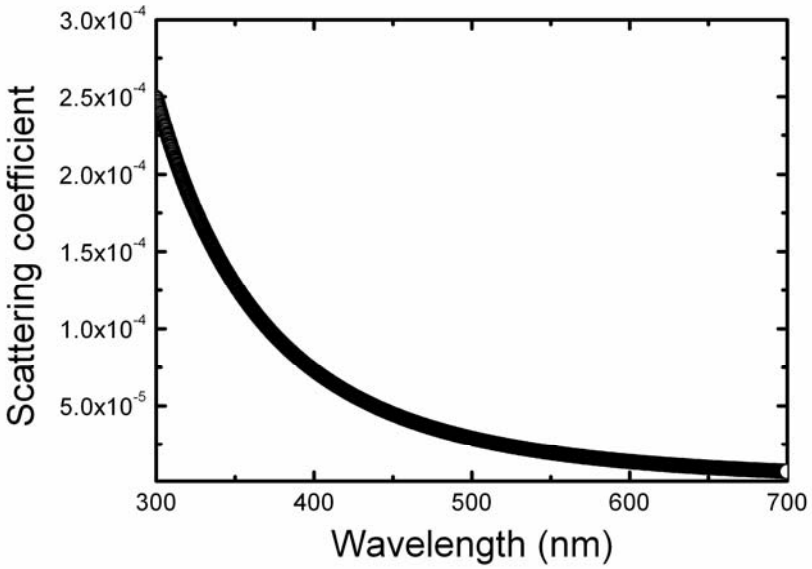

Fig. 1.5: Scattering coefficient of a 10 nm-radius SiO_2 particle as a function of wavelength. The refractive index of the particle is ~1.45. The particle size is much smaller than the wavelength of light so that its scattering behavior abides by Rayleigh scattering.

Therefore, the scattering cross section is a reciprocal of the fourth power of the wavelength. The scattering cross section from a particle at blue component of sunlight is larger by about five orders of magnitude than that for the same particle at red light, which accounts for the reason why the sky looks blue. However, the sky looks red at sunset since the color corresponds to the light of longer wavelength that is less efficiently scattered. Fig. 1.5 depicts the variation of the scattering strength with the wavelength of light for a SiO_2 particle with a radius of 10 nm in vacuum.

For a particle comparable to or larger than the wavelength of light, the Mie theory is used to analyze the scattering behaviors.[20,21] The Mie cross section, which is valid for spheres of any sizes, is obtained from calculation more complicated than the Rayleigh approximation. In the determination of the scattering cross section via the Mie theory, the incident wave is expanded as an infinite series of vector spherical harmonics. The tangent components of the total (incident plus scattered) electric and

magnetic fields at the surface of the sphere should be continuous across the boundary. The Mie total scattering cross section is given by:

$$\sigma_{Mie} = \left(\frac{2\pi}{k^2}\right)\sum_{n=1}^{\infty}(2n+1)(|a_n|^2 + |b_n|^2), \tag{1.6}$$

where k is the wavevector of light in the surrounding medium. The coefficient a_n and b_n are given by

$$a_n = \frac{\mu m^2 j_n(mx)[xj_n(x)]' - \mu_1 j_n(x)[mxj_n(mx)]'}{\mu m^2 j_n(mx)[xh_n^{(1)}(x)]' - \mu_1 h_n^{(1)}(x)[mxj_n(mx)]'} \tag{1.7}$$

$$b_n = \frac{\mu_1 j_n(mx)[xj_n(x)]' - \mu j_n(x)[mxj_n(mx)]'}{\mu_1 j_n(mx)[xh_n^{(1)}(x)]' - \mu h_n^{(1)}(x)[mxj_n(mx)]'}, \tag{1.8}$$

where j_n's are the spherical Bessel functions of the first kind, the h_n's are the spherical Hankel functions, μ_1 and μ are the magnetic permeabilities of the sphere and surrounding medium, respectively.

If the light is scattered by a collection of particles, the total scattering intensity is not simple summation of the scattering intensity of individual particles. Even if the light is scattered on average only once in case that assemblage of particles is optically thin, co-operative effects can occur. The total scattered intensity is determined by[1]

$$I(t,r) = \frac{c_0 n}{2}\left|E_1(t,r) + E_2(t,r) + E_3(t,r) + \cdots\right|^2, \tag{1.9}$$

where $E_n(t,r)$ denotes the individual scattering event that contributes to the total scattered light intensity, c_0 is the speed of light in vacuum, and n is the effective refractive index of the whole system. Mathematically, the square of summation of several terms is totally different from their summation of the square. If these terms are optically in phase, the former (in scale of N^2 times individual $E_n^2(t,r)$) will be much larger than the latter (in scale of N times individual $E_n^2(t,r)$). This is the result of

interference effect, which is observed in optical fields frequently. For instance, a water droplet is much more efficient in light scattering than the steam before agglomeration.

1.4.2 Multiple scattering

When the scattering system is optically thick, the light will undergo multiple scattering before escaping the system. Light propagation in such a medium is usually described by the model of light diffusion. The interference effect is usually negligible since individual scattering events are totally random without phase matching. However, the interference effect is significant in case that two light waves propagate along the same path but in opposite directions. Even only one event leading to such a situation is sufficient to change the scattering behavior. Especially in an amplified medium pumped at very large pump rate, a drastic increase of the number of emitted photons enhances the possibility to form such a light wave path. This process is also called recurrent scattering. It is a common scenario in the onset of coherent feedback of random lasers, which will be discussed later.

The scattering mean free path is used to characterize the scattering strength, which is defined as the average distance between two successive scattering events. In a scattering system containing particle the number density of which is ρ, the scattering mean free path l_s is expressed as[22]

$$l_s = \frac{1}{\rho \sigma_s}, \tag{1.10}$$

where l_s is the scattering mean free path, σ_s is the scattering cross section of the individual particle. The above formula stands for the relationship between the mean free path and the cross section, which can be extended to any cases concerning mean free path and corresponding cross section. For instance, the relationship between the absorption mean free path and the absorption cross section is written as $l_a=1/\rho\sigma_a$, in

which ρ is the number density of absorbing particles.

Another important mean free path is the transport mean free path l_t that is defined as the average distance that light travels before its direction changes. In media where an isotropic scattering takes place, the transport mean free path is equal to the scattering mean free path. However, in anisotropically scattering media, the two parameters are related to each other through an angular function that is given by[23]

$$l_t = \frac{1}{1-\langle \cos\theta \rangle} \frac{1}{\rho \sigma_s}, \tag{1.11}$$

where <cosθ> denotes the average of cosine of the scattering angle for each scattering event. It is obvious that Rayleigh scattering corresponds to <cosθ>=0 while Mie scattering may have <cosθ>≈0.5. The cross section corresponding to the transport mean free path is called the cross section for radiation pressure σ_t, which describes the average momentum transfer to the scattering centers.

There are two mean free paths as to light absorption; one is the absorption mean free path l_a, while the other is the inelastic mean free path l_i. The inelastic mean free path is defined as the traveled length over which the light intensity is reduced by a factor e^{-1} due to light absorption. The absorption mean free path is defined as the average distance between initial and final points fro paths of length l_i[23]

$$l_a = \frac{1}{3}\sqrt{3 l_t l_i}\ . \tag{1.12}$$

1.5 Random lasers

1.5.1 History, development and applications

Everything has two sides: the bright side and shadow side. It is true for light scattering as well. Light scattering has been always thought to be detrimental to lasers until Ambartsumyan et al. proposed a new type of laser in 1966, where non-resonant feedback occurred through reflection in strongly scattering medium used in place of

back laser mirror.[24] In the laser with non-resonant feedback, the central emission frequency was determined by the resonant frequency of the gain medium instead of eigenmodes of the resonator, the laser has low coherence, and its photon statistics and the dynamics of the line narrowing are different from those in conventional lasers. In 1967, Letokhov made a further theoretical prediction that laser-like peaks could be produced in an assemblage of strongly scattering particles possessing gain in the case the light moves in a diffusive way.[25] The scattering medium resembles the conventional active laser medium and recurrent scattering events in phase provide the feedback for laser oscillation. Letokhov predicted the laser threshold and the linewidth of laser-like peaks in such scattering systems by solving diffusion equations and rate equation.

As random amplifying media, REs-doped laser crystalline powders (the size of the crystalline powder is in a scale of several microns) were focused in the early stage.[26-30] In the late 1980's to the early 1990's, the research on random lasers exclusively concentrated on powders of laser crystals containing Nd^{3+}. It was found that the duration of the laser output pulse was remarkably shortened by four orders of magnitude when the pump energy reached a threshold. The linewidth of $^4F_{3/2} \rightarrow {}^4I_{11/2}$ transition (~1064 nm) was significantly reduced. When the pump energy was high enough, only one single laser line was observed.

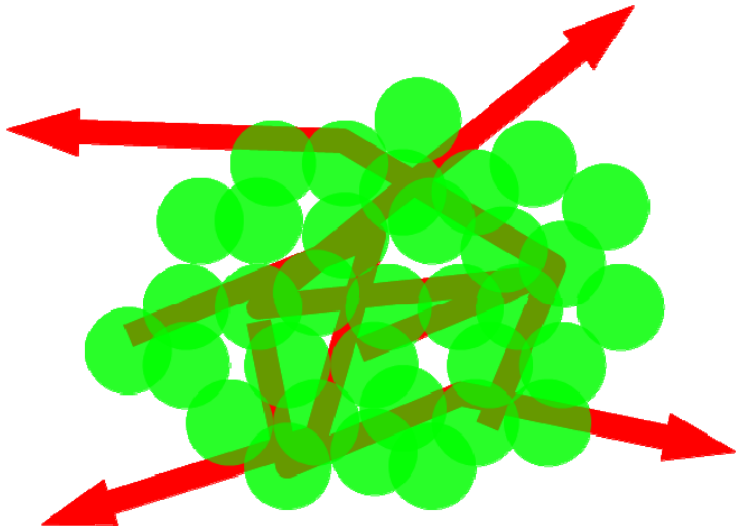

Fig. 1.6: An example of multiple light scattering with gain in microspheres stacked randomly. The spheres scatter and amplify light during light transport.

Since the early stage of 1990's, random laser materials containing other REs have been developed such as Pr^{3+}-and Ti^{3+}-based crystals.[31,32] Another approach to construct random laser materials is to disperse particles into a solution which contains laser active centers, as demonstrated by Lawandy in 1994.[33] The advantage of such a medium is that the degree of scattering can be easily controlled by the concentration of particles. The work by Lawandy stimulated further research interests on random lasers. The term of random lasers was firstly introduced by Lagendijk and Wiersma in 1995 when discussing the work of Lawandy.[34] An attractive observation was reported in 1999 by Cao et al. on coherent feedback random lasing from ZnO powders.[35] Initially, the emission in ZnO powders exhibits a broad spontaneous emission band at low pump energy. An increase in the pump energy makes the emission band narrower so that ASE becomes dominant at the threshold pump energy. Sharp peaks with linewidth much less than 1 nm appear when the pump energy reaches the second threshold. A further increase in the pump energy induces more sharp peaks superimposed on the ASE background. The calculated critical pumping area is consistent with the experimental result. The laser emission takes place along all directions. Since ZnO is an attractive

semiconductor material with high gain and the observed lasers showed coherent feedback, this work stimulated further studies on random lasers of ZnO-based materials. It is thought that recurrent light scattering gives rise to closed loop paths also called ring cavities in which coherent feedback is achieved so that sharp laser peaks appear. The presence of closed loop paths is understandable in case of strong scattering media but rather difficult to consider in weak scattering media. ZnO powders belong to strong scattering media.

A major advantage of random laser materials is that the fabrication process is relatively simple and does not cost. Random media can be prepared in a large-scale production. The technique with high precision involved in the fabrication of conventional lasers is not required here. The unique property of random lasers is that the emission has a large angular dependence and high intensity, which are especially useful for displays. At this moment, most of the random lasers are pumped by optical sources such as pulsed lasers. One problem is that electrically pumped random laser materials should be developed for practical applications in displays. In fact, such materials have been realized; for instance, Yu's group has developed p-SiC(4H)/i-ZnO-SiO_2 nanocomposite/n-ZnO:Al heterojunction diodes and realized random lasers with high intensity.[36] Gottardo has demonstrated electrical tuning of the direction of laser beam from a polymer-dispersed liquid crystal that is commonly used for displays.[37] These results clearly indicate random lasers can find potentials applications in displays.

Another advantage of random lasers is that they can be prepared in form of suspensions of particles which can be used as coatings on surfaces of any shape. It is especially effective for environment lighting, e.g. in the form of street lighting that is applied on the road. The same technology has yielded a patent for use as identification of vehicles of friend/enemy. In addition, it has been shown that random lasers are sensitive to temperature, e.g. the central frequency of the laser is tunable by changing temperature, as demonstrated by Wiersma.[38] This behavior can be used for remote

temperature sensing. In addition to the random lasers from laser crystal powders, semiconductor powders and suspension of particles in dye solution, random lasers have been also observed in tissues infiltrated with dye, which implies the potential of random lasers in medical diagnosis.[39] Random materials can also act as microlaser sources. Cao et al. has demonstrated laser operation in one ZnO cluster.[40] The ZnO cluster comprises a large amount of small particles and serves as one single lasing resonator. The lasing mode can be controlled by the pump energy. The experimental results are consistent with numerical simulation. In conclusion, there are interesting phenomena from a point of view of many potential applications as well as physics and chemistry involved in random lasers, making random lasers rather attractive topics nowadays. For clear demonstration of effectiveness of random lasers, various potential applications and relevant fundamental phenomena are summarized in Fig. 1.7.

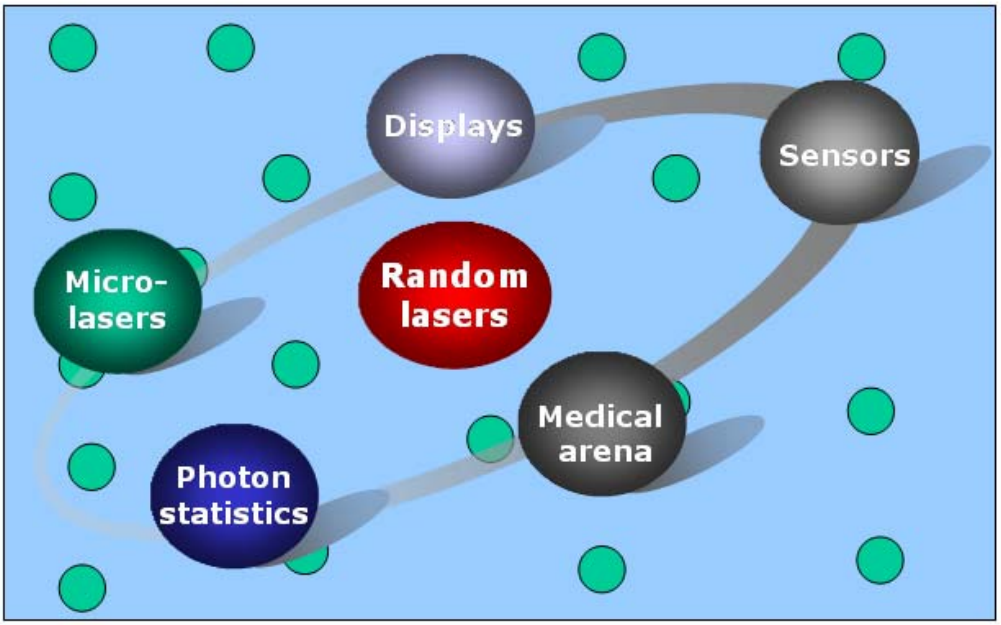

Fig. 1.7: Fundamental phenomena and applications of random lasers.

1.5.2 Light transport in amplifying random media

In general, light transport in media is described by Maxwell equation as follows

$$\nabla \cdot E = 4\pi\rho \tag{1.13}$$

$$\nabla \times E = -\frac{1}{c}\frac{\partial B}{\partial t} \tag{1.14}$$

$$\nabla \cdot B = 0 \tag{1.15}$$

$$\nabla \times B = \frac{4\pi}{c}J + \frac{1}{c}\frac{\partial E}{\partial t}, \tag{1.16}$$

where E is the electric field, B is the magnetic field, ρ is the charge density, and J is the current density. Solving Maxwell equation can lead to a distribution of the electric and magnetic fields, but the solving process is very complicated. The light transport in random media resembles the electron transport in semiconductors in many aspects such as Hall effect,[41,42] optical magnetoresistance,[43] Anderson localization[44-46], and universal conductance fluctuations[47]. A much similar point between light and electron transports lies in the Ohm's law of conductance.[48] For an electron, the resistance increases linearly with its length, resulting in the diffusive motion of electrons. The same transport law holds for the light waves in an opaque random dielectric medium without optical absorption, in which the intensity of transmitted light via diffusion process decreases linearly with the sample thickness. The conductance is associated with the absorbance through the following formula:

$$A = \frac{\sigma d}{\varepsilon_0 cn}, \tag{1.17}$$

where A is the absorbance, σ is the conductance, d is the sample thickness, ε_0 is the dielectric constant in vacuum, c is the speed of light in vacuum and n is the refractive index. In amplifying random media, the gain is involved so that the absorbance A is

usually described as negative absorption and the conductance is also negative. Light waves in random media perform a random walk with a characteristic mean free path l. If the mean free path is much larger than the sample size L, light mainly propagates so that the intensity of light varies linearly with the thickness of the sample before going out. Otherwise, light transport will experience multiple scattering events, which is described by light diffusion approximation. The model of light diffusion plays an important role in the multiple scattering theories. In the diffusion approximation, the intensity $I(r,t)$ is determined by a diffusion equation:

$$\frac{\partial I(r,t)}{\partial t} = D\nabla^2 I(r,t) - \frac{v}{l_i} I(r,t), \tag{1.18}$$

where D is the diffusion coefficient, v is the transport velocity of light in the medium, and l_i is the inelastic mean free path. The diffusion coefficient is given by $D=lv/3$.

1.5.3 Strong scattering and weak scattering

The scattering strength is characterized by the product of the wavevector of light k and the transport mean free path l_t. If $kl_t>>1$, the random medium is described as a weak scattering medium. If $kl_t \rightarrow 1$, it becomes a strong scattering medium. When $kl_t \leq 1$, the light transport tends to halt; this phenomenon is designated as the Anderson localization for light. The above-mentioned ZnO powders are a typical example of strong scattering media. The scattering cross section is proportional to the difference in refractive index between a scattering center and a surrounding material, and hence high refractive materials such as ZnO,[49] TiO_2,[50] and GaP,[51] are generally used to obtain intense scattering strength. Weak scattering systems usually refer to the solution of dye suspended with dielectric nanoparticles such as SiO_2, TiO_2 and ZnO. Here, the number density of particles and the concentration of dye can be separately tuned. The solution can be replaced by polymer films in which dielectric particles are dispersed.

Strong scattering facilitates recurrent scattering events so that the coherent

feedback is readily achieved. However, the scattering strength has to be optimized because excessive light scattering significantly reduces the pumping efficiency, especially for optical pumping.[52] In order to overcome this problem, some researchers have tried to make use of multiphoton pumping schemes since the light with longer wavelength can penetrate into a deeper depth in scattering media compared with the visible light.[53,54] Weak scattering system is another solution that has been already conducted. Random lasers with coherent feedback were firstly observed in strong scattering systems, while recently sharp laser peaks have also been observed in weak scattering systems.

The origin for the coherent feedback in random lasers is still controversial. It is understandable that the emergence of sharp peaks in strong scattering media is usually ascribed to the formation of closed loop paths due to recurrent scattering events, which is also called Anderson localization of photons. However, according to the measurements of the scattering mean free path, many practical systems showing coherent laser emission are far from the condition for Anderson localization. Several mechanisms have been tentatively proposed to explain the coherent feedback in terms of almost localized modes,[55] the absorption induced localization in the local pump region,[56] and the amplification of spontaneous emission along very long paths (extended modes).[57]

1.5.4 How to tell the coherent nature?

When the pump energy exceeds a threshold, very sharp peaks appear in amplifying random media. The linewidth of these peaks is much narrower than 1 nm, and hence they are most likely real lasers. Conventional lasers are known for their unidirectional, monochromatic and coherent laser output. Nevertheless, random lasers emit light beams in all directions accompanied by random peaks. A plot of the integrated emission intensity against the pump energy shows a drastic increase in the slope at the

threshold pump energy, which may imply the occurrence of laser actions. However, the most convincing evidence to tell the coherent nature is to use photon statistics.[58] The incoherent light is describable in terms of the Bose-Einstein distribution function, while the coherent light can be interpreted by the Poisson distribution function. These distribution functions are given by

$$p(n,m) = \frac{m^n}{(1+m)^{1-n}} \tag{1.19}$$

and

$$p(n,m) = \frac{m^n e^{-m}}{n!}, \tag{1.20}$$

where $p(n,m)$ is the probability of observing n photons with a mean number of m. Eqs. (1.19) and (1.20) denote Bose-Einstein and Poisson distributions, respectively. A pioneering work was conducted by Cao et al. in 2001,[59] who observed that the distribution for the number of photon in a single mode changes continuously at the threshold from Bose-Einstein distribution to Poisson distribution. Fig. 1.8 shows the spectral/temporal variation of laser emission from ZnO powders. The horizontal axis is time and the vertical axis is wavelength. The emission intensity varies depending on the mode. A tiny rectangle is selected from one mode (usually the brightest mode), for which one side is $\Delta\lambda$ and another Δt. Then the number of photon per pulse is counted to be n and a large number of the data are collected, and the probability $p(n)$ of n photon within (λ, $\lambda+\Delta\lambda$) and (t, $t+\Delta t$) can be determined. It should be noted that the Δt must be as narrow as possible since incoherent distribution for a long observation time can also yield the Poisson distribution. Experimentally, Δt should satisfy $\Delta v \Delta t<1$, in which Δv is derived from $\Delta v=\Delta\lambda c/\lambda^2$. Under the above conditions, the collected mode is a single electromagnetic mode. Fig. 1.9 presents the photon count data obtained from the emission of ZnO powder. It shows that the photon statistics is the Bose-Einstein function at low pump energy and then changes to the Poisson function at high pump

energy. The photon statistics makes sense since it confirms the coherence nature of sharp peaks and provides guidance to successive experimental works.

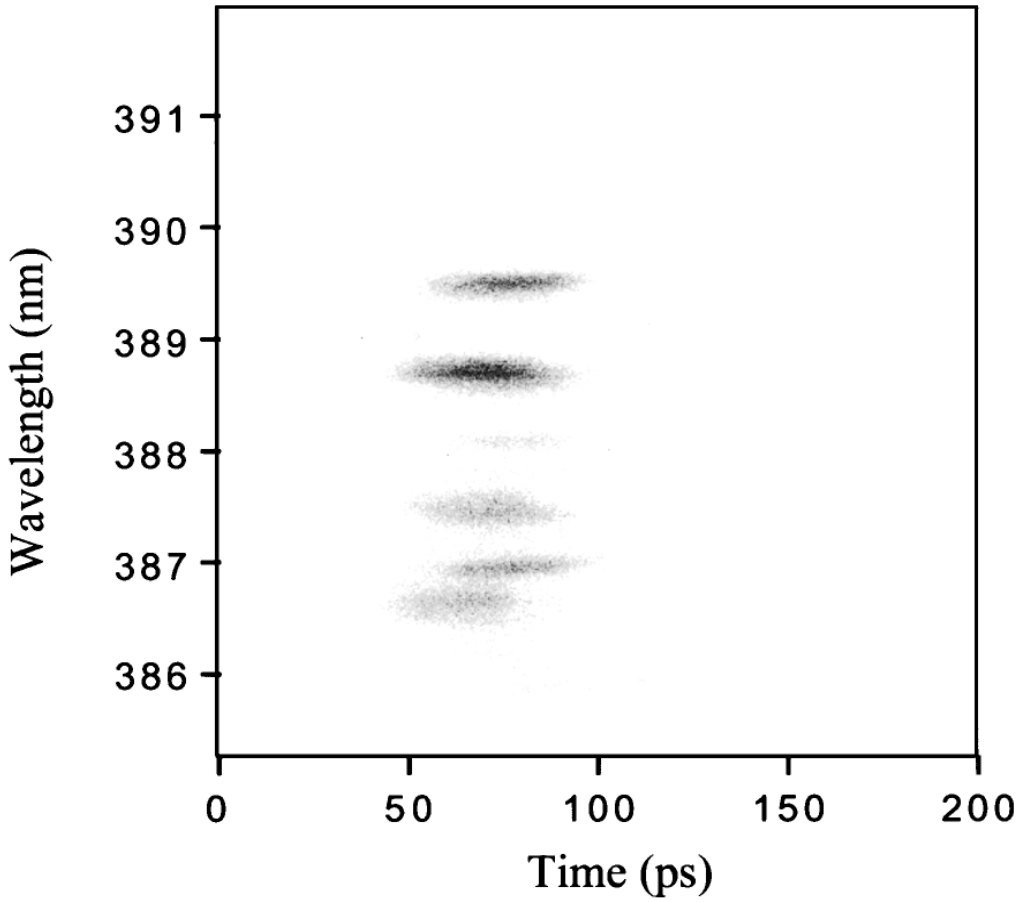

Fig. 1.8: The measured spectral/temporal variation of the emission in a pellet made of ZnO powders. The incident pump pulse energy is 4.5 nJ.

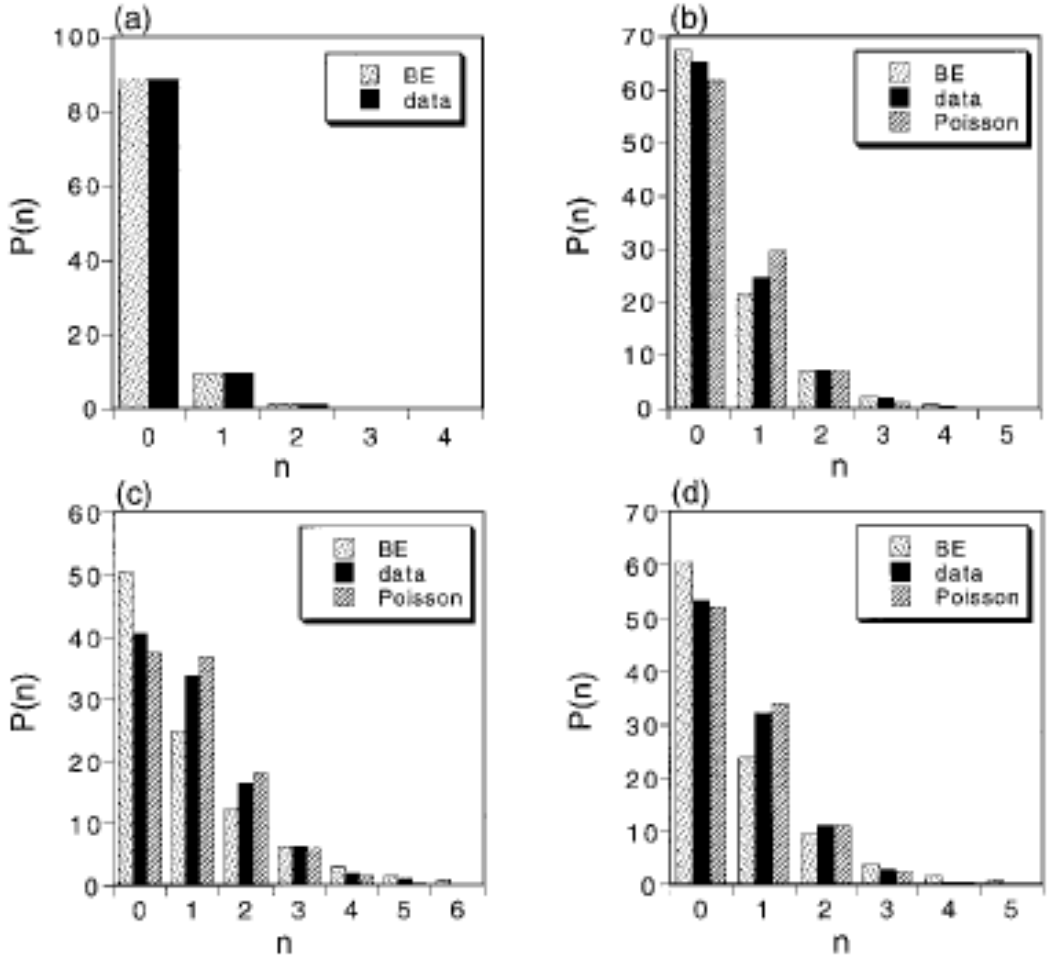

Fig. 1.9: The solid columns are the measured photon count distribution for the emission in a pellet made of ZnO powders. The dotted (dashed) columns are the Bose-Einstein (Poisson) distribution for the same mean count. The incident pump intensity is (a) 1.0, (b) 1.5, (c) 3.0, and (d) 5.6 times of the intensity at the threshold where discrete spectral peaks appear.

1.6 Surface plasmon resonance

Surface plasmons, also called electromagnetic surface modes, are electromagnetic excitations associated with charge density wave on the surface of nanoscale metallic systems. Surface plasmons have numerous effects in physicochemical fields such as surface-enhanced Raman scattering, enhanced transmission through subwavelength

apertures, and enhanced spontaneous emission efficiency for semiconductors, REs, and organic molecules.[60-63] Various promising applications such as biosensing, subwavelength imaging, waveguides, and switching devices below the diffraction limit, have been processed nowadays.[64-67] The excitation of surface plasmons by light is observed as surface plasmon resonance (SPR) for planar surfaces or localized SPR for nanometer-sized metallic structures. This phenomenon is the basis of many standard tools for measuring adsorption of chemical species onto planar metal (typically gold and silver) surfaces and onto surfaces of metal nanoparticles. It is also utilized for biosensor applications and different lab-on-a-chip sensors.

Fig. 1.10 depicts the evolution of SPR at the surface of metal nanoparticles. By the irradiation with light, free electrons that initially manifest a random distribution at the particle surface will response to the incident electric field and move collectively. The moment of electrons results in an internal electric field in opposite direction of the incident field. Simultaneously, the moment of electrons leads to charge density wave that propagates along the interface between metal nanoparticles and a surrounding medium. When the frequency of incident light is equal to the inherent frequency of internal electric field, the incident light will be strongly absorbed and scattered.

The permittivity of metals consists of real and imaginary part, i.e., $\tilde{\varepsilon}_m = \varepsilon_r + i\varepsilon_i$. The refractive index can be deduced from $n = \sqrt{\varepsilon}$, which is suitable for either dielectric or metallic materials. Therefore, the refractive index of metals is also a complex parameter $\tilde{n} = n + i\kappa$, in which n is the so-called refractive index and κ the extinction coefficient. The relationship between $\tilde{\varepsilon}_m$ and $\tilde{n}$ can be expressed as

$$\varepsilon_r = n^2 - \kappa^2 \tag{1.21}$$

$$\varepsilon_i = 2n\kappa . \tag{1.22}$$

The value of κ is usually zero in the visible wavelength region for dielectric materials

such as SiO_2, ZnO and TiO_2; hence, these media are non-absorbing materials. Nevertheless, as shown in Fig. 1.11 which illustrates n and κ as a function of wavelength, one can see that n is quite small (<<1) in the visible wavelength region, while κ is rather large for metals. Based on the Mie theory,[68] the extinction coefficient of media in which metal nanoparticles are dispersed can be expressed as

$$\alpha(\omega) = \frac{9q\varepsilon^{3/2}\omega}{c} \frac{\varepsilon_{\mathrm{i}}(\omega)}{[\varepsilon_{\mathrm{r}}(\omega) + 2\varepsilon]^2 + \varepsilon_{\mathrm{i}}(\omega)^2}, \tag{1.23}$$

where ε and q are the permittivity of host material and the volume fraction of metallic particles, respectively, and ε_{r} and ε_{i} are the real and imaginary parts of permittivity of metal nanoparticles, respectively. For a sphere much smaller than the wavelength, the scattering cross section is given by

$$\sigma_s \propto |\varepsilon - 1| / |\varepsilon + 2|, \tag{1.24}$$

where ε is the relative permittivity of the small spheres. Fig. 1.12 depicts the scattering cross sections of small dielectric and metallic spheres for comparison. Obviously, the scattering cross section of the metal nanoparticles is much larger than those of the dielectric particles in the visible and near-infrared wavelength regions. Especially, silver nanoparticles are efficiently scattering centers. Therefore, the silver nanoparticles are used for the experiments on random lasers in this thesis.

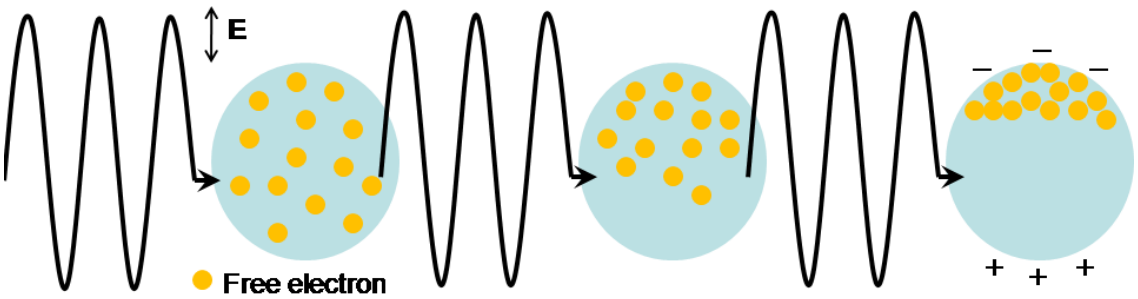

Fig. 1.10: A schematic illustration of the formation of surface plasmon resonance.

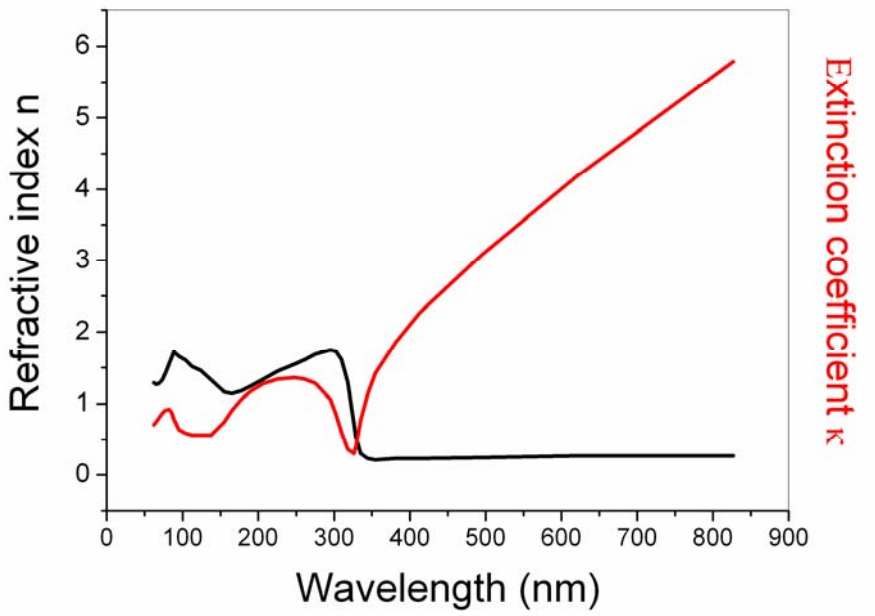

Fig. 1.11: Wavelength dependence of real and imaginary parts of the refractive index for bulk silver.

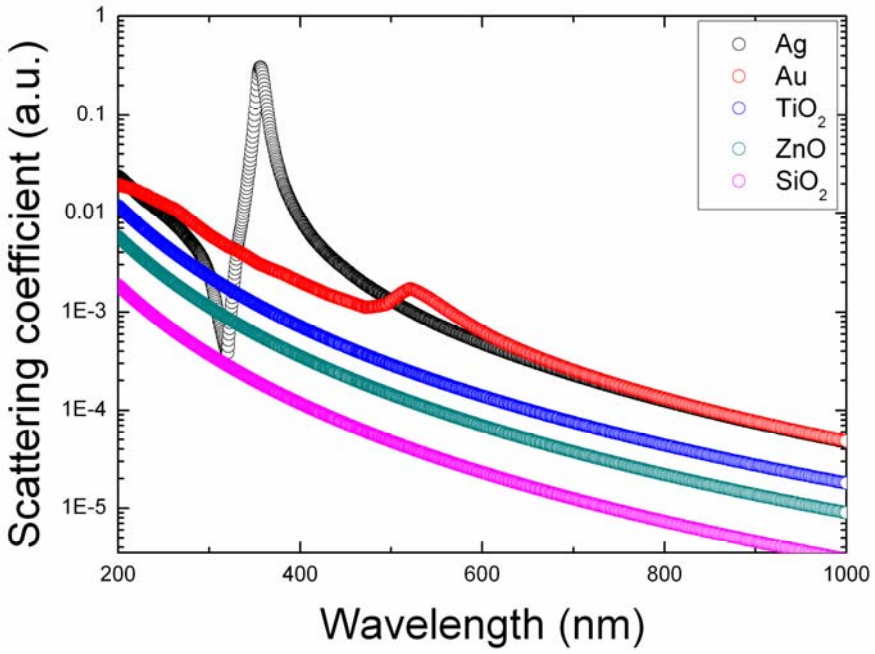

Fig. 1.12: A comparison of scattering cross sections of Ag, Au, TiO_2, ZnO and SiO_2 spherical nanoparticles with a radius of 10 nm.

One of the typical configurations to produce surface plasmon wave is called

Kretschmann configuration[69] that comprises metal thin film attached to a dielectric prism, as shown in Fig. 1.13 (a). When the incident light is totally reflected at the interface between the metal thin film and the dielectric prism, an evanescent wave is caused to penetrate through the metal film and induces a surface plasmon wave on the other side of the film. The wave number vector of the surface plasmon mode is a function of the dielectric functions of metal (ε_m) and dielectric prism (ε_d), as expressed by

$$k_{sp} = \frac{\omega}{c}\sqrt{\frac{\varepsilon_m \varepsilon_d}{\varepsilon_m + \varepsilon_d}}\,. \tag{1.25}$$

As mentioned above, the real part of ε_m is negative and its absolute value is rather large, and hence, k_{sp} is also composed of real and imaginary parts. Its imaginary part characterizes the propagation length of surface plasmon wave before it is damped into the metal. The propagation length in the visible wavelength is about tens of micrometers at the smooth surface of noble metals such as silver and gold. Fig. 1.13 (b) shows the dispersion relation for both surface plasmon wave and incident light, which are denoted by the dotted blue line and solid red line, respectively. The red line is always below the blue line. Therefore, an additional component is required to make the incident light coupled to the surface plasmon mode and maintain the momentum preservation

$$k_{sp} = k_{inc} + G\,. \tag{1.26}$$

This is the simplest resonance condition, which is the function of incident angle θ. The above relation should be modified as

$$k_{sp} = k_0 \sin\theta + G\,. \tag{1.27}$$

A method to supply G is to use a periodic array. G can be expressed as multiples of $2\pi/a_0$, where a_0 is the period of the structure. When the following equation is satisfied

(*n* is an integer):

$$k_{sp} = k_0 \sin\theta + n \times \frac{2\pi}{a_0}, \tag{1.28}$$

the incident light can be coupled to the surface plasmon mode. Under the resonant conditions, the light wave will be spatially confined at the surface of the metal, accompanied by the formation of highly localized optical modes. At every wave number equal to multiple of π/a_0 (Brillouin zone edge), the surface plasmon wave is strongly reflected so that it can not propagate any more. Therefore, bandgaps appear in the dispersion relation of surface plasmon, corresponding to stationary waves and high field enhancements.

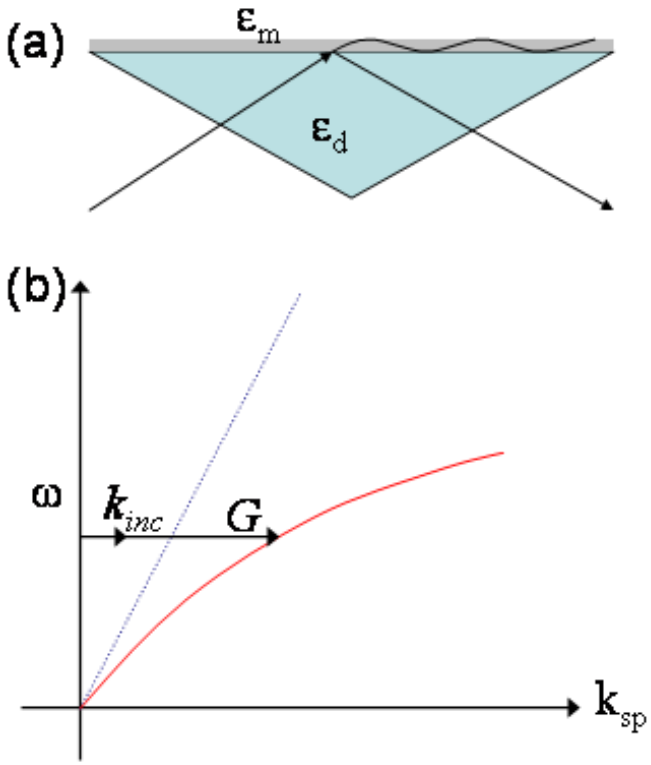

Fig. 1.13: (a) Kretschmann configuration and (b) dispersion relation of the surface plasmon mode. Here, ε_m and ε_d represent the permittivity of metal and dielectric prisms, respectively, which can be extended to any systems that can generate surface plasmon mode. In (b), k_{sp} and k_{inc} represent the transverse wave vectors of surface plasmon wave and incident light, respectively. The dotted blue line is the dispersion relation of the incident light while the solid red line is that of surface plasmon wave. G is the wave vector that is needed to couple the incident wave vector with the surface plasmon wave vector.

1.7 Rate equation of laser

For a collection of particles that obey Maxwell-Boltzmann statistics, most of the particles occupy the ground state instead of high energy states at thermal equilibrium. In order to realize light amplification and then laser output, external energy such as light

and electric field must excite electrons so that the electrons occupy the higher energy levels. Whether the laser output can be realized or not depends on the competition between the spontaneous and stimulated emissions. The gain coefficient of the medium can be given by

$$\gamma(\nu) = (N_2 - \frac{g_2}{g_1} N_1) \frac{c^2 A_{21}}{8\pi\nu^2} g(\nu_0, \nu), \tag{1.29}$$

where $\gamma(\nu)$ is the gain coefficient of the medium, N_1 and N_2 are the number density (per volume) of particles in the lower and upper energy levels, g_1 and g_2 are the degeneracy of the lower and upper energy levels, A_{21} is the spontaneous emission rate from the upper energy level to the lower energy level, c is the speed of light in vacuum, ν is the frequency of light, ν_0 is the central frequency of the spontaneous emission, $g(\nu_0, \nu)$ is the lineshape function of the spontaneous emission. In order to realize the light amplification, Eq. (1.29) should satisfy that

$$N_2 - \frac{g_2}{g_1} N_1 > 0. \tag{1.30}$$

Hence, the number density in the upper energy level must be larger than that in the lower energy level. This is called the population inversion, which is necessary for the output of laser irradiation.

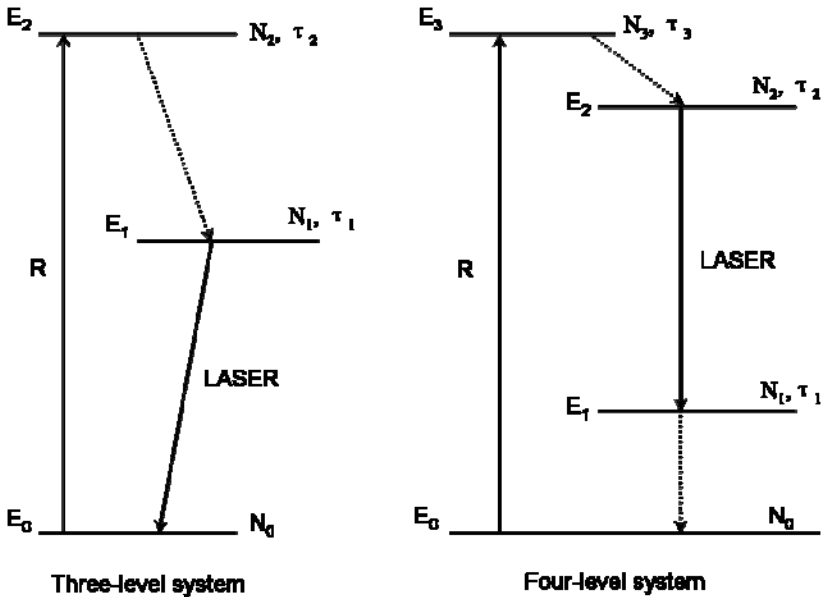

Fig. 1.14: Schematic representations of three-level and four-level laser systems.

The principle and mechanism of practical lasers include two types: three-level and four-level systems, as shown in Fig. 1.14, where E_0, E_1, E_2, E_3 indicate the energy levels, N_0, N_1, N_2, N_3 are the particle density in E_0, E_1, E_2, and E_3 states, R is the pumping rate, τ_1, τ_2 and τ_3 are the lifetime in E_1, E_2 and E_3, respectively. In some literatures, the three-level systems are included into the four-level systems when $E_1 << kT$ is satisfied. The most commonly used lasers belong to the four-level system, although the first laser operation was performed in a three-level system $Al_2O_3:Cr^{3+}$. The threshold of three-level systems is much higher than that of four-level system, which can be seen from the following equation

$$\frac{N_2(3-level)}{N_2(4-level)} = \frac{(g_2/g_1)N + N_t}{\left[(g_2/g_1)+1\right]N_t}, \tag{1.31}$$

where N is the total number of the particles per volume, N_2 is the threshold population inversion, and N_t is given by

$$N_t = \frac{8\pi}{A_{21}\lambda^2 g(\nu)c\tau_0}. \tag{1.32}$$

References

1. G. Blasse, B. C. Grabmaier, *Luminescent materials*, Springer-Verlag Berlin Heidelberg, 1994.
2. R. P. Chin, Y. R. Shen, and V. Petrova-koch, *Science* **270**, 776 (1995).
3. F. Auzel, *Chem. Rev*. **104**, 139 (2004).
4. H. You and M. Nogami, *Appl. Phys. Lett*. **84**, 2076 (2004).
5. X. Meng, K. Tanaka, S. Murai, K. Fujita, K. Miura, and K. Hirao, *Opt. Lett*. **31**, 2867 (2006).
6. L. Yang, C. Wang, Y. Dong, N. Da, X. Hu, D. Chen, and J. Qiu, *Opt. Exp*. **13**, 10157 (2005).
7. H. Scholze, *Glass nature, structure, and properties*, Springer-Verlag, New York, Berlin Heidelberg, 1991.
8. L. Skuja, M. Hirano, H. Hosono, and K. Kajihara, *Phys. Stat. Sol. (c)*, **2**, 15 (2005).
9. K. Kajihara, US-JAPAN 2008 Winter School, Kyoto, Japan.
10. K. Kajihara, *J. Ceram. Soc. Jap.* **115**, 85 (2007).
11. J. R. Chavez, S. P. Karna, K. Vanheusden, C. P. Brothers, R. D. Pugh, B. K. Singaraju, W. L. Warren, and R. A. B. Devine, *IEEE Trans. Nucl. Sci*. **44**, 1799 (1997).
12. M. Stapelbroek, D. L. Griscom, E. J. Friebele, and G. H. Sigel, Jr., *J. Non-Cryst. Solids* **32**, 313 (1979).
13. D. L. Griscom, *J. Ceram. Soc. Jpn.* **99**, 923 (1991).
14. L. Skuja, M. Hirano, H. Hosono, and K. Kajihara, *Phys. Stat. Sol. (c)* **2**, 15 (2005).
15. J. H. Stathis and M. A. Kastner, *Phys. Rev. B*, **35**, 2972 (1987).
16. L. Skuja, *J. Non-Cryst. Solids* **239**, 16 (1998).
17. H. Hosono, Y. Ikuta, T. Kinoshita, K. Kajihara, and M. Hirano, *Phys. Rev. Lett*. **87**, 175501 (2001).
18. D. S. Wiersma, Ph.D thesis, Amsterdam, Dutch (1995).

19. C. F. Bohren and D. Huffman, *Absorption and scattering of light by small particles*, John Wiley, New York, 1983.
20. A. J. Cox, A. J. DeWeerd, and J. Linden, *Am. J. Phys*. **70**, 620 (2002).
21. G. Mie, *Ann. Phys*. **25**, 377 (1908).
22. A. Ishimaru, *Wave propagation and scattering in random media*, Academic, New York, 1978.
23. H. Cao, *J. Phys. A: Math. Gen*. **38**, 10497 (2005).
24. R. V. Ambartsumian, N. G. Basov, P. G. Kryukov, and V. S. Letokhov, *IEEE J. Quantum Electron*. **QE-2**, 442, (1966).
25. V. S. Letokhov, *Zh. Eksp. Teor. Fiz*. **53**, 1442 (1967).
26. V. M. Markushev, V. F. Zolin, and Ch. M. Briskina, *Zh. Prikl. Spectroscopy*. **45**, 847 (1986).
27. C. Gouedard, D. Husson, C. Sauteret, F. Auzel, and A. Migus, *J. Opt. Soc. Am. B* **10**, 2362 (1993).
28. V. M. Markushev, V. F. Zolin, and C. M. Briskina, *Sov. J. Quantum Electron*. **16,** 281 (1986).
29. N. E. Ter-Gabrielyan, V. M. Markushev, V. R. Belan, Ch. M. Briskina, O. V. Dimitrova, V. F. Zolin, and A. V. Lavrov, *Sov. J. Quantum Electron*. **21**, 840 (1991).
30. F. Auzel and P. Goldner, *J. Alloys Compd*. **300-301**, 11 (2000).
31. V. F. Zolin, *J. Alloys Compd*. **300-301**, 214 (2000).
32. M. A. Noginov, N. E. Noginova, S. U. Egarievwe, H. J. Caulfield, C. Cochrane, J. C. Wang, M. R. Kokta, and J. Paitz, *Opt. Mater*. **10**, 297 (1998).
33. N. M. Lawandy, R. M. Balachandran, A. S. L. Gomes, and E. Saultravioletain, *Nature (London)* **368**, 436 (1994).
34. H. Cao, Y. G. Zhao, S. T. Ho, E. E. Seeling, Q. H. Wang, and R. P. H. Chang, *Phys. Rev. Lett*. **82**, 2278 (1999).
35. D. S. Wiersma, M. P. van Albada, and A. Lagendijk, *Nature (London)* **373**, 203 (1995).

36. E. S. P. Leong, M. K. Chong, S. F. Yu, and K. Pita, *IEEE Photonics Technology Letters* **16**, 2418 (2004).
37. S. Gottardo, S. Cavalieri, O. Yaroschuck, and D. S. Wiersma, *Phys. Rev. Lett*. **93**, 263901 (2004).
38. D. S. Wiersma and S. Cavalieri, *Nature (London)* **414**, 708 (2001).
39. R. C. Polson and Z. V. Vardeny, *Phys. Rev. B* **71**, 045205 (2005).
40. H. Cao, J. Y. Xu, S. H. Chang, S. T. Ho, E. W. Seeling, X. Liu, and R. P. H. Chang, *Phys. Rev. Lett*. **84**, 5584 (2000).
41. B. A. van Tiggelen, *Phys. Rev. Lett*. **75**, 422 (1995).
42. G. L. J. A. Rikken and B. A. van Tiggelen, *Nature (London)* **381**, 54 (1996).
43. A. Sparenberg, G. L. J. A. Rikken, and B. A. van Tiggelen, *Phys. Rev. Lett*. **79**, 757 (1997).
44. S. John, *Phys. Rev. Lett*. **53**, 2169 (1984).
45. P. W. Anderson, *Phil. Mag*. **52**, 505 (1985).
46. A. A. Chabanov and A. Z. Genack, *Phys. Rev. Lett*. **87**, 153901 (2001).
47. F. Scheffold and G. Maret, *Phys. Rev. Lett*. **81**, 5800 (1998).
48. D. S. Wiersma, R. Sapienza, S. Mujumdar, M. Colocci, M. Ghulinyan, and L. Pavesi, *J. Opt. A: Pure Appl. Opt*. **7**, S190 (2005).
49. S. F. Yu and E. S. P. Leong, *IEEE J. Quantum Electron*. **40**, 1186 (2004).
50. G. van Soest, F. J. Poelwijk, R. Sprik, and A. Lagendijk, *Phys. Rev. Lett*. **86**, 1522 (2001).
51. K. L. van der Molen, R. W. Tjerkstra, A. P. Mosk, and A. Lagendijk, *Phys. Rev. Lett*. **98**, 143901 (2007).
52. A. L. Burin, H. Cao, and M. A. Ratner, *IEEE J. Sel. Top. Quantum Electron*. **9**, 124 (2003).
53. C. F. Zhang, Z. W. Dong, G. J. You, and S. X. Qian, *Opt. Lett*. **31**, 3345 (2006).
54. E. V. Chelnokov, N. Bityurin, I. Ozerov, and W. Marine, *Appl. Phys. Lett*. **89**, 171119 (2006).

55. V. M. Apalkov, M. E. Raikh, and B. Shapiro, *Phys. Rev. Lett*. **89**, 016802 (2002).
56. A. Yamilov, X. Wu, H. Cao, and A. L. Burin, *Opt. Lett*. **30**, 2430 (2005).
57. S. Mujumdar, M. Ricci, R. Torre, and D. S. Wiersma, *Phys. Rev. Lett*. **93**, 053903 (2004).
58. M. I. Stockman, *Phys. Rev. Lett*. **79**, 4562 (1997).
59. H. Cao, Y. Ling, J. Y. Xu, C. Q. Cao, and P. Kumar, *Phys. Rev. Lett*. **86**, 4524 (2001).
60. C. Genet and T. W. Ebbesen, *Nature (London)* **445**, 39 (2007).
61. K. Okamoto, I. Niki, A. Shvartser, Y. Narukawa, T. Mukai, and S. Scherer, *Nat. Mater*. **3**, 601 (2004).
62. D. M. da Silva, L. R. P. Kassab, S. R. Luthi, C. B. De Araujo, A. S. L. Gomes, and M. J. V. Bell, *Appl. Phys. Lett*. **90**, 081913 (2007).
63. K. Aslan, M. Wu, J. R. Lakowicz, and C. D. Geddes, *J. Am. Chem. Soc*. **129**, 1524 (2007).
64. F. Frederix, J. M. Friedt, K. H. Choi, W. Laureyn, A. Campitelli, D. Mondelaers, G. Maes, and G. Borghs, *Anal. Chem*. **75**, 6894 (2003).
65. A. J. Haes and R. P. van Duyne, *J. Am. Chem. Soc*. **124**, 10596 (2002).
66. H. Ditlbacher, A. Hohenau, D. Wagner, U. Kreibig, M. Rogers, F. Hofer, F. R. Aussenegg, and J. R. Krenn, *Phys. Rev. Lett*. **95**, 257403 (2005).
67. M. L. Brongersma, J. W. Hartman, and H. A. Atwater, *Phys. Rev. B* **62**, 16356 (2000).
68. G. Mie, *Ann. Phys*. **25**, 377 (1908).
69. E. Kretschmann and E. Kroger, *J. Opt. Soc. Am*. **65**, 150 (1975).

Chapter 2 Emission from Glasses Doped with d^0 Ions

This chapter will describe the preparation, characterization, experimental results of glasses doped with d^0 ions. The glasses are characterized by measurements of optical absorption, fluorescence, and electron spin resonance. The possible mechanisms responsible for observations of tunable visible emissions are discussed.

2.1 Glasses containing d^0 ions

As mentioned in the general introduction, crystalline materials containing d^0 ions have received much attention because they demonstrate intense nonlinearity and attractive luminescent properties. However, little attention has been paid to glasses doped with d^0 ions although glasses are important host materials for REs, TMs, semiconductor quantum dots, and so on. Therefore, it is of interest to examine the optical properties of glasses doped with d^0 ions. In this section, the author has prepared d^0 ion-doped glasses and examined their optical properties. Six d^0 ions, i.e., Ti^{4+}, Zr^{4+}, Nb^{5+}, Ta^{5+}, Mo^{6+}, and W^{6+} are described. The author has found two interesting phenomena. Firstly, glasses doped with d^0 ions exhibit tunable visible emissions when they are excited by ultraviolet light. The emission wavelength strongly depends on the kinds of d^0 ions. Secondly, such glasses exhibit upconversion fluorescence with tunable wavelength when they are excited by a near-infrared femtosecond laser. The profile of emission spectrum obtained by excitation with ultraviolet light is almost the same as that excited by the near-infrared femtosecond laser for Ta^{5+}, Ti^{4+}, and Nb^{5+}-doped glasses. However, it is not the case for the other d^0 ions. The mechanism of the observed tunable visible emissions is discussed and a model for d^0 energy state responsible for such observations is proposed.

2.2 Sample preparation and measurements for characterizations

Glasses were prepared by a conventional melt quenching method. The as-received SiO_2 (99.99%), Na_2CO_3 (99.96%), $CaCO_3$ (99.99%), ZrO_2 (99.9%), TiO_2 (99.9%), Nb_2O_5 (99.9%), Ta_2O_5 (99.9%), MoO_3 (99.9%), and WO_3 (99.9%) were used as raw materials. A soda-lime silicate glass with a composition of $20Na_2O$-10CaO-$70SiO_2$ (in mol%) was chosen as glass matrix. The oxides containing d^0 ions were incorporated into glasses by substituting SiO_2. The glass composition was $20Na_2O$-10CaO-(70-x)SiO_2-xZrO_2 (or TiO_2, Nb_2O_5, Ta_2O_5, MoO_3, WO_3; in mol%). The weighted raw materials were thoroughly mixed for 10 h by ball milling. Then, the raw materials were put into a platinum crucible and preheated in an electric furnace at 1000 ℃ for 10 h. The preheated raw materials were transferred into a superburn furnace and melted at 1550 ℃ for 4 h in ambient atmosphere. The melt was taken out of the furnace, poured rapidly onto a stainless steel plate, and pressed with another plate to form glass. After the as-prepared glass was annealed at 570 ℃ for 5 h, it was cut and polished to obtain glass samples of 10×10×2 mm^3 for measurements. The glass matrix is referred to as SSC while the doped glasses are referred to as SSC: Zr^{4+}, SSC: Ti^{4+}, SSC: Nb^{5+}, SSC: Ta^{5+}, SSC: Mo^{6+}, and SSC: W^{6+}. For Ta^{5+}-doped glasses, strontium borate glass was also prepared with a composition of 33.3SrO-66.7B_2O_3 (in mol%, referred to as SrB_4O_7). 1 mol% Ta^{5+} ion was incorporated into the glass matrix by replacing Sr^{2+}. The doped glass is referred to as SrB_4O_7: Ta^{5+}. The glass was melted at 1300 ℃ for 1 h and treated in the same ways as the above-mentioned silicate glasses. For comparison, raw materials with low purity such as SiO_2 (99.0%), Na_2CO_3 (99.0%) and $CaCO_3$ (99.0%) were also used to prepare glasses for the purpose of studying the effect of purity on optical properties. Unless otherwise noted, all the glasses are referred to as those prepared by using raw materials with high purity.

Optical absorption spectrum was measured with a JASCO-V570

ultraviolet-visible-near infrared spectrophotometer. Measurements of excitation and emission spectra were performed with a HITACHI 850 fluorescence spectrophotometer. Electron spin resonance (ESR) measurements were carried out by using a JES-TE100 ESR spectrometer operating at X-band microwave frequency to detect paramagnetic defects and impurities in glasses. The fluorescence decay was obtained through a FluoroMax-P spectrophotometer by utilizing a pulsed Xe lamp as an excitation source. A regeneratively amplified Ti:sapphire laser was used for investigation of upconversion fluorescence with an operating wavelength of 780 nm, a repetition rate of 1 kHz, and a pulse duration of 130 fs. The laser was focused in the interior of the sample through an objective lens with a focal length of 150 mm. Upconversion fluorescence spectra were obtained by using the Hitachi 850 spectrophotometer.

A Ti:sapphire laser system with an oscillator (Tsunami, pumped by a solid-state laser Millennia, both provided by Spectra Physics Co. Ltd.) and an amplifier (Spitfire pumped by Merlin both provided by Spectra Physics Co. Ltd.) was used in this study. Fig. 2.1 shows a schematic diagram of upconversion fluorescence study the Ti:sapphire laser as a pump source. The emission from the canted sample was detected by the Hitachi 850 spectrophotometer. It should be noted that the photons emitted at the back of sample is usually used for supercontinuum observation. The excitation power of the Ti:sapphire laser was carefully controlled; otherwise the sample was easily damaged due to the high power density of the femtosecond laser.

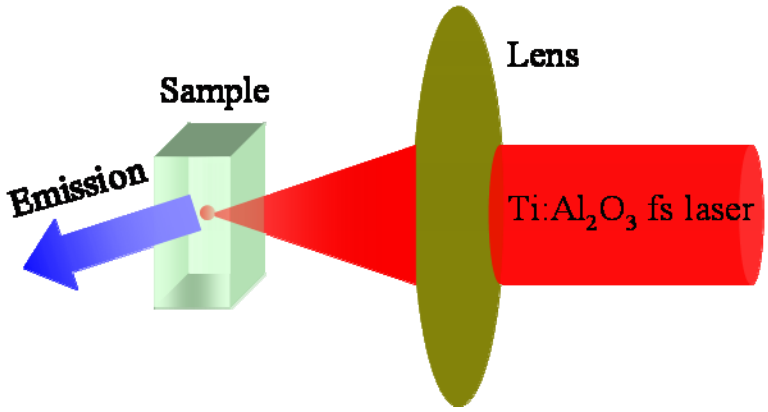

Fig. 2.1: A schematic diagram for measurements of upconversion fluorescence. A near-infrared Ti:sapphire femtosecond laser (λ=780 nm, 1 kHz repetition rate, and 130 fs pulse width) was used as a pump source. The laser beam was focused inside the sample and the emission was detected with Hitachi-850.

2.3 Optical properties

2.3.1 Ta^{5+}-doped glasses

Fig. 2.2 (a) shows the absorption spectra of SSC (black line) and SSC:Ta^{5+} (1 mol%, red line), along with their difference spectrum (blue line). SSC manifests a narrow absorption band with maximum absorption at 202 nm while SSC:Ta^{5+} manifests a much broader absorption band with maximum absorption at 222 nm. The difference spectrum processes a maximum absorption at 226 nm. The absorption coefficient is as large as 22.4 cm^{-1} for the difference spectrum. It is known that the absorption coefficient of defects in silica glass is usually less than 1 cm^{-1}. The very large value of absorption coefficient of SSC:Ta^{5+} seems to imply that the absorption is not caused by the formation of defects which may be brought about by Ta^{5+} incorporation into silicate glass. Instead, the author ascribes the absorption band to the charge transfer transition from O^{2-} to Ta^{5+}.

Fig. 2.2 (b) shows the excitation and emission spectra of SSC and SSC:Ta^{5+} prepared from raw materials with relatively low purity. SSC shows a weak emission band at 400 nm, while the excitation spectrum consists of two bands located at 220 and 262 nm, respectively. SSC:Ta^{5+} shows an emission band at 420 nm with the corresponding excitation band at 241 nm. For SSC:Ta^{5+}, the linewidth of the excitation band is about 37 nm, while it is about 115 nm for the emission band. Despite the observation of the emission band at 400 nm for SSC, the intensity is so weak that it is invisible to naked eyes when the glass is exposed to a 5 W ultraviolet lamp. The emission intensity of SSC:Ta^{5+} is about 100 times of that of SSC, so the former glass shows very intense blue emission when the glass is exposed to the same ultraviolet lamp. Actually, the emission in SSC is undetectable by the spectrophotometer when SSC is made from raw materials with high purity. The emission in SSC may arise from the B_2 defect or Fe^{3+} impurity imposed by raw materials. The presence of Fe^{3+} can be confirmed by the ESR spectrum, which will be presented later.

It is known that Ce^{3+}, Cu^{+} and Eu^{2+} ions are important blue emitters.[1] By comparing the emission intensity of SSC:Ta^{5+} with Ce^{3+}-doped borosilicate glass, it is found that the emission of SSC:Ta^{5+} is much more intense than that of Ce^{3+}-doped borosilicate glass. For glasses doped with Ce^{3+}, Cu^{+} and Eu^{2+} ions, reducing atmosphere is necessary to achieve high emission intensity. In contrast, Ta^{5+}-doped silicate glasses do not require control of any reducing or oxidation atmosphere; nevertheless, they show very intense blue emission. In addition, the preparation method is usually rather complex and it takes a long time to prepare glasses doped with Ce^{3+}, Cu^{+} and Eu^{2+} ions, while the conventional melt quenching method can be used to prepare Ta^{5+}-doped glasses so that large glasses can be easily fabricated. This is an advantageous point for practical applications of Ta^{5+}-doped glasses.

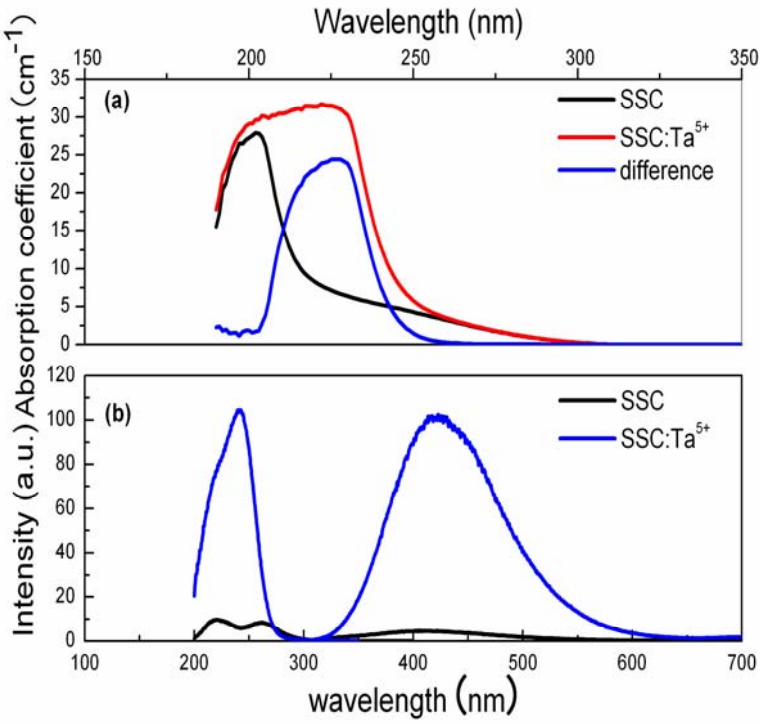

Fig. 2.2: (a) Optical absorption spectra of SSC (black line) and SSC: Ta^{5+} (red line) along with their difference spectrum (blue line). (b) Excitation (left) and emission (right) spectra of SSC (black line) and SSC:Ta^{5+} (blue line).

In order to detect the presence of possible paramagnetic defects in SSC:Ta^{5+}, ESR measurements were performed. Fig. 2.3 depicts ESR spectra of SSC and SSC:Ta^{5+} made from raw materials with low purity. Three signals are observed at g_1=4.264, g_2=2.073, and g_3=2.005 in both SSC and SSC:Ta^{5+}. The signals of SSC:Ta^{5+} resemble those of SSC. The dangling bond (E′ center) was reported to show an ESR signal at g≈2.005.[2] The signal position of E′ center readily changes with the preparation method. Therefore, the narrow signal at g_3=2.005 may be assigned to the dangling bond due to the deficient oxygen,[3] but impurities such as Fe^{3+} and Cu^{2+} can be responsible for this signal. Fe^{3+} usually manifests a signal at g=4.3,[4] so the g_1=4.264 signal can be ascribed to Fe^{3+} impurity responsible for the 400 nm emission band in SSC.[5-7] The broad signal at g_2=2.073 is presumably due to the impurities as well.

The three signals are also observed for Na_2CO_3 (99.0% purity) used as the raw material. Hence, the above three signals are thought to arise from the impurities like Fe^{3+} and Cu^{2+}.[8] When high purity raw materials are used, the signal at g_1=4.264 disappears while the other two still emerge.

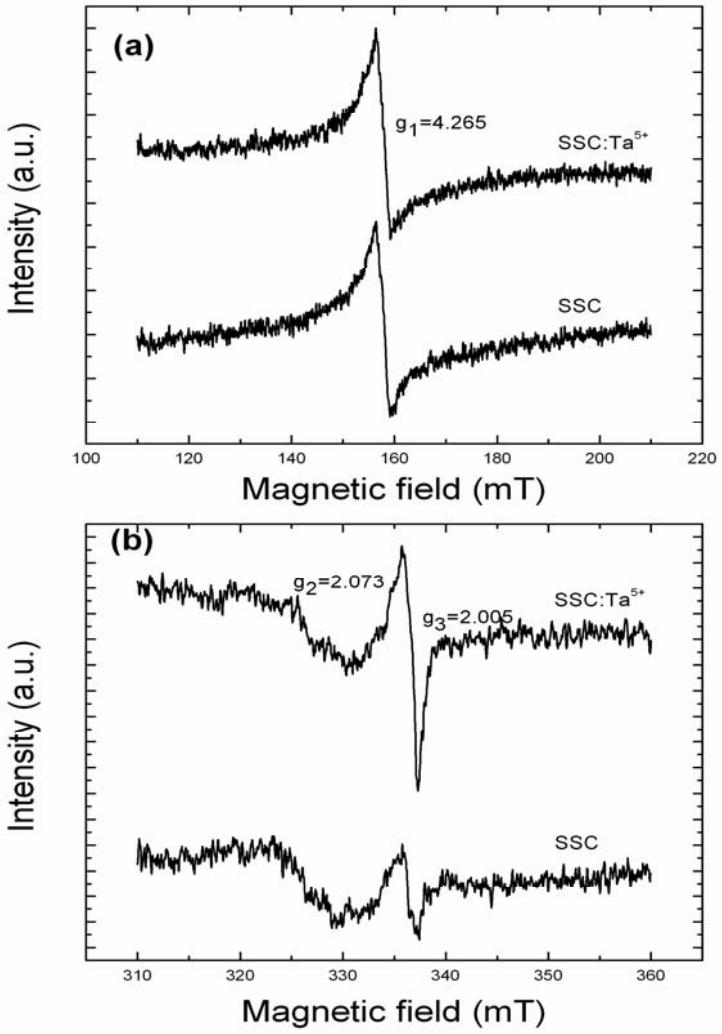

Fig. 2.3: ESR spectra of SSC and SSC:Ta^{5+}; (a) and (b) were recorded at low and high magnetic fields, respectively. The glasses are made from raw materials with relatively low purity. When raw materials with high purity are used, the signal at g_1=4.264 disappears, while the other two signals are still observed. All the measurements were performed at room temperature.

Fig. 2.4 illustrates the temperature dependence of emission spectrum of SSC:Ta^{5+} (1.0 mol%). In this measurement, the sample was mounted on a cold finger of an optical cryostat coupled to a closed-cycle helium refrigerator (Iwatani, CryoMini D105). The temperature was automatically tuned by a temperature controller (Iwatani, TCU-4) attached to the refrigerator. As the temperature increases, the emission spectrum manifests a red shift from 432 nm at T=15 K to 420 nm at T=300 K. On the other hand, the emission intensity gradually decreases with an increase in the temperature. The linewidth of the emission band increases with an increase in the temperature from ~107 nm at T=15 K to ~120 nm at T=300 nm.

Fig. 2.5 shows the fluorescence decay experimentally observed for SSC:Ta^{5+} along with the calculated curve. The decay curve significantly deviates from the single exponential function but can be described by the stretched exponential function that is expressed as I=1.35exp[-(t/45.7 μs)$^{0.92}$]. The decay time derived in this way is about 45.7 μs. From the Ta_2O_5 concentration dependence of the fluorescence decay, one can see that the decay time increases, reaches a maximum at 1.0 mol% Ta_2O_5, and then decreases with an increase of Ta_2O_5 concentration. All the experimental data can be explained in terms of the stretched exponential functions.

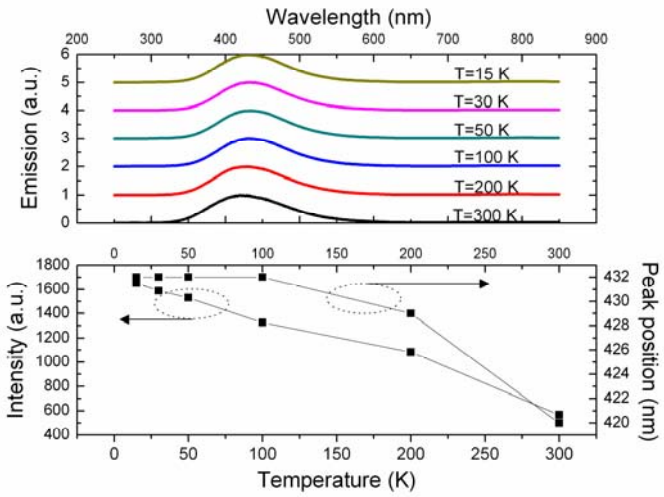

Fig. 2.4: The temperature dependence of emission spectrum of SSC:Ta^{5+} (1 mol%), as well as the plots of the emission intensity and peak positions against the temperature.

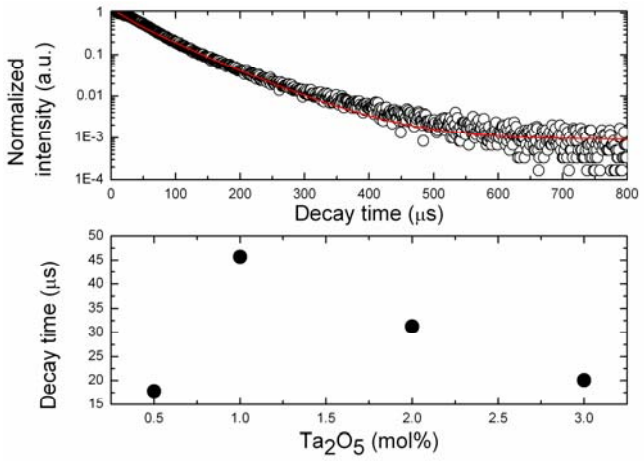

Fig. 2.5: (a) Experimental fluorescence decay curve of SSC:Ta^{5+} (1.0 mol%, black circles) and the fit curve by the stretched exponential function given by $I=1.35\exp[(-t/45.7\ \mu s)^{0.85}]$ (red line). (b) The fluorescence decay time as a function of Ta_2O_5 concentrations from 0.5 to 3.0 mol%.

When SSC:Ta^{5+} is exposed to a femtosecond laser, an intense blue emission can be observed; SSC also yields a very weak bluish emission. Fig. 2.6 (a) shows the emission spectra of SSC and SSC:Ta^{5+} excited by the femtosecond laser. The peaks of emission are observed at 350 nm for SSC and 415 nm for SSC:Ta^{5+}. The two spectra are quite different from each other from a standpoint of both emission intensity and spectral profile, implying that they do not arise from the same emitting center. Fig. 2.6 (b) compares the emission spectra obtained by excitation with ultraviolet light at 245 nm and with the femtosecond laser at 780 nm for SSC:Ta^{5+}. The figure shows that the two spectra are almost identical to each other, suggesting that the emission brought about by the two excitation sources originates from the same center. Fig. 2.6 (c) illustrates the pump power dependence of the integrated intensity for the blue emission at 415 nm for SSC:Ta^{5+}. The slope of log (intensity)-log (pump power) line is close to unity when the pump power is low, while it gradually decreases with an increase in the pump power. A similar phenomenon was observed in REs-doped materials, and ascribed to the saturation of absorption. Here, the decrease of the slope may be associated with a damage of the glass caused by the high power density of the femtosecond laser. Indeed, a gray spot was observed at the focus of the femtosecond laser. The gray area does not show emission when it is irradiated with ultraviolet light. Also, it has no ESR signal.

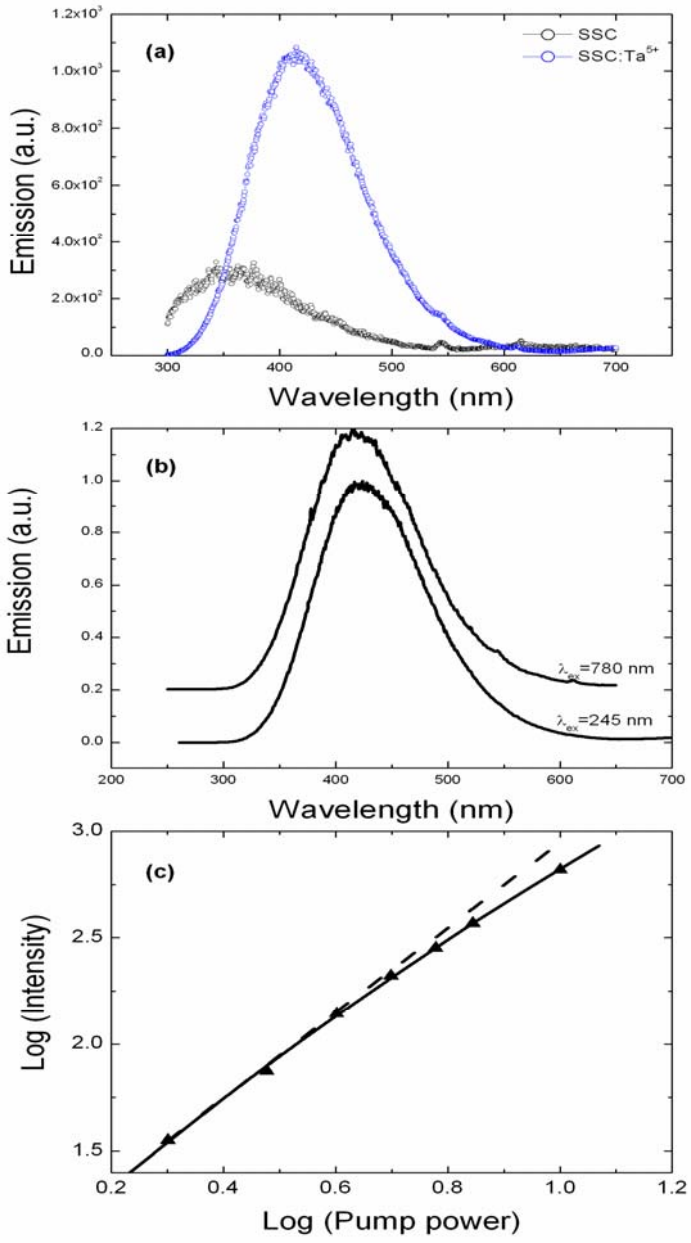

Fig. 2.6: (a) Emission spectra of SSC (black circles) and SSC:Ta^{5+} (blue circles) when excited by the femtosecond laser. (b) A comparison of emission spectra between ultraviolet light and femtosecond laser excitations for SSC:Ta^{5+}. (c) Log-log plot between the integrated emission intensity and pump power for the upconversion fluorescence of SSC:Ta^{5+}. The triangles are the experimental data and the dashed line is a straight line with a slope of 2.0.

Even when the borate glass is used as a host material, the spectral profiles are almost the same. Fig. 2.7 depicts the absorption spectrum (a), excitation and emission spectra (b), fluorescence decay curve (c), and emission spectra excited by the ultraviolet light and femtosecond laser (d). The absorption spectrum of the host material without Ta^{5+} manifests a maximum intensity at 208 nm, while the wavelength of the maximum shifts to 228 nm by Ta^{5+} incorporation. The difference spectrum exhibits intense maximum intensity at 244 nm with an absorption coefficient as large as 15 cm^{-1}. The excitation spectrum of SrB_4O_7:Ta^{5+} possesses a peak at 240 nm with a linewidth of 26 nm. The emission intensity peaks at 420 nm, and a linewidth of the spectrum is114 nm. It is found that the excitation band of SrB_4O_7:Ta^{5+} is narrower by 11 nm than that of SSC:Ta^{5+}, although the emission bands of these two glasses have similarities in both emission peak position and lineshape. Also, the fluorescence decay significantly deviates from the single exponential function. The decay time was determined to be ~10.7 μs by analyzing the experimental data with the extended exponential function that is denoted as I=2.88exp[-(t/10.7)$^{0.57}$]. This value of relaxation time is about 35 μs shorter than that of SSC:Ta^{5+}. When SrB_4O_7:Ta^{5+} is exposed to the femtosecond laser, the glass manifests a blue emission as shown in Fig. 2.7 (d). The profile of emission spectrum obtained by excitation with the femtosecond laser at 780 nm is almost identical to that obtained by excitation with ultraviolet light at 240 nm. This result indicates that the blue emission from SSC:Ta^{5+} and SrB_4O_7:Ta^{5+} originates from the same emitting center regardless of the host materials.

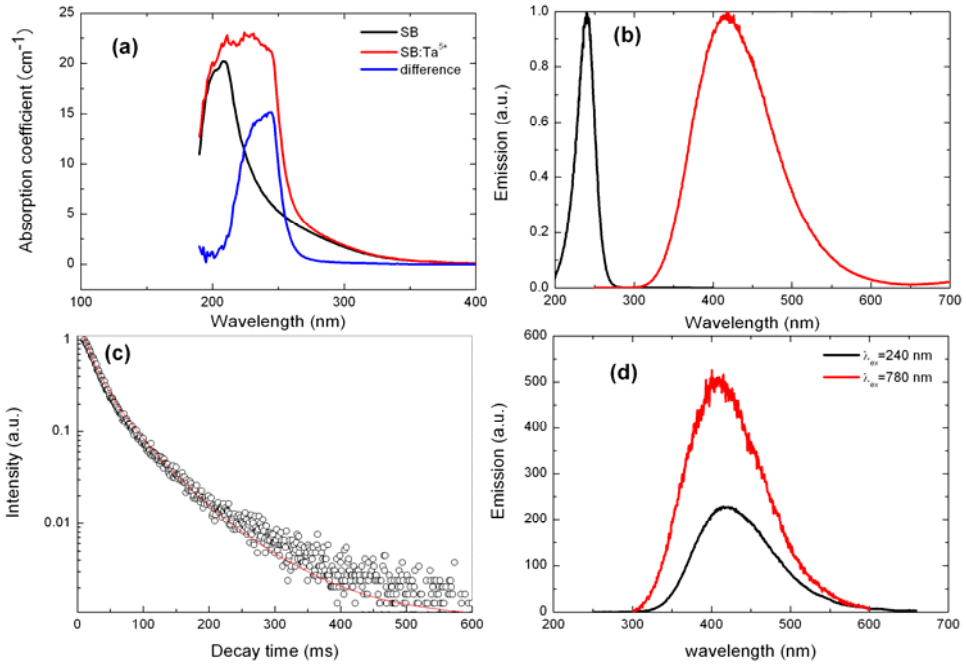

Fig. 2.7: (a) Absorption spectra of SrB_4O_7 (black line), SrB_4O_7: Ta^{5+} (red line) and their difference (blue line). (b) Excitation (black line) and emission (red line) spectra of SrB_4O_7: Ta^{5+}. (c) Fluorescence decay curve of SrB_4O_7: Ta^{5+} (black circles) and the fit curve (red line) calculated by an extended exponential function expressed by $I=2.88exp[(-t/10.7\ \mu s)^{0.57}]$. (d) Emission spectra obtained by excitation with ultraviolet light at 240 nm (black line) and femtosecond laser at 780 nm (red line).

As mentioned above, little attention has been paid to the fluorescence properties of d^0 ion-doped glass materials so that the origin for the fluorescence is not so clear. In contrast to the d^0 ion-doped amorphous materials, fluorescence properties of various crystalline materials based on d^0 ion such as tantalates have been extensively studied in the past by Blasse *et al.*[9-13] As shown in Table 2.1, some characteristics can be summarized from the spectral properties of crystalline tantalates reported previously; (1) the absorption edges of these tantalates usually occur in the ultraviolet wavelength region and coincide with the corresponding excitation spectra, (2) the excitation spectra are located in the ultraviolet region, while the emission spectra are observed in the ultraviolet or blue region, (3) large Stokes shifts exist in most of these tantalates, (4) the emission is efficient at low temperatures and thermal quenching takes place at room temperature, (5) in tatanlate, octahedral TaO_6 and tetrahedral TaO_4 are two important emitting centers, and Ta-O-Ta bond angles and lengths have significant effects on the properties of spectra. Nevertheless, the nature of the fluorescence is still unclear. The experimental data only present restricted information due to the fact that the spectra consist of very broad emission and excitation bands which do not exhibit any vibrational structures.

Since the blue emission is not observed from both undoped silicate and borate hosts, it is reasonable to ascribe the emergence of the blue emission to the incorporation of Ta^{5+} ions. The profile of emission spectra of Ta^{5+}-doped borate glass is very similar to that of Ta^{5+}-doped silicate glass, so that one can rule out the possibility of oxygen-related defects that may be responsible for the blue emission. The tantalum belongs to group 5 in the periodic table, and usually exists as a pentavalent state. One speculation is that the blue emission is associated with polyhedral groups consisting of tantalum and oxygen. Considerable efforts have been made on emission properties of crystallite materials containing TMs with d^0 or d^{10} configurations in the past decades. The polyhedra, i.e., TaO_6 and TaO_4, are known as rather efficient fluorescent centers via metal-to-ligand transition.

The ultraviolet-excited blue emission can be interpreted in terms of the presence of Ta^{5+} $5d^0$ energy state, as proposed in previous reports.[14,15] Because the SSC:Ta^{5+} and SrB_4O_7:Ta^{5+} are insulators, the Ta^{5+} $5d^0$ energy level is plausibly localized in the band gap. The valence band is composed of 2p orbitals of O^{2-}. An electron in O^{2-} 2p orbital absorbs an ultraviolet photon and is excited into the localized Ta^{5+} $5d^0$ energy level. The excited electron relaxes to the lowest vibrational level via nonradiative decay; eventually the recombination of electron-hole pair gives rise to a blue photon.

In general, an upconversion behavior can be understood in terms of the energy transfer, excited state absorption, cooperative upconversion, and photon avalanche. These processes require a metastable state existing between the ground state and the upper state so that the pumping photons are absorbed succeedingly rather than simultaneously.[1] A pumping photon can excite one electron from the ground state to the metastable state in the mechanisms of energy transfer, excited state absorption, and cooperative upconversion. Therefore, an absorption band is expected at ~1.59 eV in SSC:Ta^{5+} and SrB_4O_7: Ta^{5+}. However, the absence of this band in the Ta^{5+}-doped glasses suggests that the contribution of the above three processes is negligible. In case of photon avalanche, a critical pumping power should exist, accompanied by a sudden change in the slope.[16] This phenomenon has not been detected in this study. Another mechanism can be proposed; an electron in the ground state is excited into a real intermediate state by absorbing simultaneously two pumping photons and then further pumped into the upper state. If this is the case, an absorption band at 3.18 eV (twice the energy of one pumping photon) should occur. This mechanism seems negligible because of the absence of the expected absorption band at 3.18 eV. In general, the intensity of femtosecond laser is high enough (>100 TW/cm^2) to generate multiphoton absorption in glass matrix. Therefore, active electron-hole pairs can be formed in glasses through multiphoton excitation. The following mechanism is proposed to interpret the appearance of the blue upconversion fluorescence. One electron is driven out of the O^{2-} $2p$ orbitals by multiphoton absorption of the incident

laser and then captured by the localized Ta^{5+} $5d^0$ energy level to form one electron-hole pair. The recombination of electron-hole pair takes place accompanied by the appearance of one blue photon.

Table 2.1: Luminescence data of crystalline tantalates and Ta^{5+}-doped glasses.

Materials	Emission peak (nm)	Excitation peak (nm)	Absorption edge (nm)	Stokes shift (10^3 cm^{-1})
$LiTaO_3$ (4.2 K)	340	235	245	14.0
$NaTaO_3$ (4.2 K)	440	285	285	12.3
$KTaO_3$ (4.2 K)	490	330	330	10.2
$YTaO_3$ (300 K)	335	229	225	13.8
$LaTaO_3$ (77 K)	395	254	260	14.1
SrB_4O_7: Ta^{5+} (300 K)	419	240	259	17.8
SSC:Ta^{5+} (300 K)	420	245	247	16.9

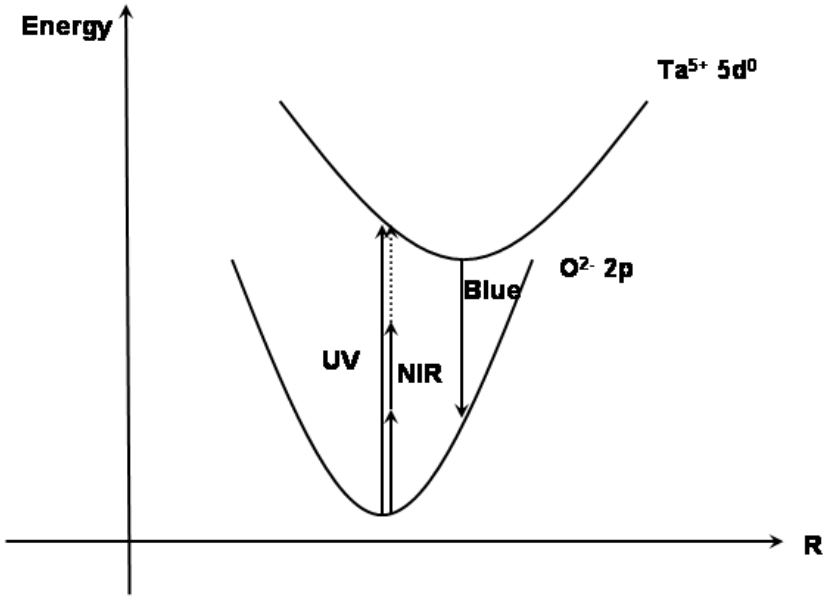

Fig. 2.8: Configurational coordinate diagram tentatively proposed to interpret the blue emission observed by excitation with ultraviolet light and near-infrared femtosecond laser. Here, UV and NIR refer to ultraviolet and near-infrared light, respectively. The ground state in this system is oxygen 2p orbital while the excited state is Ta^{5+} $5d^0$ level. The electron in oxygen 2p orbital can absorb either one ultraviolet photon or multiple near-infrared photons and be excited to Ta^{5+} $5d^0$ level, accompanied by an output of one blue photon.

2.3.2 Ti^{4+}-doped glasses

Inspired by the results of Ta^{5+}-doped glasses, the author has extended his study to other d^0 ions. Ti^{4+} ion belongs to the $3d^0$ ions with electronic configuration of [Ar] $3d^0$. It is expected that Ti^{4+}-doped glasses can show visible emission when excited by ultraviolet light and a near-infrared femtosecond laser. To confirm this, the glass of SSC:Ti^{4+} was prepared and investigated.

Fig. 2.9 (a) depicts optical absorption spectra of SSC and SSC:Ti^{4+}, along with the difference between them. Compared with SSC, the absorption spectrum of SSC:Ti^{4+} comprises a much broader band extending to low energy region of about 354 nm. In case of SSC:Ti^{4+}, an abrupt increase in absorption appears at about 335 nm to 318 nm. The broad band of SSC:Ti^{4+} can be assigned to Ti-O charge transfer transition. The shift in the absorption edge compared to that of bulk crystalline anatase which has an absorption edge of about 3.3 eV (376 nm) may be due to the localization of Ti-O bond in silicate network. There is a report on the difference in the optical absorption spectrum between anatase thin film and bulk anatase single crystal. The difference is attributed to a small size of anatase nanocrystallites located in amorphous titania walls in the thin film.[22] Thus, the position of Ti-O charge transfer band is efficiently affected by the coordination state of Ti^{4+}. It is noteworthy that the absorption spectrum of SSC:Ti^{4+} is much broader than that of SSC:Ta^{5+}, indicating that efficient photo excitation takes place in a wide range of ultraviolet energy. The SSC:Ti^{4+} clearly shows greenish emission under ultraviolet light irradiation. The emission and excitation spectra are illustrated in Fig. 2.9 (b). The emission spectrum of SSC:Ti^{4+} is composed of a broad band peaking at 496 nm and extends from 343 to 743 nm, and the excitation spectrum centering at 262 nm covers a wide energy range from 200 to 331 nm. The Stokes shift is as large as 18005 cm^{-1}. The profile of the excitation spectrum is well consistent with the difference in the absorption spectra as shown in Fig.

2.9 (a) except for a little shift in peak position. The excitation spectrum does not overlap the emission spectrum, indicating that the excitation process of Ti-O charge transfer can efficiently contribute to the greenish emission. The colors of emission for SSC:Ti^{4+} and SSC:Ta^{5+} are quite different from each other, as seen in the emission spectra of Fig. 2.9 (b). The capability of manipulating emission wavelength by simply utilizing various d^0 ions leads to possibility to use these glasses as novel luminescent materials.

Fig. 2.9 (c) illustrates the fluorescence decay curve at 496 nm obtained at room temperature (black circles). The experimental data are not consistent with the single exponential function but satisfy the stretched exponential function as given by[23]

$$I(t) = 1.69\exp[-(t/44.7\ \mu s)^{0.477}]. \quad (2.1)$$

One can see that the emission at 496 nm possesses a decay time of 44.7 μs but the practical radiative process is complex. In addition, the experimental data can also be fitted by the summation of single exponential functions given by

$$I(t)=0.74\exp(-t/33.9\ \mu s)+0.49\exp(-t/251\ \mu s). \quad (2.2)$$

Therefore, one can think that the fluorescence decay at 496 nm undergoes a fast decay with 33.9 μs and a slow one with 251 μs. The fast decay time is close to that obtained in Eq. (2.5), suggesting that both of two fitting methods can be used to estimate the fluorescence decay behavior of SSC:Ti^{4+}.

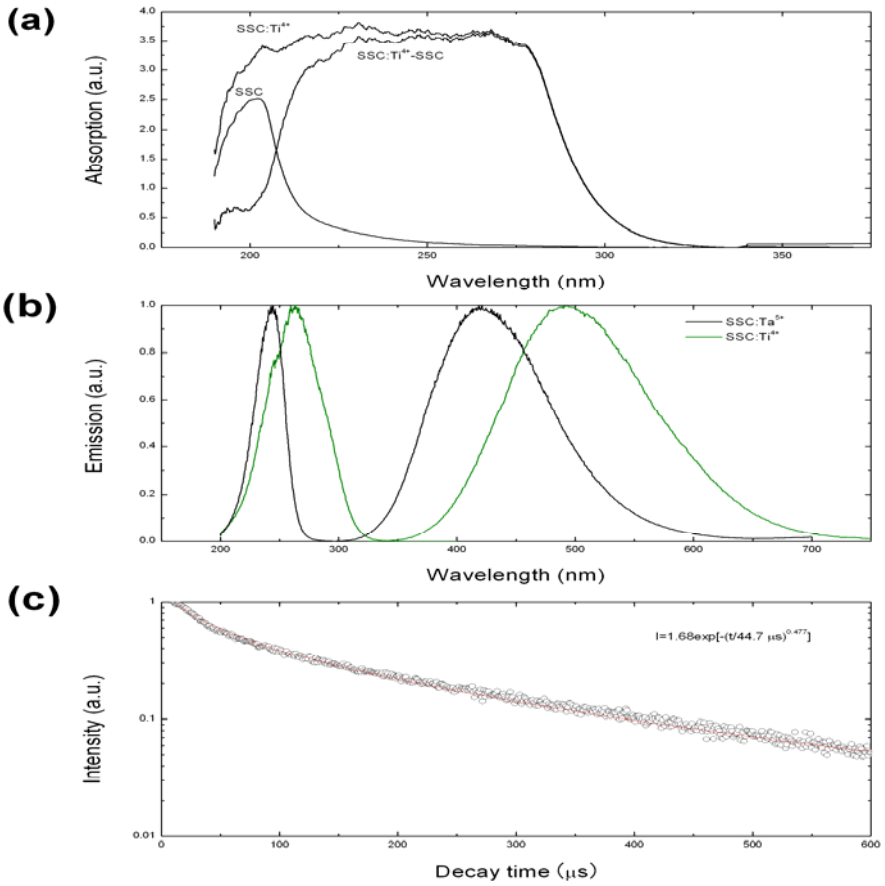

Fig. 2.9: (a) Optical absorption spectra of SSC, SSC:Ti^{4+} and the difference in optical absorption spectrum between SSC and SSC:Ti^{4+}. (b) Normalized excitation spectrum (left green line, λ_{em}=496 nm) and emission spectrum (right green line, λ_{ex}=262 nm) for SSC:Ti^{4+}, as well as normalized excitation spectrum (lefft black line, λ_{em}=420 nm) and emission spectrum (right black line, λ_{ex}=240 nm) for SSC:Ta^{5+}. (c) Fluorescence decay curve (black circles) of SSC:Ti^{4+} when the emission wavelength was monitored at 496 nm, along with the curve (red line) drawn with $I(t)=1.69\exp[-(t/44.7\ \mu s)^{0.477}]$.

As mentioned in the preceding sections, the origin of the emission from d^0 ion-doped glass materials has not been completely understood yet. Incorporation of the d^0 ions into silicate glasses may cause the formation of some defects, and as a consequence, the induced defects may give rise to the emission observed. However, ESR measurements have not shown any evidence for the presence of well-known paramagnetic defects such as non-bridging oxygen hole center (NBOHC, ≡Si-O↑, where ↑ means one unpaired electron) and peroxy radicals (≡Si-O-O↑), E′ (≡Si↑). The absorption spectra as well as ESR signals of SSC:Ti^{4+} can rule out the presence of other valence states of titanium ions such as Ti^{2+}, Ti^{3+}.[24,25] As mentioned above, the absorption coefficient due to defects in silica glass is less than $1cm^{-1}$ as reported previously, while SSC:Ti^{4+} possesses an absorption coefficient as large as $36cm^{-1}$, as shown in Fig. 2.9 (a). When SSC:Ti^{4+} was exposed to a 254 nm ultraviolet lamp, it exhibited an intense greenish emission, whereas no emission could be observed in SSC. This fact indicates that the observed greenish emission is closely associated with the excitation of the Ti-O charge transfer band. The Ti^{4+}-doped $MgAl_2O_4$ single crystal was reported to yield intense blue emission at 490 nm when excited at 280 nm; the emission was assigned to a relaxation process of $Ti^{4+}\rightarrow O^{2-}$ charge transfer.[26] The difference in color between SSC:Ti^{4+} and $MgAl_2O_4$: Ti^{4+} crystal is ascribable to the fact that the latter shows a narrow emission band reflected by the crystal field for Ti^{4+} ions. This can provide further evidence that the 496 nm emission is assigned to a relaxation process of $Ti^{4+}\rightarrow O^{2-}$ charge transfer transition.

Fig. 2.10 (a) depicts the emission spectrum obtained by the excitation with the femtosecond laser at 780 nm, along with that obtained by the ultraviolet light excitation at 262 nm for comparison. Greenish emission could be clearly observed from SSC:Ti^{4+} while blue emission from SSC:Ta^{5+} when pumped by the femtosecond laser. The spectral profile when pumped by the femtosecond laser is almost the same as that excited by the ultraviolet light, indicating that the emission in both cases comes from an identical origin. The log-log plot of the upconversion fluorescence intensity versus

pump power for the femtosecond laser excitation is shown in Fig. 2.10 (b). The upconversion fluorescence intensity is related to the pump power through the following formula $I \propto P^n$, where I is the integrated intensity of emission, P the pump power, and n the number of photon involved in the multiphoton absorption process. The slope of the curve as shown in Fig. 2.10 (b) gradually decreases as the pump power increases. The slope takes an initial value of ~3.0, and is eventually saturated to unity. The decrease in the slope may be associated with breaking of glass network or emergence of color centers induced by the ultrashort pulsed laser with high power density.

A localized Ta^{5+} $5d^0$ energy level was proposed to interpret the appearance of blue emission in case of SSC:Ta^{5+} as mentioned previously. The similarity in spectral characteristics between SSC:Ta^{5+} and SSC:Ti^{4+} suggests that the $3d^0$ energy level of Ti^{4+} may play an indispensable role in emission processes as well. In both cases of the ultraviolet and the femtosecond laser excitations, Ti^{4+} $3d^0$ energy level can accept an excited electron and contribute to the greenish emission. In general, the intensity of femtosecond pulsed laser is high enough (>100 TW/cm^2) to generate multiphoton absorption in glass matrix. Therefore, active electron-hole pairs can be formed in glasses through multiphoton process. In the present case, one electron is driven out from the O^{2-} 2p orbital by multiphoton absorption of the incident laser and then captured by the localized Ti^{4+} $3d^0$ energy level. Since the ultraviolet excitation energy (4.73 eV, 262 nm) for the 496 nm emission is almost three times larger than that of the femtosecond laser (1.59 eV, 780 nm), an electron in O^{2-} 2p orbital is supposed to be directly excited into Ti^{4+} $3d^0$ energy level by absorbing simultaneously three photons of the femtosecond laser. Eventually, the recombination of the electron and positive hole contributes to the observed upconversion fluorescence.

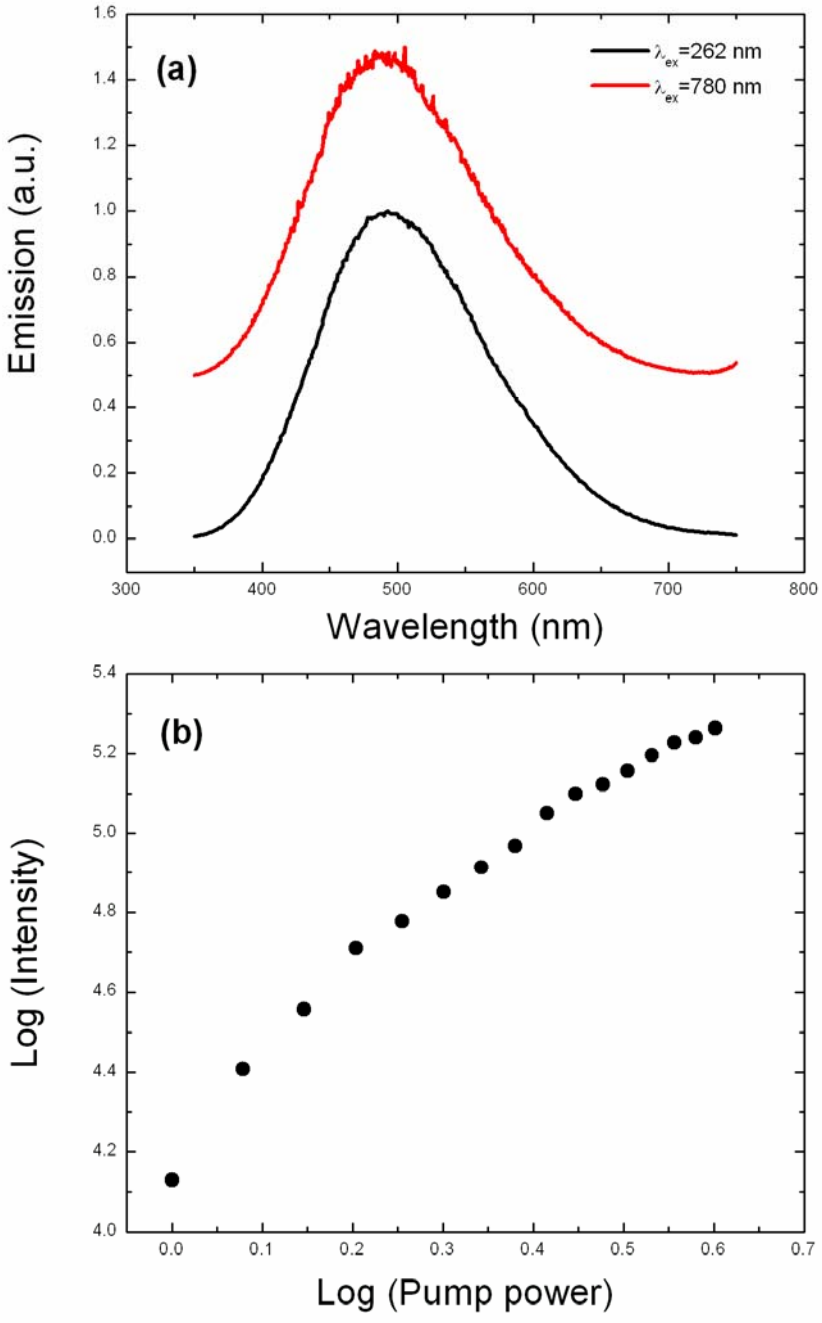

Fig. 2.10: (a) Emission spectra for SSC:Ti^{4+} when excited by ultraviolet light at 262 nm and the femtosecond laser at 780 nm. (b) Log-log plot of the integrated emission intensity versus pump power for SSC:Ti^{4+}.

2.3.3 Zr^{4+}, Nb^{5+}, Mo^{6+}, and W^{6+}-doped glasses

In this section, the experimental results of other four d^0 ions; i.e., Zr^{4+}, Nb^{5+}, Mo^{6+}, and W^{6+}, incorporated in silicate glass are presented and compared with each other. All the six d^0 ions are discussed for the purpose of emphasizing the ability to manipulate emitting colors by only using d^0 ions as dopants.

Fig. 2.11 summarizes the excitation and emission spectra of the six d^0 ion-doped soda-lime silicate glasses. It is obvious that the spectral profiles including peak positions are different from each other. The data about optical properties of glasses doped with the six d^0 ions are summarized in Table 2.2. The results illustrate that their excitation spectra are located in the ultraviolet wavelength region as narrow bands, while their emission spectra appear in the visible wavelength region as broad bands with the linewidth larger than 100 nm. What the author wants to emphasize is that these glass materials yield various colors due to emission, depending on the kinds of d^0 ions. For instance, the emission from SSC:Zr^{4+}, SSC:Ta^{5+}, and SSC:W^{6+} appears in the blue wavelength region, SSC:Ti^{4+} and SSC:Nb^{5+} have greenish emissions, and the emission of SSC:Mo^{6+} extends even to the yellow-orange wavelength region. The results indicate that d^0 ion-doped glasses can be utilized to tune the emission colors.

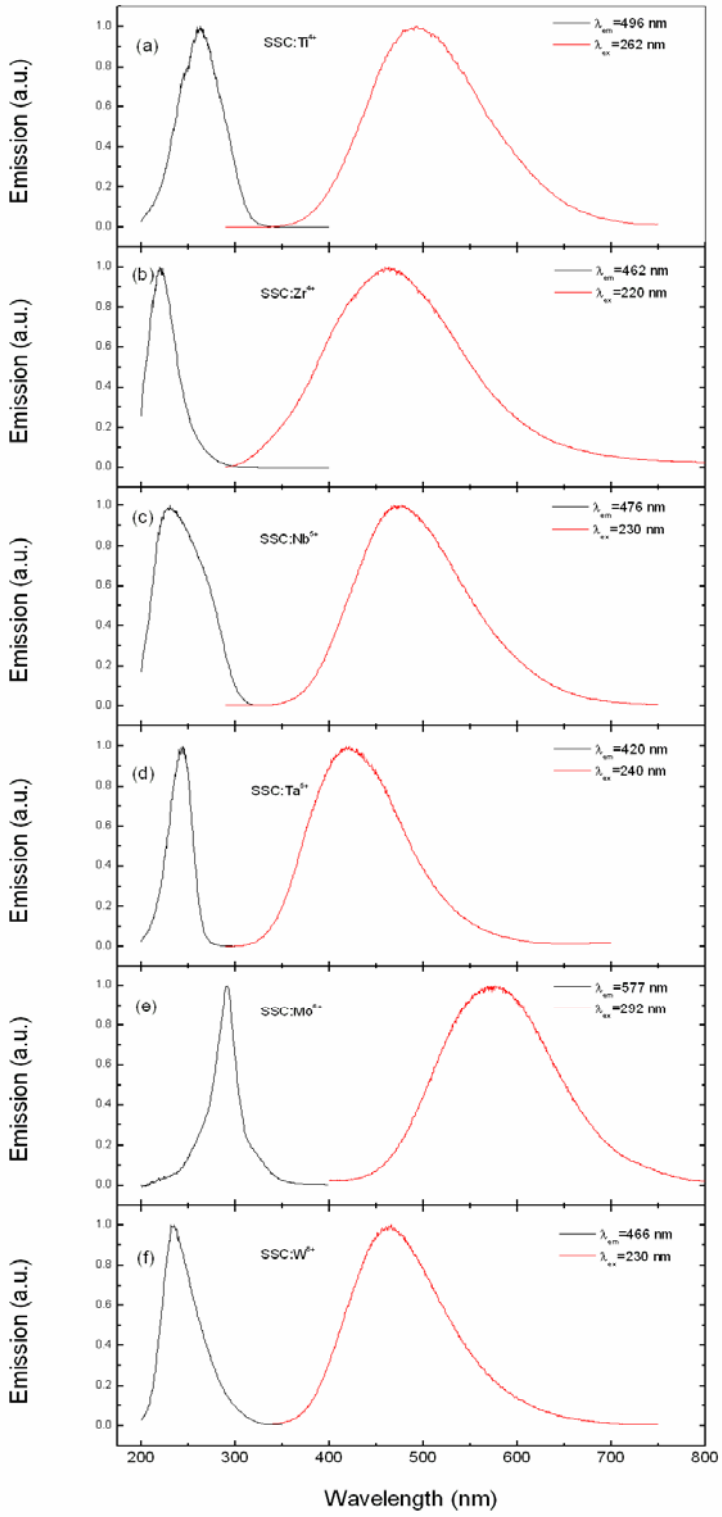

Fig. 2.11: Excitation and emission spectra of SSC:Ti^{4+} (a), SSC:Zr^{4+} (b), SSC:Nb^{5+} (c), SSC:Ta^{5+} (d), SSC:Mo^{6+} (e), and SSC:W^{6+} (f).

Table 2.2: Excitation, emission and decay properties of d^0 ion-doped silicate glasses. All the decay times were determined by the stretched exponential functions. The emission intensity of SSC:Zr^{4+} and SSC:Mo^{6+} is so weak that their corresponding decay times can not be determined by this method.

	SSC:Ti^{4+}	SSC:Zr^{4+}	SSC:Nb^{5+}	SSC:Ta^{5+}	SSC:Mo^{6+}	SSC:W^{6+}
Ex peak (linewidth)	263 (56.5)	220 (34.5)	231 (68.5)	244 (28.5)	292 (26.5)	235 (43.0)
Em peak (linewidth)	493 (145)	460 (166)	469 (138)	419 (116)	577 (147)	466 (118)
Stokes shift (cm^{-1})	17738	23715	21968	17117	16916	21094
Decay time (μs)	44.7	/	202	45.7	/	115

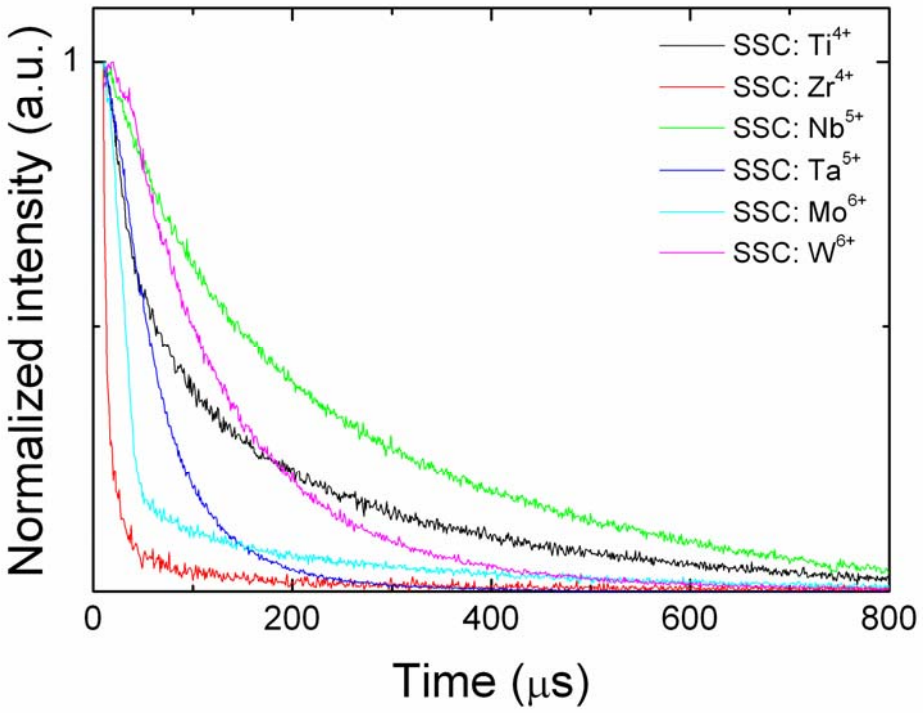

Fig. 2.12: Fluorescence decay curves of d^0 ion-doped silicate glasses.

Fig. 2.12 displays fluorescence decays of the d^0 ion-doped glasses. The fluorescence of various d^0 ion-doped glasses shows decay behaviors different from each other. When the d^0 ion-doped glasses are exposed to the femtosecond laser, all of them yield emission in the visible range corresponding to various colors. Fig. 2.13 illustrates the emission spectra obtained by excitation with the ultraviolet light and those obtained by excitation with the femtosecond laser. The profiles of emission spectra by the excitation with the femtosecond laser and the ultraviolet light are almost the same as each other for SSC: Ti^{4+}, Nb^{5+} and Ta^{5+}, while it is not the case for the other ions. The emission spectrum of SSC: Zr^{4+} is composed of a dominant peak at 398 nm and a shoulder at 345 nm. The peak position of maximum emission intensity for SSC: Mo^{6+} is almost independent of the excitation source, although a component in the low energy region is obviously observed for the emission spectrum under excitation by the femtosecond laser. The emission peak of SSC: W^{6+} is located at 464 nm when excited by the ultraviolet light, while it shifts to 512 nm when pumped by the femtosecond laser. Therefore, a blue color is seen when SSC: W^{6+} is exposed to the ultraviolet light and a clear green color is observed for the near-infrared femtosecond laser excitation.

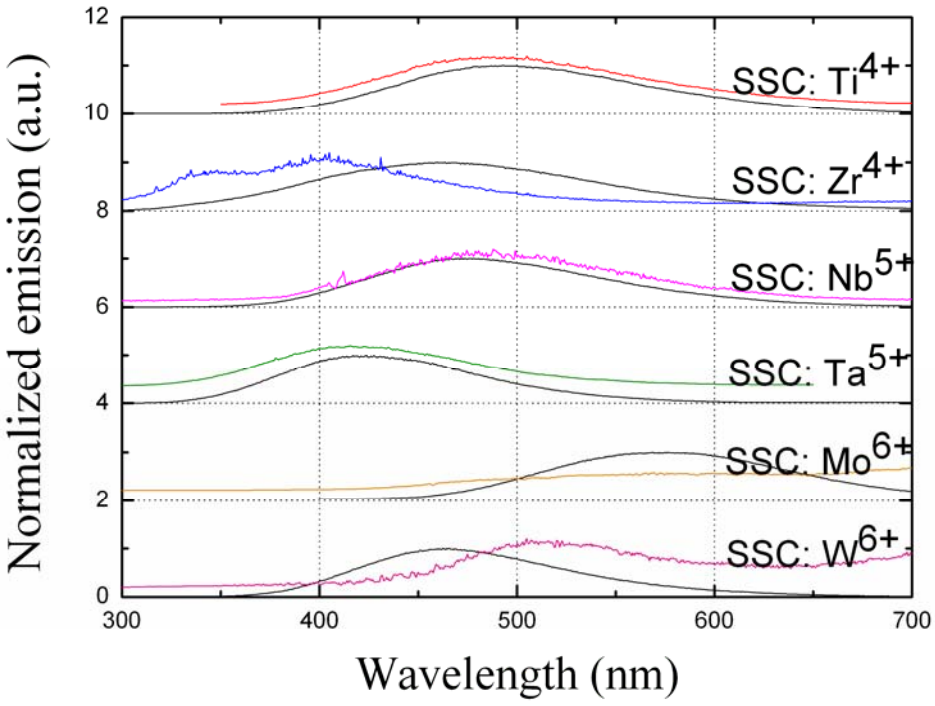

Fig. 2.13 Emission spectra excited by the ultraviolet light (black lines) and the femtosecond laser (color lines) for the silicate glasses doped with d^0 ions. All the spectra are normalized.

References

1. D. P. Chen, H. Miyoshi, and T. Akai, *Appl. Phys. Lett*. **86**, 231908 (2005).
2. J. Qiu, K. Miura, T. Suzuki, and T. Mitsuyu, *Appl. Phys. Lett*. **74**, 10 (1999).
3. B. Hua, Ph.D thesis, Kyoto University (2006).
4. K. Tanaka, PhD Thesis, Kyoto University (1990).
5. Y. Wu and A. Stesmans, *Phys. Rev. B* **38**, 2779 (1988).
6. K. Moritani, I. Takagi, and H. Moriyama, *J. Nucl. Mater*. **329–333**, 988 (2004).
7. K. Kajihara, L. Skuja, M. Hirano, and H. Hosono, *J. Non-Cryst*. *Solids* **345-346**, 219-223 (2004).
8. R. C. Nicklin, H. A. Farach, and C. P. Poole, Jr., *J. Chem. Phys*. **65**, 2998 (1976)
9. G. Blasse and A. Bril, *J. Solid State Chem*. **3**, 69 (1971).
10. G. Blasse, *J. Solid State Chem*. **7**, 169 (1973).
11. M. Lammers and G. Blasse, *Mater. Res. Bull*. **19**, 759 (1984).
12. L. Dehaart. H. Boessenkool, and G. Blasse, *Mater. Chem. Phys*. **13**, 85 (1985).
13. G. Blasse, G. Dirksen, Z. Pei, G. Wehrum, and R. Hopper, *Chem. Phys. Lett*. **215**, 363 (1993).
14. X. Meng, K. Tanaka, S. Murai, K. Fujita, K. Miura, and K. Hirao, *Opt. Lett*. **31**, 2867 (2006).
15. X. Meng, K. Tanaka, K. Fujita, and S. Murai, *Appl. Phys. Lett*. **90**, 051917 (2007).
16. J. S. Chivian, W. E. Case, and D. D. Eden, *Appl. Phys. Lett*. **35**, 124 (1979).
17. X. Jiang, T. Herricks, and Y. Xia, *Adv. Mater*. **15**, 1205 (2003).
18. M. Anpo, T. Shima, S. Kodama, and Y. Kubokawa, *J. Phys. Chem*. **91**, 4305 (1987).
19. G. A. Battiston, R. Gerbasi, M. Porchia, and L. Rizzo, *Chem. Vap. Deposition*, **5**, 73 (1999).
20. J. Livage, M. Henry, and C. Scanchez, *Prog. Solid State Chem*. **18**, 259 (1988).

21. U. Bach, D. Lupo, P. Comte, J. E. Comte, J. E. Moser, F. Weissortel, J. Salbeck, H. Spreitzer, and M. Gratzel, *Nature (London)* **395**, 583 (1993).
22. D. Ehrt, M. Leister, and A. Matthai, Jr., *Phys. Chem. Glasses* **42**, 231 (2001).
23. M. Yan, L. J. Rothberg, F. Papadimitrakopoulos, M. E. Galvin, and T. M. Miller, *Phys. Rev. Lett*. **73**, 744 (1994).
24. D. R. Gamelin, M. Wermuth, and H. V. Gudel, *J. Lumin*. **83-84**, 405 (1999).
25. L. H. C. Andrade, S. M. Lima, A. Novatski, P. T. Udo, N. G. C. Astrath, A. N. Medina, A. C. Bento, M. L. Baesso, Y. Guyot, and G. Boulon, *Phys. Rev. Lett*. **100**, 027402 (2008).
26. T. Sato, M. Shirai, K. Tanaka, Y. Kawabe, and E. Hanamura, *J. Lumin*. **114**, 155 (2005).

Chapter 3 Preparation and Characterization of Random Structures Composed of Metal Nanoparticles

Silver nanoparticles are used as scattering centers for random systems in this thesis. The preparations of samples include those of anisotropic silver nanoparticles, silver nanoprisms, polymer films embedded with anisotropic silver nanoparticles and silver nanoprisms, and *in situ* synthesized PVA-Ag-dye films. The author will briefly introduce preparation procedures below.

3.1 Anisotropic silver nanoparticles

In order to enhance the interaction between silver nanoparticles and dye molecules, it is better to manipulate the SPR profile to make it close to the emission peak of R6G since the SPR signal occurs at around 400 nm for smaller spherical silver nanoparticles. There are two alternative ways. One is to control the morphology of silver nanoparticles, while the other is to increase the particle size to some extent but can not be too large since the scattering intensity reaches a maximum at an intermediate size. For instance, at the wavelength λ=580 nm (for R6G) and the surrounding medium of n=1.5, the scattering intensity of silver nanoparticles has a peak at particle radius of 50 nm. Therefore, the author chose to synthesize silver nanoparticles with anisotropic morphology and particle size of ~50 nm.

Anisotropic silver nanoparticles were synthesized through a seed mediated method as reported previously.[1] Silver nitrate ($AgNO_3$, 99.8%), trisodium citrate (99.0%), sodium borohydride ($NaBH_4$, 98.0%), and tannic acid ($C_{76}H_{52}O_{46}$, 98.0%) were used as the raw materials. The seed silver nanoparticles were prepared as follows. Silver nitrate and trisodium citrate were added into 20 ml of deionized water to make the final concentrations of 0.25 mM silver nitrate and 0.25 mM trisodium citrate. Then, 0.6 ml

of 10 mM sodium borohydride was added into the above solution all at once while stirring vigorously. The seed was used 2 h after preparation. Subsequently, the growth solution was prepared by mixing 10 ml of 5 mM silver nitrate aqueous solution, 10 ml of 1 mM tannin aqueous solution and 10 ml of as-prepared seed solution. The mixture was gently shaken for several minutes to make it homogeneous. Tannic acid acts as the roles of both reducing agent and stabilizer. After the resultant solution was aged for 12 h, silver nanoparticles were collected by centrifugation. The size distribution and shape for silver nanoparticles were checked by a field-emission scanning electron microscope (FE-SEM, JSM-6700F, JEOL Ltd.). Optical absorption spectra were measured with a JASCO-V570 ultraviolet-vis-near infrared spectrophotometer.

Fig. 3.1 (a) shows the FE-SEM image of silver nanoparticles. One can see that silver nanoparticles are anisotropic in particle shape with an average size of 50 nm in diameter without large clusters. Almost all of the particles exhibit anisotropic polymorphs, which is consistent with the reported results.[1] Fig. 3.1 (b) is the TEM image showing that some superfine silver nanoparticles with sizes of 3-5 nm exist. The smaller particles may arise from seed particles without participating particle growth into larger ones. In the synthetic process, the ratio of tannic acid to the seed solution is one of the important factors to determine the resultant particle shape and size. In general, the larger the amount of tannic acid is, the smaller the particle size is. When the concentration of tannic acid is moderate, most particles exist as polymorphs with sharp edges. In contrast, at low concentration of tannic acid, silver nanowires can be observed (not shown), accompanied by a different profile in optical absorption spectrum.

Fig. 3.2 (a) presents the X-ray diffraction pattern of silver nanoparticles. The four diffraction peaks can be assigned to the diffraction of (111), (200), (220), and (311) planes of FCC silver, respectively. The lattice parameter is calculated to be 4.07772 Å by the formula $2d\sin\theta=\lambda(h^2+k^2+l^2)^{1/2}$, where the values of *h, k, l* and θ are taken from

(111) diffraction. The calculation result agrees with that in previous literature.[1] The ratio of the intensity between (111) and (200) diffraction peaks is about 8:1, which is much larger than the conventional value 13:4. This implies that silver nanoparticles are abundant in (111) surfaces and tend to lay with these planes parallel to the supporting substrate. Thus, the diffraction intensity of the (111) plane is greatly enhanced compared with other planes. Fig. 3.2 (b) shows the optical absorption spectrum of silver nanoparticles dispersed in aqueous solution. Two main absorption bands are observed at around 425 and 540 nm, along with a shoulder at 340 nm. It is known that small silver nanospheres possess a single absorption band around 400 nm, while some absorption bands may arise from large particles and anisotropic particle shape.[2] The complex shape of silver nanoparticles as observed in Fig. 3.1 (a) may account for the observations of multiple absorption bands.

The scattering strength of PMMA films embedded with silver nanoparticles is estimated using the Mie theory.[3] The scattering mean free path l_s is expressed as

$$l_s = 1/\rho\sigma_s \tag{3.1}$$

where ρ and σ_s are the number density and scattering cross section of silver nanoparticles, respectively. In this work, the volume fraction of silver nanoparticles is 3×10^{-3} vol% relative to PMMA host corresponding to $\rho\approx4.6\times10^{11}/cm^3$. The scattering cross section of an individual silver nanoparticle of 50 nm in diameter is calculated by the Mie theory to be 5.6×10^{-16} m^2 at the emission wavelength λ_{em}=580 nm. In the above calculation, the author supposes the silver nanoparticles are monodisperse spheres and take the refractive index of PMMA to be 1.5. The scattering mean free path is determined to be 3.9 mm. The product of the wave vector and the scattering mean free path is $kl_s\sim4.6\times10^3>>1$, where k wavevector in PMMA. This result indicates that PMMA-Ag-R6G films operate in extremely weak scattering regime.

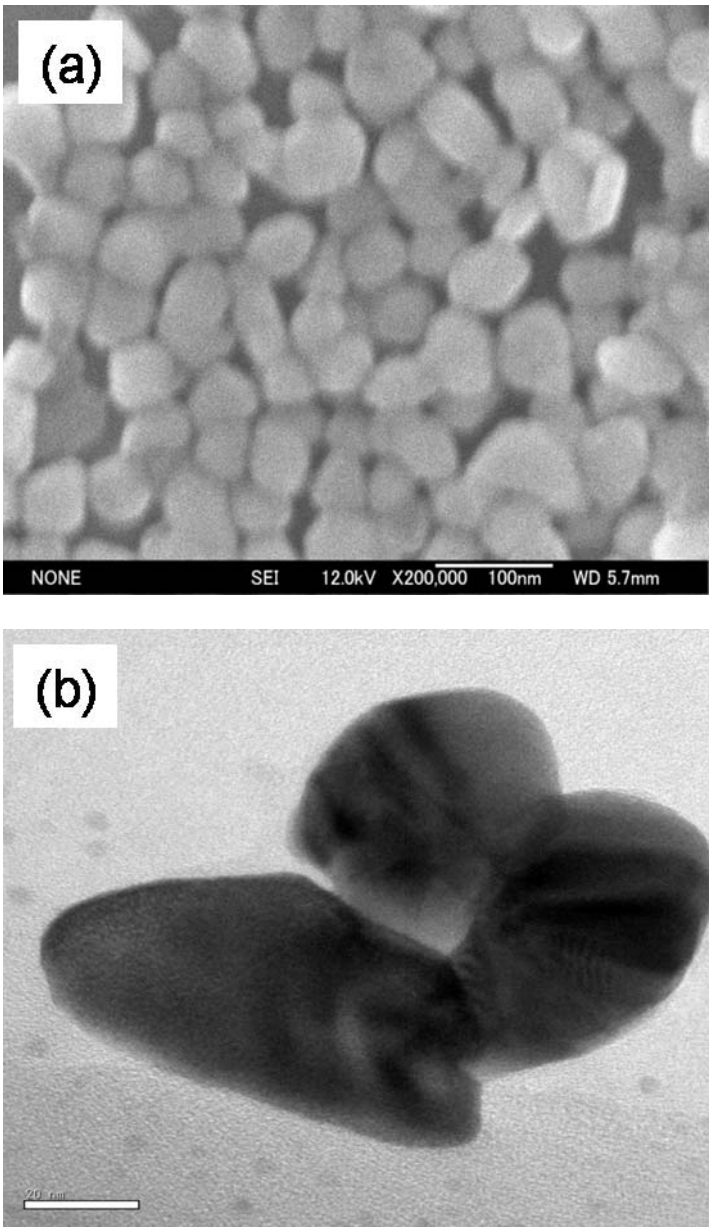

Fig. 3.1: (a) FE-SEM image of silver nanoparticles. (b) TEM image of the same material. The scale bar in (a) is 100 nm and 50 nm in (b). Silver nanoparticles are highly monodisperse without observing large clusters. The smaller particles of 3-5 nm in TEM image are seed particles without participating in growth into larger particles.

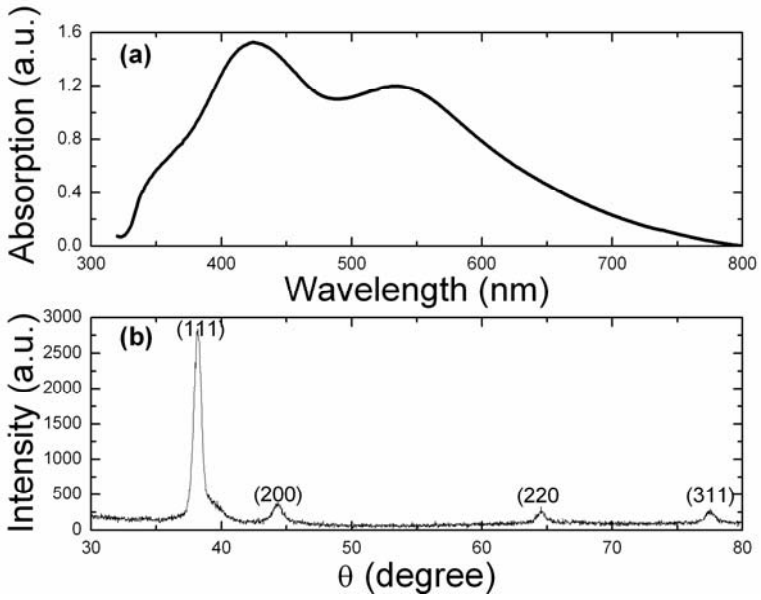

Fig. 3.2: (a) Absorption spectrum and (b) XRD pattern of silver nanoparticles.

3.2 Silver nanoprisms

Silver prism is chosen as another candidate to induce coherent feedback random lasers because the electric field at sharp corners of prisms is much more intense than that of spherical nanoparticles. The electric field has been enhanced by more than 500 times in previous reports.[4] Silver nitrate (99.8%), poly(vinyl pyrrolidone) (PVP, Mw~29,000) were used as the raw materials. Silver nanoprisms were synthesized through a procedure reported previously.[5] PVP has the double role of stabilizer and reducing agent. In a classical synthetic process, 1.88 g PVP was dissolved in 8 ml deionized water, and heated at 60 ℃ under vigorous stirring to dissolve PVP completely. Then, silver nitrate aqueous solution (95.6 mg $AgNO_3$ in 3 ml H_2O) was rapidly added to the solution of PVP. The mixture was heated at 60 ℃ for 5 hours. After that, the solution was centrifuged and washed with ethanol several times to remove PVP. The distribution of size and morphology for silver nanoparticles were checked by FE-SEM. Optical absorption spectra were recorded with a JASCO-V570 ultraviolet-vis-near infrared spectrophotometer.

The samples used in this section are PMMA-R6G films embedded with silver prisms. The film thickness is about 100 μm. The concentration of R6G relative to PMMA host is 10 mM. The density of silver prisms relative to PMMA host is adjusted in the range of $\rho_{Ag}=1.2\times10^{-4}$~$6.0\times10^{-2}$ vol%.

The evolution of SPR signals as a function of ρ_{Ag} in PMMA host is illustrated in Fig. 3.3. The sample embedded with $\rho_{Ag}=1.2\times10^{-4}$ (black) shows a rather flat band in the whole visible wavelength region, while that embedded with $\rho_{Ag}=1.2\times10^{-3}$ (red) begins to exhibit a weak SPR signal at around λ=660 nm. Further increase in the number density of silver nanoprisms leads to the emergence of two more SPR signals at λ=351 and 453 nm, as shown in the absorption spectrum of the sample embedded with silver nanoprisms of $\rho_{Ag}=1.2\times10^{-2}$ (blue). The influence of host materials on SPR signals is apparent, especially for the signals at longer wavelength. For instance, the spectral position of the signal at λ=351 nm is maintained in PMMA host as compared with that in aqueous solution (dark yellow), while the signals at 453 and 660 nm are redshifted by 25 and 100 nm, respectively. As reported previously,[2,3] spherical silver nanoparticles merely show a single SPR band at around λ=400 nm. The observation of complex SPR signals should arise from the influences of size, shape, and dielectric environment, which have been conducted in detail previously.[4] Fig. 3.4 represents the FE-SEM image of silver particles. Silver particles consist of a large amount of prisms of 250 nm in edge length and a small amount of irregular particles of 120 nm in diameter. Most of silver prisms have sharp edges, while some edges are truncated.

In accordance with previous reports,[5] silver nanoparticles exist as smaller particles in the initial synthesis state, and then gradually grow into prisms as the reaction goes. Hence, one can say that irregular particles of 120 nm in diameter are under an incubative stage toward prisms. In an extensive work, the ratio of silver prisms can reach up to 75%, and the SPR signals exhibit redshift with reaction time. However, in this study, the reaction is stopped at a certain time to control the profile of SPR signals

so that the obtained silver nanoprisms can enhance the interplay between silver nanoparticles and dye molecules as much as possible.

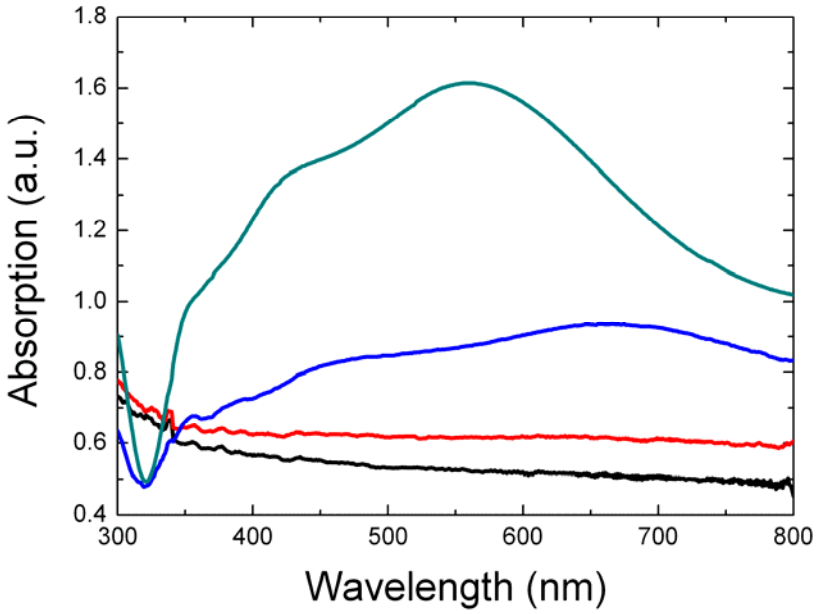

Fig. 3.3: Absorption spectra of PMMA-Ag film with $\rho_{Ag}=1.2\times10^{-4}$ (black), $\rho_{Ag}=1.2\times10^{-3}$ (blue) and $\rho_{Ag}=1.2\times10^{-2}$ vol% (dark yellow) along with silver nanoprisms in aqueous solution (dark cyan). The first two absorption spectra are magnified by 10 times in order to clearly compare all the absorption spectra.

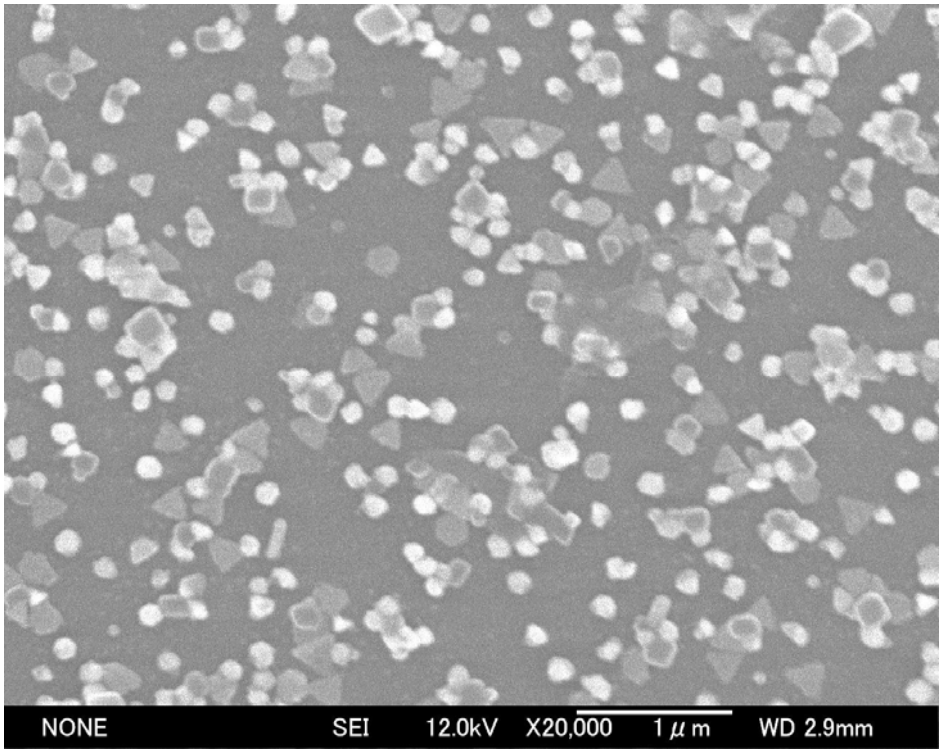

Fig. 3.4: FE-SEM image of silver nanoprisms. The particles consist of ~50% prisms with 250 nm in edge length and ~50% irregular smaller particles with average size of 120 nm in diameter.

3.3 PMMA films embedded with silver nanoparticles

Poly(methyl methacrylate) (PMMA, Mw~120,000) is used as a matrix material for silver nanoparticles in this work. PMMA films embedded with silver particles are prepared through a cell-casting technique. First, PMMA and R6G were dissolved in chloroform solvent. Then, silver nanoparticles are dispersed into the solution and ultrasonically mixed completely. After that, the as-prepared mixture was evaporated at room temperature under air flow. The advantage of this method is that the concentrations of silver nanoparticles and dye can be controlled separately. The film thickness is controlled by the content of PMMA, which can be tuned from several microns to several millimeters. In this work, the concentration of silver nanoparticles relative to PMMA host is extremely low in order to operate the system in weak scattering regime.

3.4 *In situ* synthesized PVA-Ag-R6G films

Experimentally, it is very hard to prepare a large amount of superfine silver nanoparticles toward potential applications in random lasers. In this work, the author adopts an *in situ* route to prepare polyvinyl alcohol (PVA) films embedded with superfine silver nanoparticles.[6] The raw materials used in this experiment are silver nitrate (99.8%), PVA (%hydrolysis=86.5-89, M_w=22000). In a typical synthetic process, the mixture of PVA, silver nitrate and R6G aqueous solutions was spin coated on glass substrate accompanied by thermal treatment at 90-130 ℃ to precipitate silver nanoparticles. The evolution of silver nanoparticles in PVA matrix versus annealing time was characterized by optical absorption spectra recorded with a JASCO-V570 ultraviolet-vis-near infrared spectrophotometer.

Fig. 3.5 (a) shows the evolution of optical absorption spectra of PVA-Ag-R6G films as a function of annealing time when the films are annealed at 110 ℃. An

absorption band around λ=420 nm begins to emerge when the annealing time reached 30 min and then rises gradually with the increase in annealing time and finally saturates after 420 min annealing. This band should be ascribed to SPR signal of spherical silver nanocrystals. During the thermal treatment, the alcohol group of PVA reduces Ag^+ ions, while the alcohol itself is oxidized to ketones. The absorption band at around λ=532 nm is due to the electronic transition from the ground state S_0 to the first excited singlet state S_1 of R6G. Fig. 3.5 (b) shows the difference absorption spectra between annealed samples and as-prepared one, together with the simulation curves by using the Mie scattering theory and Drude model. The evolution of SPR signal is very obvious with the increase in the annealing time.

Based on the Mie theory,[7] the extinction coefficient of media embedded with metal nanoparticles can be expressed by

$$\alpha(\omega) = \frac{9q\varepsilon^{3/2}\omega}{c} \frac{\varepsilon_i(\omega)}{[\varepsilon_r(\omega)+2\varepsilon]^2+\varepsilon_i(\omega)^2}, \tag{3.2}$$

where ε and q are the permittivity of host material and the volume fraction of metallic particles relative to host materials, respectively, while ε_r and ε_i are the real and imaginary parts of permittivity of metal nanoparticles, respectively. According to Drude's free electron theory,[8] the permittivity of metal nanoparticles is expressed by

$$\varepsilon_m(\omega) = 1 + i\frac{\omega_p^2\tau}{\omega(1-i\omega\tau)}, \tag{3.3}$$

where τ is the relaxation time, and $\omega_p=(N_e e^2/\varepsilon_0 m)^{1/2}$ is the frequency of plasma oscillation (N_e, e, and m are the number, charge, and mass of electrons, respectively). Doyle and Kreibig et al. proposed that,[9,10] for a spherical particle much smaller than the mean free path of the electrons in bulk material, l_∞, the collisions of the conduction electrons with the particle surfaces become important as an additional relaxation process and the effective mean free path, l, is restricted by the particle size, $2R$. Thus, the

relaxation time τ can be substituted for the collision time

$$\tau_c = 2R / v_f , \tag{3.4}$$

where v_f=1.39×10^8 cm/s is the Fermi velocity. Eventually, one can get from Eqs. (3.2) and (3.3), when $\omega\tau_c$>>1,

$$\alpha(\omega) = \frac{9qn^3}{c(1+n^2)} \frac{\omega^2\omega_r^2 / \tau_c}{(\omega^2 - \omega_r^2)^2 + (\omega_r^2 / \omega\tau_c)^2} , \tag{3.5}$$

where ω_r is the resonance frequency of the surface plasmon and described by

$$\omega_r^2 = \omega_p^2 /(1+2n^2) . \tag{3.6}$$

Under this approximation, the full width at half maximum is given by $\Delta\omega_{1/2}\approx 1/\tau_c$, thus one can obtain the following relationship

$$2R = v_f / \Delta\omega_{1/2} . \tag{3.7}$$

The simulation curves by the Mie-Drude model Eq. (3.4) are presented in Fig. 3.5 (b). The simulation result indicates that the average size of Ag nanoparticles is ~1.0 nm in radius, while the volume fraction of silver nanoparticles relative to PVA is ~3.8×10^{-4}. It should be noted that no change has been found in the sample during 532 nm laser irradiation in laser experiment, which indicates that the pump laser has no influence on the evolution of silver nanoparticles in PVA matrix.

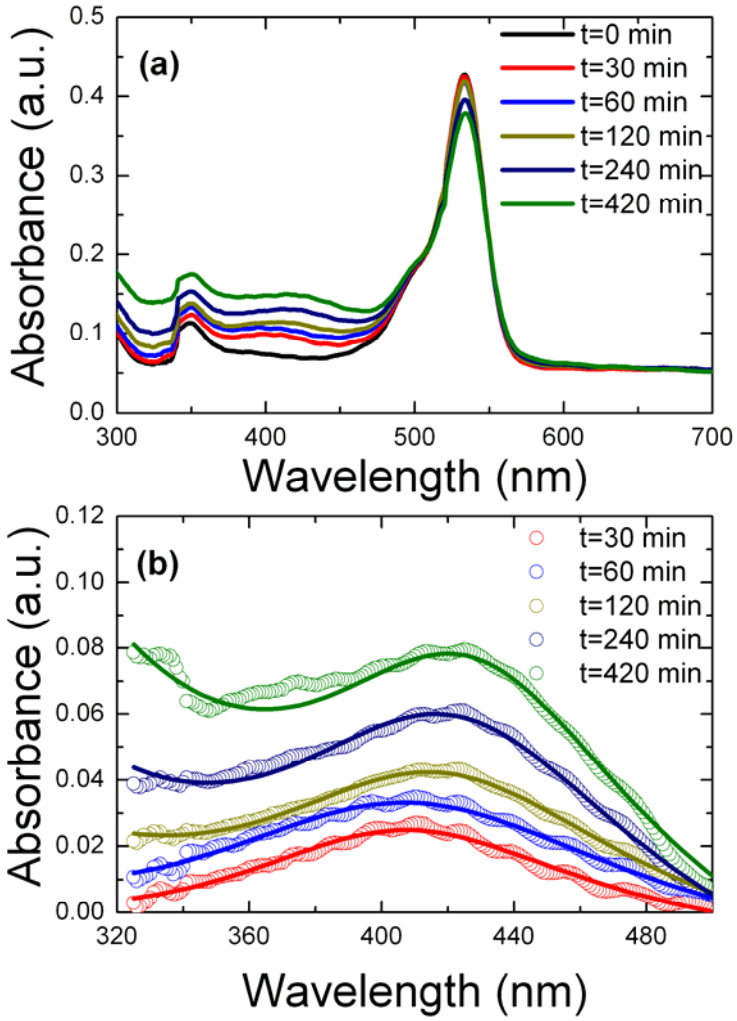

Fig. 3.5: (a) Optical absorption spectra of PVA-Ag-R6G film as a function of annealing time: t=0 (black), 30 (red), 60 (green), 120 (blue), 240 (yellow), and 420 min (cyan). (b) The difference spectra (circles) between annealed samples and as-prepared one along with the simulation curves (solid lines) by the Mie scattering theory and Drude model. The sample was annealed at 110 ℃ in air.

References

1. X. Tian, W. Wang, and G. Cao, *Mater. Lett*. **61**, 130 (2007).
2. R. C. Jin, Y. W. Cao. C. A. Mirkin, K. L. Kelly, G. C. Schatz, and J. G. Zheng, *Science* **294**, 1901 (2001).
3. G. Mie, *Ann. Phys*. **25**, 377 (1908).
4. K. L. Kelly, E. Coronado, L. L. Zhao, and G. C. Schatz, *J. Phys. Chem. B* **107**, 668 (2003).
5. I. Washio, Y. J. Xiong, Y. D. Yin, and Y. N. Xia, *Adv. Mater*. **18**, 1745 (2006).
6. S. Porel, S. Singh, S. S. Harsha, D. N. Rao, and T. P. Radhakrishnan, *Chem. Mater*. **17**, 9 (2005).
7. M. Born and E. Wolf, *Principles of optics* (6th ed.), Pergamon, Oxford, 1980.
8. C. Kittel, *Introduction to solid state physics* (7th ed.), Wiley, New York, 1996.
9. W. T. Doyle, *Phys. Rev*. **111**, 1067 (1958).
10. U. Kreibig and C. V. Fragstein, *Z. Phys*. **224**, 307 (1969).

Chapter 4 Random Lasers Induced by Metal Nanostructures

As described in chapter 3, silver nanoparticles are chosen as scattering centers in random lasing materials. Polymer films are used as host materials, while R6G is used as the light emitting material. Silver nanoparticles take three major advantages over dielectric nanoparticles when they are used as scattering centers in random lasers.

(1) Silver nanoparticles have much larger scattering cross section than dielectric nanoparticles when they have the same dimensions.

(2) Silver nanoparticles possess unique SPR property. Light can be spatially confined near the surface of metal nanoparticles; therefore, high optical gain for lasing is expected. Highly localized optical modes can be formed during interactions between dye molecules and silver nanoparticles through SPR.

(3) The scattering spectrum of silver nanoparticles has a maximum that is sensitive to particle size and shape. This maximum exists at certain wavelength for each silver nanoparticle; thus, the scattering maximum can be selected by tuning SPR profile.

4.1 Experimental setup

The samples were optically pumped by the second harmonics of a mode-locked Nd:YAG laser (λ=1064 nm, 10 Hz repetition rate, 25 ps pulse duration) in order to conduct random laser experiments. The laser beam was focused on the samples through a cylindrical lens to form a stripe with a width of 17 μm and a length that could be varied from 0.1 to 6 mm. Fig. 4.1 shows the experimental setup for random lasers. A tunable attenuator was used to adjust the pulse energy and the aperture was to control the beam spot size. The sample was mounted on a stage that could be adjusted three

dimensionally. The emission was collected along the stripe with a fiber device into a monochromator (SPEX 270M) coupled to a liquid-nitrogen-cooled charge couple device (CCD 3000, the spectral resolution is 0.07 nm). In order to study the effect of the gain length on laser behaviors, the stripe length is changed from 0.1 to 6 mm. Single-shot emission spectra were obtained by simultaneously controlling the integration time of CCD and temporal interval between pulses.

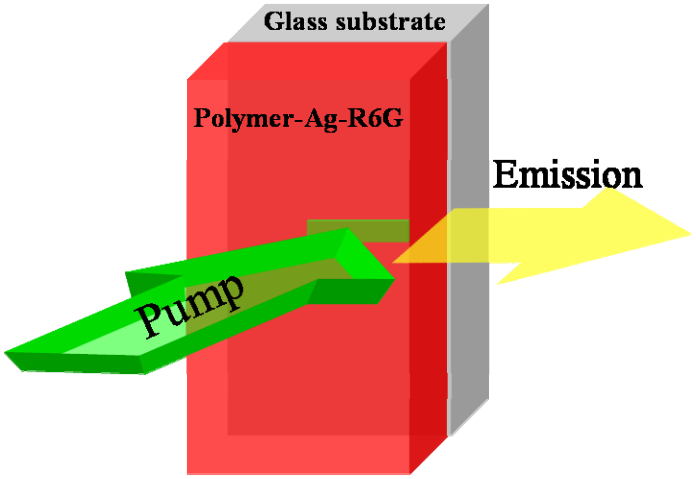

Fig. 4.1: Schematic illustration of excitation-detection configuration for measurements of random lasers. A mode-locked Nd:YAG laser (λ=1064 nm, 10 Hz repetition rate, 25 ps pulse duration) is used as the excitation source. A cylindrical lens is used to focus the incident beam to form a stripe on sample. The emission is collected with a fiber device into a monochromator coupled to a liquid nitrogen cooled charge couple device.

4.2 Rodamine 6G (R6G)

Organic dye is one of the most important laser materials; it is usually a molecule in which carbon-carbon double bonds, in particular, conjugated double bonds are formed. In this work, rodamine 6G (R6G) is used as a light emitting molecule for random lasers. Its structure and electronic energy levels are presented in Fig. 4.2. The ground state is a singlet and denoted by the term S_0. Under light irradiation, an electron is excited into the states that are denoted by S_1, S_2, T_1 and T_2, where S_1 and S_2 are singlet states, while T_1 and T_2 are triplet states. Either the singlet state or the triplet state contains a series of vibrational and rotational energy levels. The excitation with maximum efficiency occurs at ~530 nm, hence the second harmonic wave of Nd:YAG laser is usually used as an excitation source for R6G. The excited electron nonradiatively relaxes to the lowest vibrational level of S_1 in a time scale of ~1 ps. This nonradiative relaxation process is called the internal conversion. Then, the electron undergoes radiative relaxation to one vibrational level of S_0 or nonradiatively relaxes to one vibrational level of T_1. The former transition is spin-allowed and the fluorescence lifetime is ~1 ns, while the latter is spin-forbidden so that the process is rather slow compared with the former but occurs within ~10 ns. The spin-forbidden process is called the intersystem crossing. The radiative relaxation process from T_1 to S_0 is called the phosphorescence with a characteristic lifetime of ~100 μs. If an electron reaches T_1, the excitation to the higher triplet levels is an efficient process. The pump process involves the following steps: (1) the excitation to one vibrational level of S_1, (2) the internal conversion to the lowest vibrational level of S_1 in a time scale of ~1 ps, and (3) radiative relaxation to one vibrational level of S_0 that is well above the ground state.

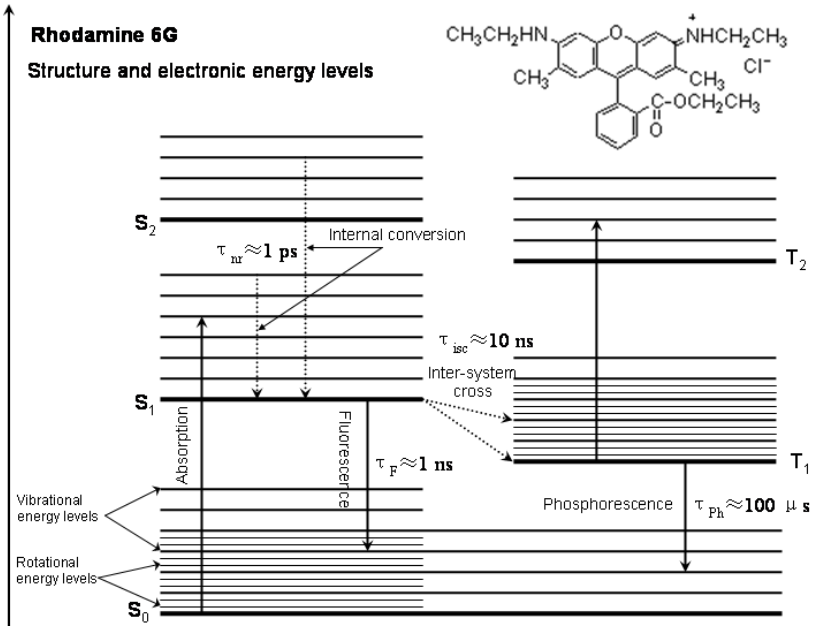

Fig. 4.2: Molecular structure, schematic energy levels, and electronic transitions of R6G. S_0, S_1 and S_2 denote the singlet levels while T_1 and T_2 the triplet levels. The internal conversion occurs in a time scale of $\tau_{nr}\approx 1$ ps. The intersystem crossing process takes a time $\tau_{isc}\approx 10$ ns, much slower than the fluorescence process $\tau_F\approx 1$ ns. The phosphorescence process from T_1 to S_0 occurs in a time scale of $\tau_{Ph}\approx 100$ μs.

4.3 Properties of random lasers

4.3.1 PMMA films embedded with anisotropic silver nanoparticles

In this section, PMMA-R6G films embedded with anisotropic silver nanoparticles have been examined on random lasing properties. The thickness of PMMA-Ag-R6G films was ~30 μm. The volume fraction of silver nanoparticles relative to PMMA host was varied from 3×10^{-5}-3×10^{-2} vol%. The concentration of R6G relative to PMMA host is 10 mM for all the samples. Unless otherwise noted, the results below are mainly described for the sample containing 3×10^{-3} vol% silver nanoparticles.

Fig. 4.3 (a) shows the evolution of emission spectra against the pump energy. When the pump energy is low, the emission spectrum exhibits a broad band centering at λ=590 nm with FWHM of ~46 nm, which can be ascribed to the transition from the first excited level S_1 to the ground state S_0 of R6G. As the pump energy is increased up to 0.89 μJ, a single sharp peak at λ=572 nm with FWHM less than 0.2 nm suddenly emerges, implying the occurrence of lasing. In contrast, the sample containing no silver nanoparticles merely manifests a spontaneous emission band with FWHM of ~46 nm under identical excitation conditions. Discrete laser spikes are observed as the pump energy increases further. Lasing frequencies vary with the irradiated position on the sample, which is associated with the random distribution of silver nanoparticles in PMMA host. Given that FWHM of these lasing modes is much less than 1 nm, the lasing behavior is of coherent feedback. Fig. 4.3 (b) plots the emission intensity as a function of the pump energy. The emission intensity increases more rapidly above a threshold, further indicating the occurrence of laser oscillation. The threshold to reach laser oscillation is 0.89 μJ.

Two points should be addressed. One is the spectral shift in the emission spectra as the pump energy increases. The emission spectrum peaking at λ=590 nm below the threshold pump energy shifts to a shorter wavelength at a pump energy just above the

threshold (E_p=0.89 μJ) and then again to a longer wavelength at a pump energy much higher than the threshold (E_p=2.13 μJ). This phenomenon has been observed in the previous literature.[1] The blue shift with the pump energy is interpreted as the reabsorption effect. Because there is a partial overlap between the red side of the absorption and the blue side of the emission of R6G, the emission at the blue side will be reabsorbed by other dye molecules when the pump energy is low so that the emission peaks at a longer wavelength region. As the pump energy increases, the population at the excited state grows rapidly so that the reabsorption of the emission light decreases; hence the emission spectrum peaks at shorter wavelength. As the pump energy further increases, the excited state absorption (the maximum wavelength of the excited state absorption is ~565 nm) is so significant that the emission at the blue side is reabsorbed; hence the emission peaks show a red shift again. Another point addressed is the linewidth evolution with the pump energy. The emission at E_p=0.58 μJ shows a broad spontaneous emission band. As the pump energy just reaches the threshold at E_p=0.89 μJ, the sharp peak is so intense that the broad spontaneous band is strongly suppressed. Nevertheless, the emission at E_p=2.13 μJ exhibits sharp peaks together with an obvious ASE band. The ASE band is mainly due to the excited state absorption that results in a considerable portion of dye molecules without participating in the lasing process.

When the spontaneous process is solely involved in the emission, the slope in the plot of the emission intensity versus the pump energy is linear, as demonstrated in Fig. 4.3 (b). As the ASE process appears, the emission intensity may increase either linearly or nonlinearly. Both of the cases have been reported previously.[1,2] Once the real lasing action occurs, the slope dramatically increases. The gradual transition from the spontaneous emission to ASE and finally lasers has been observed in dye solutions suspended with ZnO and TiO_2 particles.[1,2] However, this phenomenon has not been observed in this work.

The central emission frequency is determined by the gain medium for incoherent random lasers while it is determined by the eigenmodes of resonators for coherent

random lasers. In the present random media, the gain medium and scattering centers are separate. The emission can escape the naked polymer film through the totally open boundary. This is quite different from the chaotic cavity lasers, in which only limited open boundaries are available so that light is spatially confined in the almost closed cavity. The author accounts for the modes observed herein based on the concept of quasistates (also called quasimodes) for light in random media which was proposed by Cao and co-workers.[3] The quasistates are the eigenmodes of the Maxwell's equations in a finite-sized passive random medium. The boundary conditions for quasistates are the absence of any incoming waves and the presence of only outgoing waves. Hence, the frequency of a quasistate is expressed by a function of complex variable: $\Omega=\omega+i\gamma$, where γ is the decay rate of a quasistate as a result of its coupling to the environment. When the light reaches the boundary, it will either be reflected back to or escape the random medium. The mean decay rate is given by $\gamma_m \sim D/L^2$, where D is the diffusion coefficient and L the dimension of the random medium. The average frequency spacing between adjacent quasistates is $\delta\nu=v\lambda^2/8\pi L^3$, where v and λ are the speed of light and the wavelength in the medium, respectively. When the pump energy is low, the decay rate of quasistates is slow. Therefore, γ_m is larger than $\delta\nu$ so that the frequencies of quasistates overlap each other, which gives rise to a continuous broad emission band. In contrast, as the pump energy is increased to some extent, the coupling between adjacent quasistates is so strong that γ_m is less than δ_ν. When the pump energy reaches the threshold of an individual quasistate, the quasistate will lase. With the further increase in the pump energy, more quasistates obtain sufficient gain to lase so that more sharp peaks appear.

It should be mentioned that two reports have been published on random lasers enhanced by silver and gold nanoparticles but the lasers therein are restrained to be of incoherent feedback.[4,5] Random media in Dice's work are dye solutions suspended with silver nanoparticles with narrower size distribution and more uniform shape. The linewidth of the emission band was remarkably reduced to 4.6 nm, and the threshold

was reduced by the incorporation of silver nanoparticles. Random media used in Popov's work were polymer films embedded with gold nanoparticles. Popov took into account the effect of the spectral profile of the SPR signal on random lasing behaviors by adjusting the particle size and found that the threshold was the lowest when the SPR peak was close to the emission maximum. The linewith of the emission spectrum could be reduced to 4-7 nm. In both of the-above mentioned reports, the observed emission is in analogy to ASE, and sharp peaks with linewidths less than 1 nm are not observed.

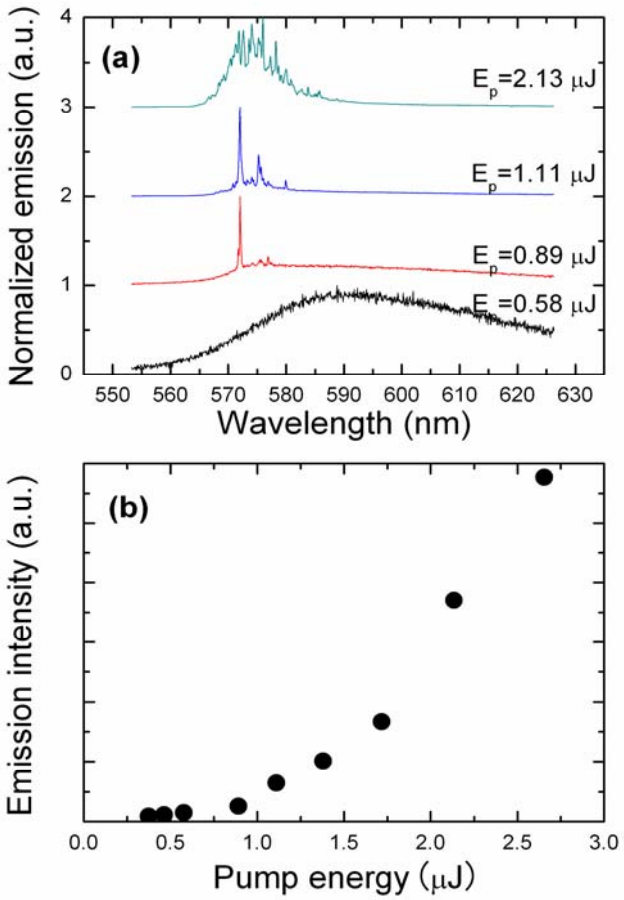

Fig. 4.3: (a) Emission spectra recorded below and above the threshold pump energy; E_p=0.58, 0.89, 1.11 and 2.13 μJ, respectively. The stripe length and width are 2.4 mm and 17 μm. (b) Integrated emission intensity versus the pump energy. The threshold pump energy is about 0.89 μJ.

Fig. 4.4 (a) depicts the evolution of emission spectra as a function of the stripe length when the sample is pumped at 3.30 μJ of pump energy. The number of lasing modes rapidly increases from ~4 at l=0.6 mm to ~40 at l=2.4 mm. The results are naturally expected since the increase in l gives rise to more cavities for which the optical gain exceeds the loss and then leads to more lasing modes. The broad emission background is strongly inhibited at l=0.6 mm but revivals with increasing l. Fig. 4.4 (b) plots the dependence of the pump energy at threshold E_{th} on l, showing that E_{th} tends to decline with increasing l. The fitted curve abides by $E_{th}=E_0 l^{\alpha}$, where E_0=1.9±0.18 and α=−1.3±0.16, as shown in Fig. 4.4 (b). The value of α nearly coincides with[3]

$$E_{th} \propto \frac{\sqrt{l_t}\, l^{-3/2}}{\sqrt{l_a}}, \tag{4.1}$$

where l_t is the transport mean free path and l_a is the pump absorption length. The value of E_0 is rather large because of the large value in l_t, while the ratio of $\sqrt{l_t}/\sqrt{l_a}$ is consistent with the value in previous report.[3]

The resift in the emission spectra is observed with increasing the stripe length, which can be interpreted by the reabsorption effect. In case of the stripe pump configuration, the emitted light will experience various propagation distance from the edge of the stripe. As the propagation distance increases, the magnitude of the output intensity declines due to reabsorption or scattering. The further the pump region from the stripe edge is, the larger the effective path length is, which results in an increased reabsorption of the emission and thereby the shift of the emission peak toward the red side. It is also observed that the suppressed ASE band at shorter stripe length revivals at longer stripe length. In case of stripe pump configuration, the pump intensity is uniform throughout the entire pump area. This phenomenon can also be ascribed to the increased reabsorption effect. This behavior is different from what have been observed in random lasers from ZnO powders, which may be caused by the negligible reabsorption in case of ZnO powders.

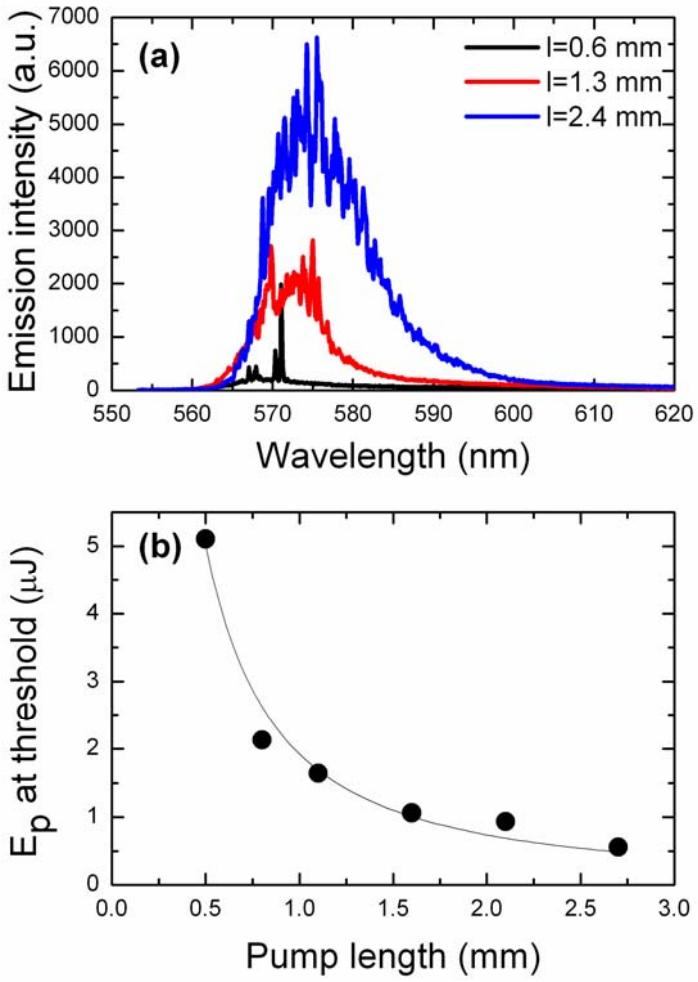

Fig. 4.4: a) Evolution of emission spectra with the pump length; l=0.6 mm (black), l=1.3 mm (red), and l=2.4 mm (blue). The pump energy is 3.30 μJ. b) Dependence of lasing threshold on the stripe length. The solid line represents a fit of $E_{th}=E_0 l^{\alpha}$ *to the experimental data, where* $E_0=1.9\pm0.18$ *and* $\alpha=-1.3\pm0.16$.

The emission is not confined externally; however, lasing output is found to be highly directional along the stripe. When the pump energy is low, a bright light spot was observed on the screen normal to the stripe, while the increase in the pump energy causes development into multiple sporadic spots. Fig. 4.5 (b) plots the emission intensity dependence on probe angles, which indicates that the emission is strongly confined in an angle range of ~20º. Out of this angle range, what has been detected is not laser signal but spontaneous emission or ASE. For instance, the emission spectra

collected along the stripe and 45° away are presented in Fig. 4.5 (a). The absorption lengths at λ=532 and 570 nm are calculated through transmission measurements to be ~6 and ~81 μm, respectively. Either the penetration depth at λ=532 nm (<30 μm) or the stripe width is much less than l_s; hence it is hard to obtain high gain for lasing along these two dimensions via multiple scattering of light. In contrast, l can be tuned close to or larger than l_s so that optical gain along the stripe length is much larger than the other dimensions and result in highly directional lasing.

The output direction of random lasers depends on the gain in each dimension and light confinement. The pump area can be circular spot or stripe, which depends on the use of circular focus lens or cylindrical lens. In case of circularly pumped ZnO films, the gain distribution is isotropic so that lasers emit towards all directions. However, it is not this case for circularly pumped dye solution suspended with dielectric particles. For instance, Wu et al.[6] reported that the laser output was tightly confined within a small angle range backward. The main reason lies in the formation of the excitation cone inside the solution for a moderate scattering system. The light confined within this cone can obtain much higher gain so that the laser output is strongly confined in the backward direction. The role of the cone resembles the Fabry-Perot cavity for laser oscillation. When the scattering strength becomes very intense, the excitation volume in the solution seems like a hemisphere that may be caused by the isotropically strong scattering. As a consequence, laser emission disappears.

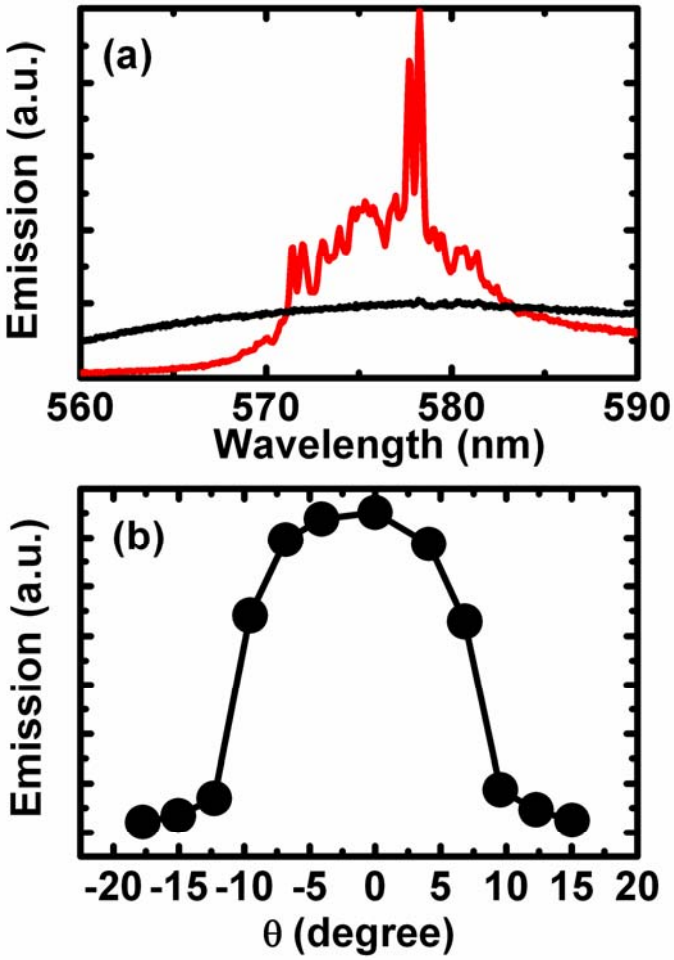

Fig. 4.5: (a) Emission spectra collected along the stripe (red line) and 45° away from the stripe (black line). The pump energy is 1.72 μJ. b) Angular distribution of the emission intensity when the pump energy is 1.72 μJ.

Another notable phenomenon is revealed in Fig. 4.6, representing six of single-shot emission spectra collected at the same pump position on the sample with the same pump energy. Spectral spacing between adjacent lasing modes is irregular, which differs from the behavior observed in a dynamically random medium.[7] Nevertheless, lasing frequencies have not shown strongly chaotic behaviors that have been reported in statically disordered media but statistically tend to populate in dominant locations denoted by S_n (n: 1~6) in Fig. 4.5, implying that random lasers herein are determined by certainly fixed oscillation cavities in PMMA host. The shift in lasing frequencies may

be caused by nonlinear Kerr effect since the third-order nonlinearity ($\chi^{(3)}$) not only changes the frequency and size of lasing modes but also modifies the laser emission intensity and laser pulse width.[8] The illuminated surface area A is 4.1×10^4 μm^2 herein; so this area can support lasing modes counting up to $N>7.8\times10^5$ estimated by $N=2\pi A/\lambda^2$ at λ=570 nm.[7] This large number combined with nonlinear effect leads to strong mode competition so that only the modes with longer lifetime can lase eventually.

Depending on the configuration of scattering centers, random media can be classified into two categories: statically and dynamically scattering media. The former refers to the random media in which the scattering centers are fixed spatially, such as ZnO film, polymer films embedded with dielectric particles, and porous glasses infiltrated with dye solution. The latter refers to the system in which the scattering centers are dynamic and move all the time. The typical example of the latter is dye solution suspended with dielectric particles. The dielectric particles behave like Brownian movement in dye solution. The shot-to-shot emission spectra may differ from each other due to the ceaseless movement of particles in the solution, while the shot-to-shot emission spectra should be reproducible for statically scattering media. However, the emission spectrum in this work is not totally reproducible. The author surmises that this variation may be partially caused by the unstable output of the laser pulse besides the effect of nonlinear process.

When the emission spectrum is averaged over several pulses, the emission spectrum in dynamic systems may become smooth and the sharp peaks are smeared out because the particle in solution moves ceaselessly and then leads to the variation of oscillation cavity. However, the emission spectrum from static random media may maintain the sharp peaks due to the fixation of particles relative to the host. Experimentally, it has been observed that the sharp peaks still maintains even after the emission spectrum is averaged over up to several hundreds of pump pulses.

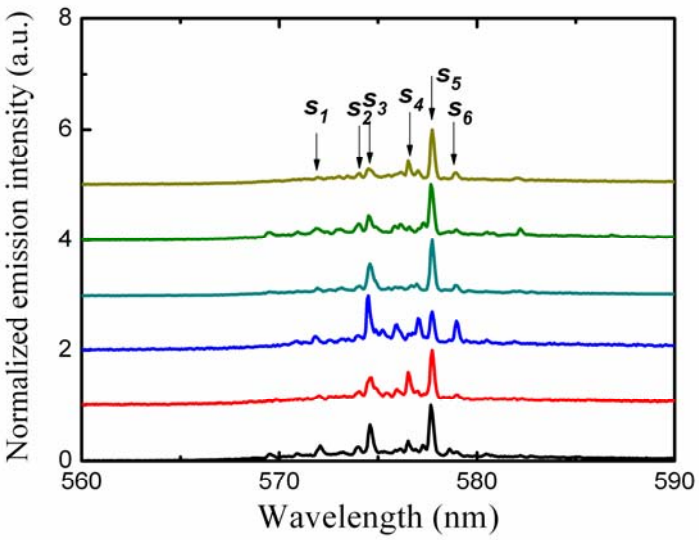

Fig. 4.6: Six of single-shot emission spectra collected at the same position on the sample; the lasing modes trend to populate in frequencies denoted by S_n (n: 1~6). The stripe length under irradiation is 2.4 mm. The pumping pulse energy is about 2.13 μJ.

The oscillation cavity length is of importance for both regular lasers and random lasers. It is measurable for regular lasers while not for random lasers. Polson[2] found that the cavity length could be deduced from the power Fourier transform of single-shot emission spectra. The intensity of the Fourier transform of a Fabry-Perot cavity consists of a series of equally spaced diminishing lines given by[9]

$$I(d) = \left|1 - R\exp(2i\phi)\right|^2 \times \sum_{m=0}^{\infty}\sum_{l=0}^{\infty} \frac{R^{l+m}\exp[-2i\phi(l-m)]}{kL(l+m+1)+i[\pi d + nL(l-m)]} \qquad (4.2)$$

where k is the wavevector, d is the conjugate variable to wavevector, l and m are integers, ϕ is the phase change upon reflection at the mirrors, and R is the mirror reflectivity. The important part of this expression is that peaks are produced whenever the imaginary part of the denominator goes to zero. This occurs when d is a multiple of nL/π with the circular geometry used here, where n is the refractive index of the working medium. In the Fourier transform of emission spectra, x axis is the path

length denoted as L in the above formula. The procedure to determine the oscillation length is as follows. First, the Fourier transform is mathematically transferred from single-shot spectrum. Next, L is calculated by $L=\pi d/mn$, where m denotes the order of the Fourier transform harmonics. In practical, ensemble-averaged power Fourier transform is usually used since the fluctuation in the pump energy and the particle fluctuation inevitably give rise to different single-shot emission spectra. Suppose the individual single-shot spectrum is given by $g_n(\lambda)$ that results in the Fourier transform spectrum $f_n(\lambda)$, the ensemble-averaged Power Fourier transform spectrum can be expressed as

$$\overline{f(\lambda)} = \frac{f_1(\lambda) + f_2(\lambda) + f_3(\lambda) + \cdots + f_n(\lambda)}{n} \tag{4.3}$$

The lasing cavity length L should be approximately integral times of l_s in case of laser oscillation resulting from multiple scattering of light. The power Fourier transform spectrum of single-shot emission spectra closely associates L with the Fourier transform components d_m. A well-defined laser cavity exhibits peaks at d_m that abides by $d_m=mLn/\pi$. To unveil the underlying resonators involved in random lasers, the author calculated the ensemble-averaged power Fourier transform spectra from single-shot emission spectra, as shown in Fig. 4.7. All the single-shot emission spectra involved in the calculation are collected at various pump positions on the sample since the configuration of scattering centers is static here. The power Fourier transform spectra from individual single-shot emission spectra exhibit free-standing peaks, while no apparent correlation occurs to each other. In contrast, the correlation increases with the increase in the number of single-shot emission spectra involved in the calculation of ensemble-averaged power Fourier transform spectra. Hence, the ensemble-averaged power Fourier transform spectrum derived from 100 single-shot emission spectra rather than individual power Fourier transform spectra is utilized to determine the oscillation cavity length. The first peak denoted as d_1 in Fig. 4.7 falls at ~6.4 μm that can be

treated as the fundamental component, while the other components denoted as d_2, d_3, d_4, d_5, and d_6 are regarded as the *mth* harmonics (m=2~6). The oscillation cavity length is given by $L=\pi d_1/n$, so we obtain L=13.0 μm by using n=1.54 for PMMA host. The cavity length is ~100 times smaller than l_s, which has rarely occurred so far, indicating that scattering of light plays a minor role in the onset of coherent feedback.

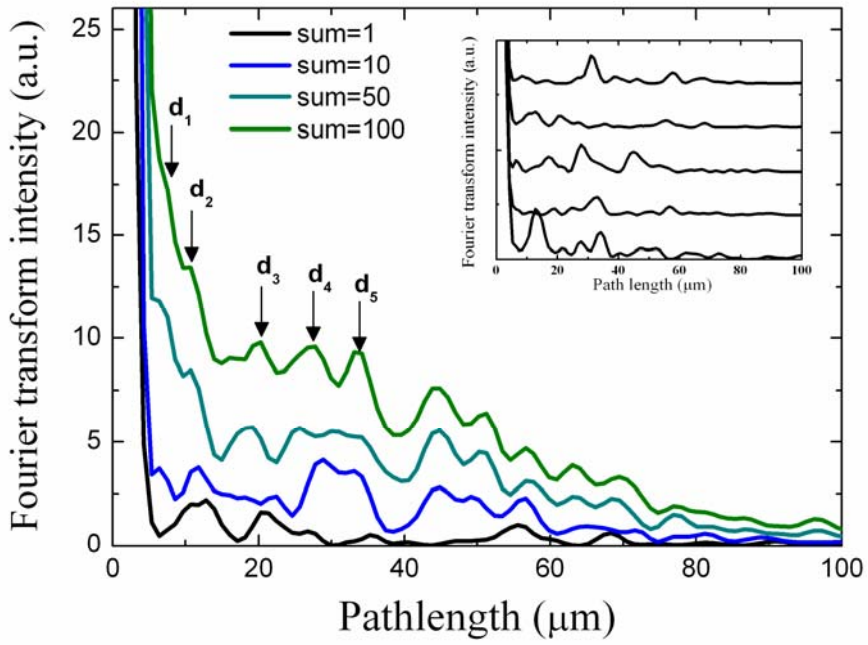

Fig. 4.7: Ensemble-averaged Fourier transform spectra of single-shot emission spectra collected at various spots on the sample. The number of single-shot emission spectra for EAPFT is chosen as 10, 50 and 100, respectively. The stripe length under irradiation is fixed at 2.4 mm. The pumping pulse energy is about 2.13 μJ.

4.3.2 PMMA films embedded with silver nanoprisms

In this section, random lasing properties of PMMA-R6G films embedded with silver nanoprisms have been examined. The sample thickness is bout 100 μm. The concentration of R6G relative to PMMA host is in a range of 1~20 mM. The volume fraction of silver prisms relative to PMMA host is adjusted in a range of $\rho_{Ag}=1.2\times10^{-4}\sim6\times10^{-2}$. Unless otherwise noted, results are mainly described about a sample containing 1.2×10^{-3} vol% silver nanoprisms and 10 mM R6G.

Fig. 4.8 (a) shows the evolution of emission spectra as a function of the pump energy. The emission spectrum exhibits a broad band centering at λ=600 nm with linewidth of ~40 nm, which should be ascribed to the spontaneous emission of R6G from S_0 to S_1. As the pump energy is increased up to 0.67 μJ, a narrowing band emerges in the high energy side at λ=580 nm, which should be assigned to ASE of R6G. Further increase in the pump energy up to 0.83 μJ gives rise to several sharp peaks at around λ=578 nm accompanied by a rapid increase in the emission intensity, indicating the onset of lasing oscillation. In contrast, the sample containing no silver nanoparticles only shows a broad spontaneous emission band when pumped at 0.83 μJ. Therefore, silver nanoparticles are vital to the emergence of sharp laser peaks. As the pump energy is further increased, more laser peaks are observed since more oscillation cavities are formed with the increase in the pump energy. Lasing frequencies are sensitive to the irradiated positions on the sample, which is ascribed to the random distribution of silver nanoprisms inside PMMA host. Fig. 4.8 (b) shows the evolution of integrated emission intensity with the pump energy. The emission intensity increases more rapidly with the increase of the pump energy when the pump energy exceeds a threshold, implying the onset of lasing actions. A clear threshold behavior is observed.

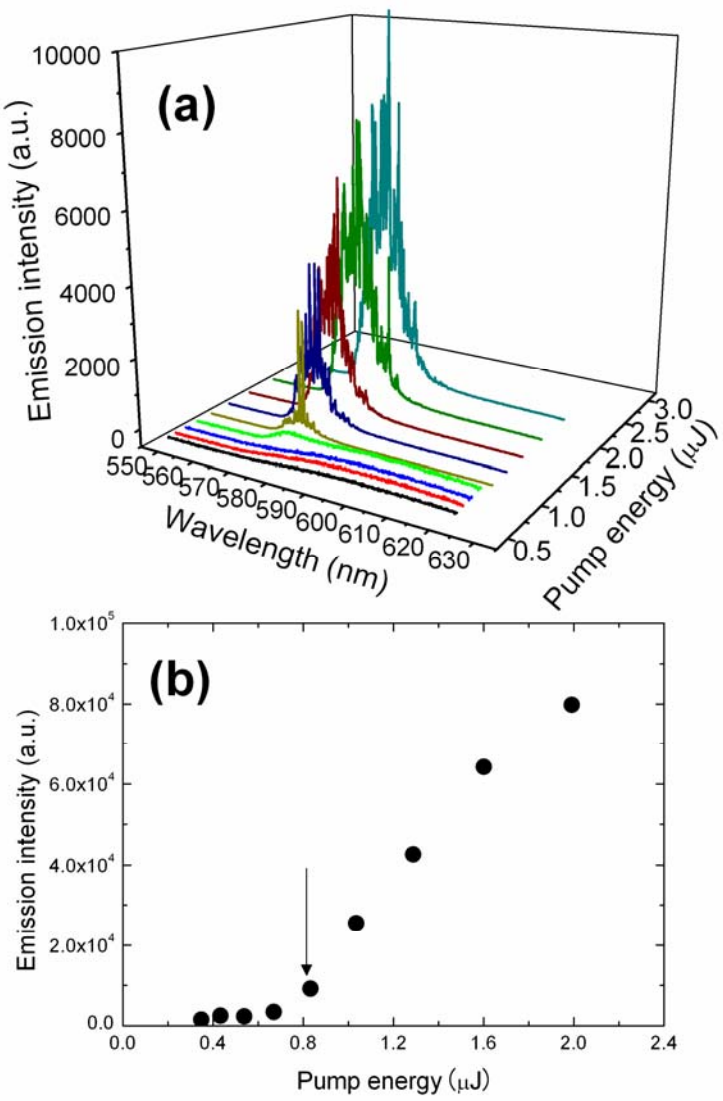

Fig. 4.8: (a) Emission spectra against the pump energy for PMMA film with $\rho_{Ag}=1.2\times10^{-3}$ *vol% and 10 mM R6G. The stripe length and width are 2.4 mm and 17 μm, respectively. The four emission spectra (black, red, blue, and green lines) measured at the pump energy of 0.5~1.0 μJ are magnified by 5 times to clearly compare them with other curves. (b) Integrated emission intensity as a function of the pump energy. The threshold pump energy is indicated by the arrow.*

Compared with dielectric nanoparticles, metal nanoparticles are of dual roles in the onset of lasing oscillation. On one hand, the intense absorption in the wavelength of

both incident light and dye fluorescence will degrade laser performance significantly, which is negligible in case of random lasers based on dielectric particles. On the other hand, the emission properties of dye molecules can be significantly modified by the proximity of silver nanoparticles. Dye molecules can either emit into free space or into surface plasmons of silver nanoparticles, in which the latter gives rise to highly localization of optical modes accompanied by a dramatic concentration of optical fields. Metal nanoplates having sharp edges and corners are thought to be most effective to enhance optical fields and generate highly localized modes. Therefore, the optical gain is greatly enhanced in the proximity of silver nanoparticles, which benefits laser performance significantly. The dynamic competition between optical absorption and SPR-enhanced optical fields dominates ultimate laser behaviors. In the present study, the laser threshold is minimum when $\rho_{Ag}=1.2\times10^{-3}$ vol%, as shown in Fig. 4.9 (b). When $\rho_{Ag}<<1.2\times10^{-3}$ vol%, optical absorption is weak, while the enhancement of optical fields is also restrained; hence the laser threshold is a slightly higher. As $\rho_{Ag}>>1.2\times10^{-3}$ vol%, optical absorption is so intense that it counteracts the enhancement of optical field caused by SPR; hence the laser threshold is high, too. The results imply that it is vital to control the concentration of metal nanoparticles in order to achieve an optimal lasing output. The influence of dye concentration on lasing threshold is also studied, as shown in Fig. 4.9 (a). The optimal dye concentration is ~10 mM, while no lasers are achieved in the shadow area. The result is understandable because low dye concentration is insufficient to produce optical gain, while excessive concentration of dye will quench the emission.

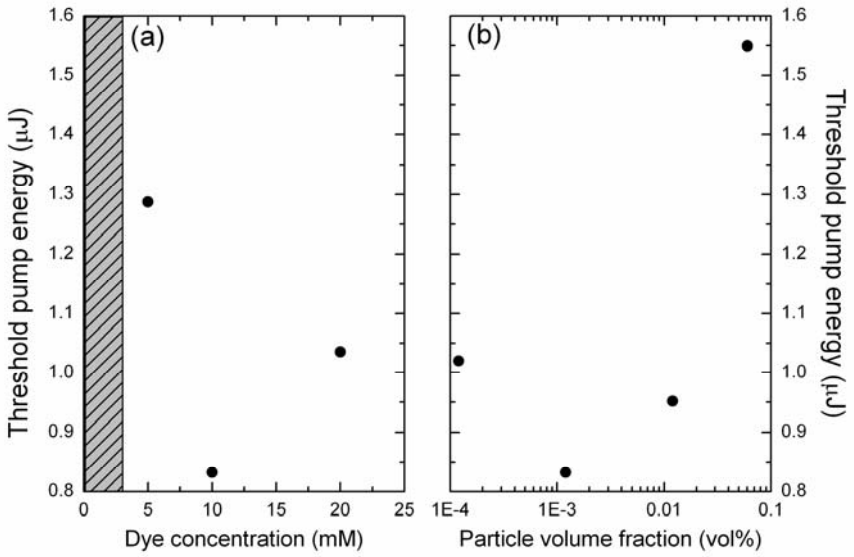

Fig. 4.9: Evolution of the threshold pump energy with the concentration of R6G (a) and the volume fraction of silver nanoprisms in the PMMA matrix (b). The stripe length and width are 2.4 mm and 17 μm, respectively.

When a screen is placed 10 cm away from the edge of the pump stripe, a bright spot appears on the screen, which indicates that the laser emission radiates unidirectionally. In order to quantitatively analyze the spatial distribution of the emission, a fiber device mounted on a three-dimensional stage was used to collect emission signals. Fig. 4.10 (a) presents the emission spectra along the stripe and θ~3°, 5°, and 8° away from the stripe, which shows that the laser emission intensity reduces dramatically with the deviation from the pump stripe and becomes almost invisible at θ~8°. The evolution of emission intensity as a function of probe angle is plotted in Fig. 4.10 (b). The unidirectional laser irradiation should be ascribed to the large aspect ratio of the pump stripe (~150), since fluorescence emitted inside the stripe obtains much larger gain from silver nanoparticles than that emitted outside the stripe. The mechanism responsible for unidirectional laser output herein resembles that responsible for the laser emission from colloidal solution of laser dye which was pumped with a circular spot on the sample surface as reported by Wu[6].

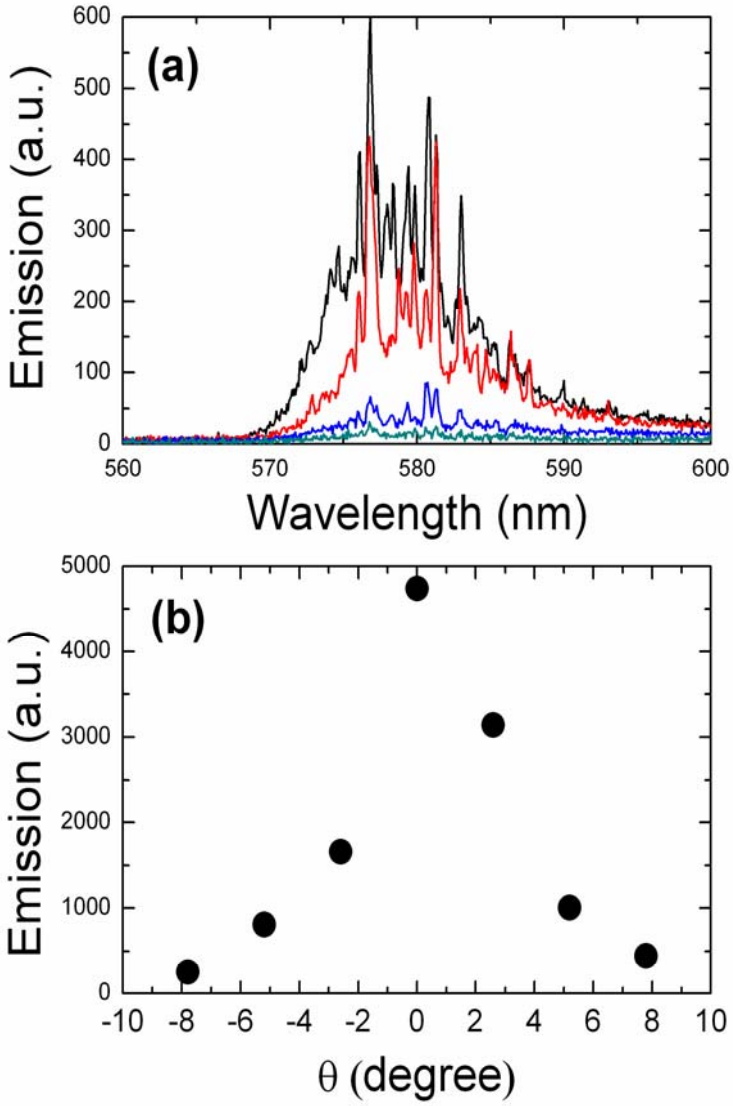

Fig. 4.10: (a) Emission spectra recorded along the pump stripe (black,) 3° (red), 5° (blue), and 8° (dark cyan) away from the pump stripe for PMMA film with $\rho_{Ag}=1.2\times10^{-3}$ *vol% and 10 mM R6G. (b) The plot of the emission intensity distribution over the probe angle. The pump stripe length and width are 2.5 mm and 17 μm, respectively.*

As mentioned above, the pump stripe length on the sample surface can be varied from 0.1 to 6 mm, which allows to study the effect of the gain length on random lasers. Fig. 4.11 (a) shows the emission spectra recorded at the stripe length of l=0.8 (black), 1.6 (red), and 2.5 mm (blue). The increase in l leads to more laser peaks accompanied by rapid increase in the emission intensity, which is because that the increase in the gain

length makes more cavity modes lasing. A redshift in the emission spectra is also observed when l is increased, which should be ascribed to the excited state absorption. Fig. 4.11 (b) displays the evolution of the threshold pump energy against l, revealing that the threshold exhibits a monotonic ascending tendency as l is increased. The fit curve follows $E_{th}=E_0 l^{\alpha}$, where E_0=1.92±0.19 and α=−1.70±0.11. The results resemble what have been observed in dielectric particles-based random lasing systems.[8]

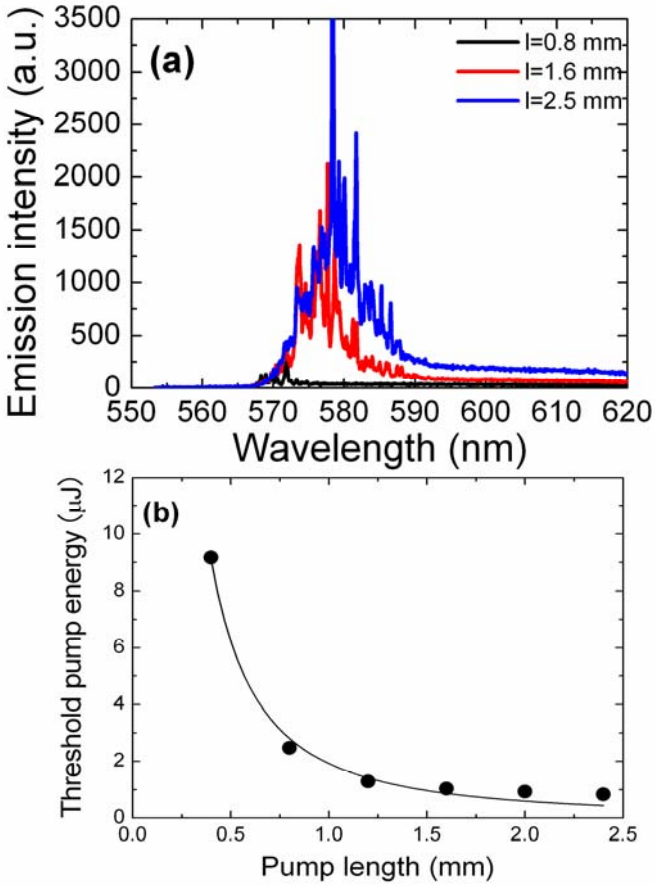

Fig. 4.11: (a) Emission spectra pumped at three stripe lengths for the PMMA film with $\rho_{Ag}=1.2\times10^{-3}$ vol% and 10 mM R6G: l=0.8 (black), 1.6 (red), and 2.5 mm (blue). The pump energy is 1.60 μJ. (b) Threshold pump energy as a function of the stripe length for PMMA film with $\rho_{Ag}=1.2\times10^{-3}$ vol% and 10 mM R6G. The solid circles represent the experimental data, while the solid line is the fit curve drawn with $E_{th}=E_0 l^{\alpha}$ where E_0=1.92±0.19; α=−1.70±0.11.

The author has conducted the same experiments as those in the PMMA films embedded with anisotropic silver nanoparticles described in section 4.3.1 to estimate the oscillation cavity length for lasing by using the power Fourier transform of single-shot emission spectrum. Fig. 4.12 shows one single-shot emission spectrum (a) and the power Fourier transform spectrum (b) derived from (a). The power Fourier transform spectrum exhibits well-separated peaks locating around 12.7, 21.3, 32.6, 40.9, and 48.2 μm. The component at 12.7 μm can be viewed as the fundamental one, while the other components at 21.3, 32.6, 40.9, and 48.2 μm are the *mth* harmonics (m=2~5). The oscillation cavity length is given by $L=\pi d_1/n$, so L=25.9 μm is obtained by using n=1.54 for PMMA. It should be noted that unstable pump source operation or strong competition between lasing modes may result in the shift in lasing frequencies for individual single-shot emission spectra, then affecting the profile of the power Fourier transform spectrum. However, the present experimental results show that the first dominant peak always exists at a position less than 15 μm. Therefore, L=25.9 μm is sufficient to estimate the oscillation cavity length. Due to the high anisotropy of silver nanoprisms, it is not suitable to estimate the scattering mean free path by taking into account the Mie scattering theory.

Interference effect plays an important role in random lasers. In the microconcept of random lasers, one should distinguish between diffusive and coherent random lasers. Sharp laser peaks exist in both cases. In amplifying random media, multiple scattering is elastic; therefore, interference effects exist and significantly affect light propagation behaviors. One can tell the interference effect by averaging the emission spectra over several laser pulses. If sharp peaks in the emission spectra are smeared out after averaging, one can describe light propagation in diffusive regime. Otherwise, if sharp peaks still remain after averaging, interference effects have a large contribution. In Polson's experiments,[2] sharp laser peaks were smoothed out after averaging over several pulses, indicating that random laser materials therein worked in a diffusive regime despite of the observations of laser peaks. However, the emission measurements over

a certain amount of laser pulses are conducted in this study, as shown in Fig. 4.13. The result indicates that sharp laser peaks still remain obviously even by averaging over 100 pump pulses. Therefore, interference effects should be taken into account in this study.

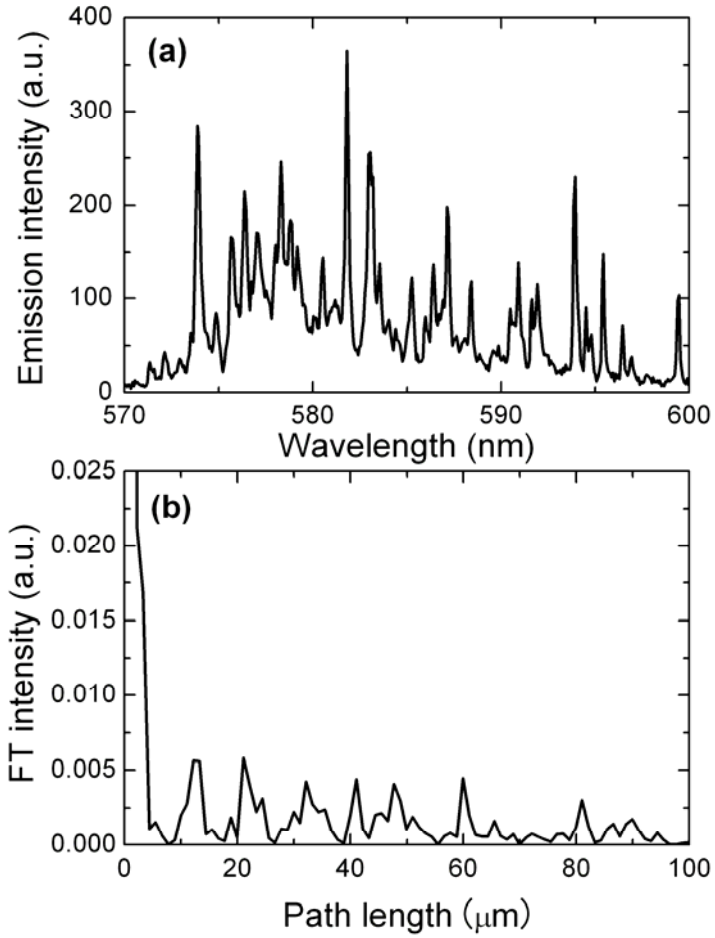

Fig. 4.12: (a) Single-shot emission spectrum for PMMA film with $\rho_{Ag}=1.2\times10^{-3}$ vol% and 10 mM R6G. (b) The power Fourier transform spectrum of the emission spectrum shown in (a). The pump energy is 1.99 μJ. The stripe length and width are 2.4 mm and 17 μm , respectively.

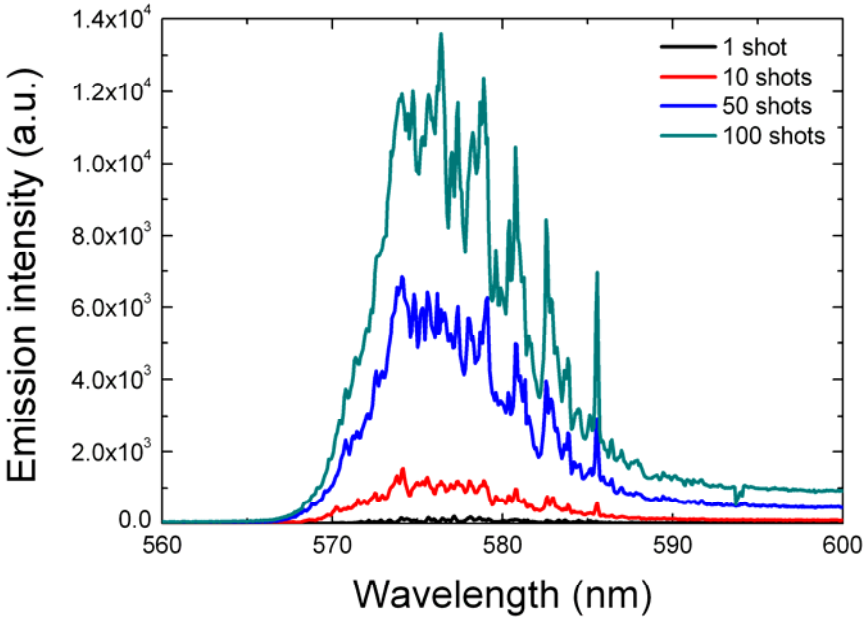

Fig. 4.13: Emission spectra by averaging over 1 shot (black), 10 shots (red), 50 shots (blue), and 100 shots (cyan), respectively. The stripe length and width are 2.4 mm and 17 μm, respectively. The pump energy is 1.99 μJ. The sample is PMMA film with $\rho_{Ag}=1.2\times10^{-3}$ *vol% and 10 mM R6G. The thickness of the PMMA film is 100 μm.*

4.3.3 *In situ* synthesized PVA-Ag-R6G films

Fig. 4.14 depicts the evolution of emission spectra as a function of the pump energy. The emission spectrum shows a broad spontaneous emission band with a linewidth of ~30 nm when the pump energy is low. When the pump energy reaches a threshold (herein 1.12 μJ), a sharp peak that centers at λ=567 nm with a linewidth of ~0.5 nm suddenly emerges on the broad ASE background. In contrast, the sample containing no silver nanoparticles merely exhibits a spontaneous emission band, indicating that silver nanoparticles have played an important role in the emergence of sharp peaks. With further increase in the pump energy, more sharp peaks are observed in the ASE background. For clear demonstration of the sharp peaks, the emission

spectra just below and above the pump threshold are inserted in Fig. 4.14. The author supposes that these peaks are really due to laser oscillation by analyzing the evolution of emission intensity as a function of pump energies that clearly demonstrates a threshold behavior, as shown in Fig. 4.15. Another evidence for lasing is the observation of unidirectional laser irradiation, as shown in the inset of Fig. 4.15, since the unidirectional irradiation is lack in the spontaneous emission. The above results resemble those previously reported random lasers with coherent feedback.[1,2] For instance, the number of laser modes is small when the pump energy is relative low since only those cavities with optical gain high enough can lase. The increase in the pump energy increases the number of lasing cavities.

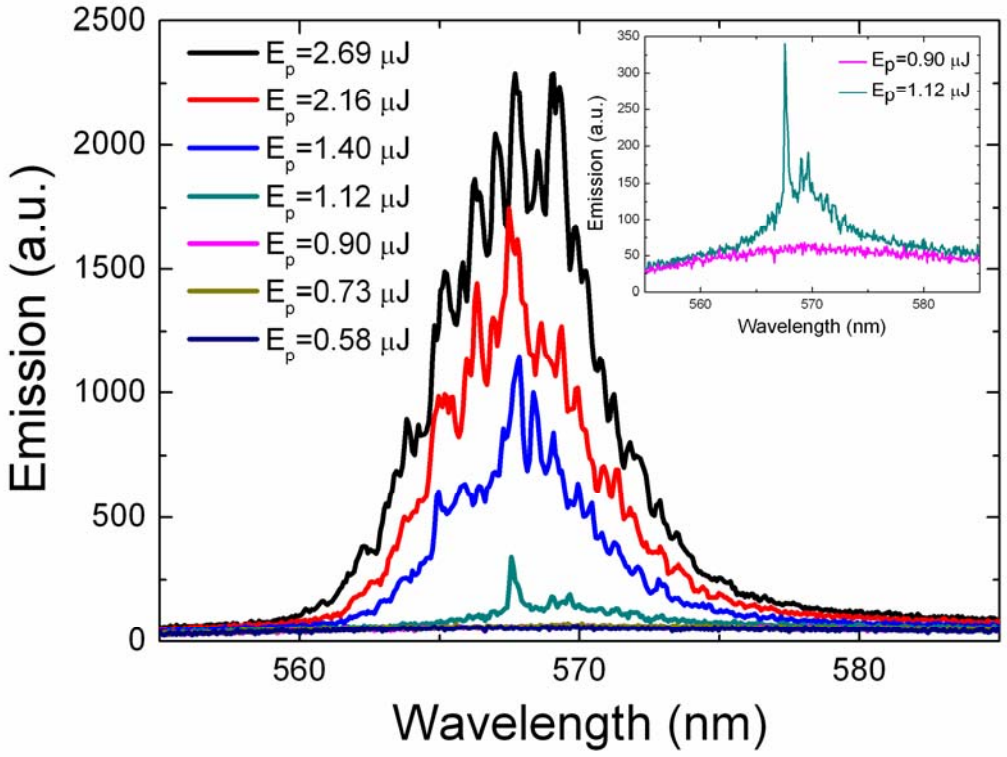

Fig. 4.14: Emission spectra as a function of pump energy for the PVA-Ag-R6G film. The inset shows the emission spectra just below and above pump threshold. The pumping stripe length and width are 2.0 mm and 17 μm, respectively.

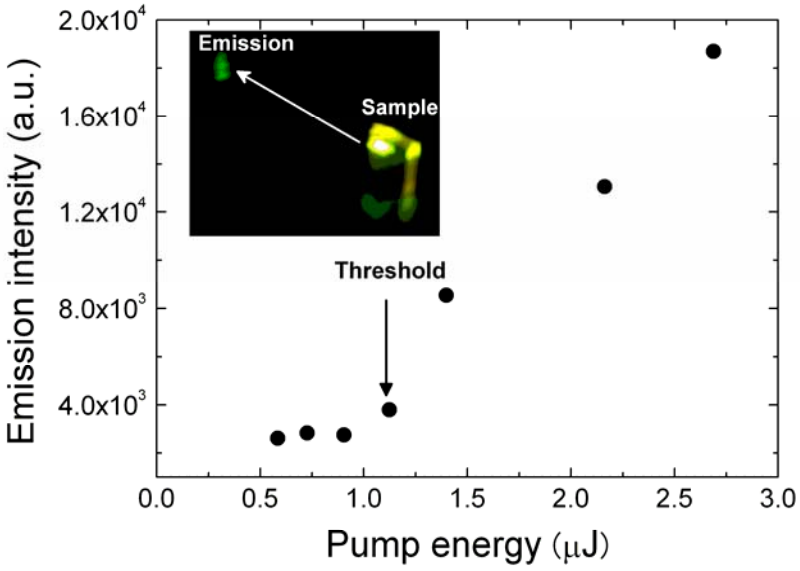

Fig. 4.15: Evolution of emission intensity as a function of the pump energy. The transition from spontaneous emission to laser irradiation is clearly indicated by the sharp increase in the slope. The inset is an image of laser emission projected on a screen 10 cm away from the sample. At left is the laser emission while the right is the sample.

The extinction cross section (σ_e) of one particle consists of σ_s and absorption cross section (σ_a); namely $\sigma_e=\sigma_s+\sigma_a$. The σ_s of one Ag nanoparticle of 1.0 nm in radius is $\sim 1.5\times10^{-24}$ while $\sigma_a \sim 5.3\times10^{-21}$ at λ=567 nm. Therefore, the scattering intensity of 1.0 nm silver nanoparticles is much weaker than the absorption intensity. However, the author has found a certain enhancement of fluorescence for all the samples containing silver nanoparticles instead of fluorescence quenching. The results indicate that the enhancement is possibly caused by SPR, as revealed previously. The scattering mean free path l_s can be estimated via the Mie theory $l_s=1/\rho\sigma_s$, where ρ is the number density of silver nanoparticles in PVA host. The ρ is calculated to be $\sim 9.1\times10^{22}/m^3$; thus l_s is

~7.3×10^3 mm. Hence, kl_s is ~1.2×10^8>>1, implying that the present system operates in extremely weak scattering regime. Although coherent feedback random lasers have been observed in dielectric based random media, the system with scattering strength as weak as that in this work has never been conducted. The author surmises that the observed lasing peaks may be associated with the highly localized optical modes due to SPR.

The present random media combine three important characteristics distinct from existing random media. First, metal nanoparticles instead of dielectric particles are used as scattering centers. Second, the size of silver nanoparticles is much smaller than the emission wavelength, which rules out the possibility of single particle as resonator. Third, the scattering strength is extremely weak, which makes polymer films highly transparent for efficiently optical excitation. Furthermore, the number density and size of silver nanoparticles relative to PVA matrix can be facilely manipulated through annealing temperature and time as well as the initial concentration of Ag^+ ions.

In summary, random lasers with coherent feedback have been observed from highly transparent polymer films embedded with silver nanoparticles. The scattering mean free path estimated by the Mie theory is ~7 orders of magnitude larger than the emission wavelength, indicating that light scattering loosely contributes to the emergence of coherent feedback. The author surmises that the observed random lasers with coherent feedback are closely associated with highly localized light modes caused by SPR interaction between silver nanoparticles and light. The author believes that this work is adding a new dimension to the fields of random lasers with metal nanostructure-based random media while further experiments should be underway in order to clarify the oscillation mechanism.

4.4 Mechanism responsible for coherent feedback

A review of light transport in disordered systems is made before discussing mechanisms responsible for coherent feedback in random lasers. Light transport in disordered systems is usually described by the model of random walk, as shown in Fig. 4.16 (a). Every step therein corresponds to the mean free path. Light arising from a spontaneous seed randomly walks in disordered media along a path 1 and obtains optical amplification during propagation. The output light may exhibit a narrowed emission band because of optical amplification to some extent. In this model, interference effects are ignored, while actually the emission spectrum is dominated by the interference effect as depicted in Fig. 4.16 (b). If light transports along a path 2, optical amplification will be constructive so that lasing oscillation takes place in the cavity. It should be noted that, even if light transports along the path 1 and walk steps are enormous (in this way, the survival photons is called lucky photons), laser peaks may appear. The scenario of the path 2 is also related to light localization, the counterpart of Anderson localization for electrons. Generally, it is believed that the light localization is responsible for the emergence of sharp peaks in strongly scattering systems. However, coherent lasers in weakly scattering systems are generally thought to be due to extended modes.

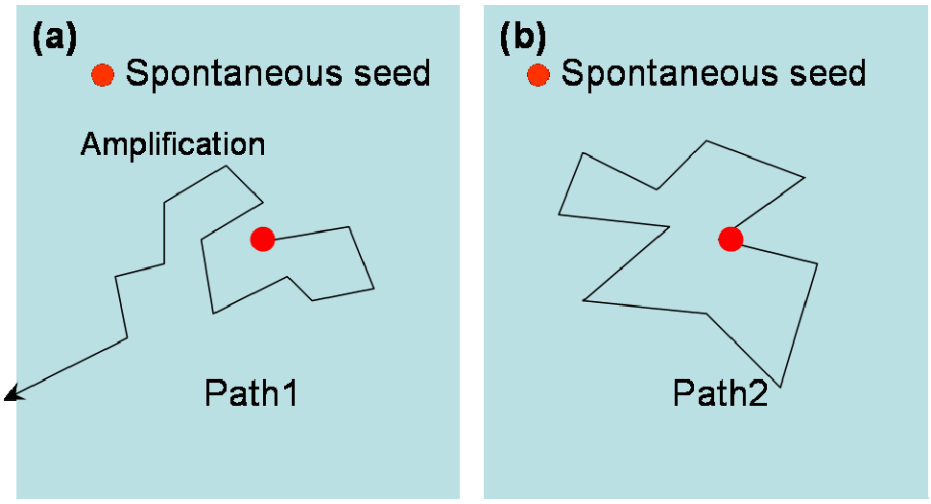

Fig. 4.16: The model of random walk of light transport in disordered system. (a) Path 1 is a diffusive process without considering interference effect but optical amplification to some extent can still be obtained. (b) Closed loop path occurs in path 2 so that interference effect has to be taken into account.

Light scattering originates from the spatial fluctuation in the dielectric constant $\varepsilon(r)$. The fluctuation strength can be described by the correlator $K(r)$ that is defined as $K(\Delta r)\equiv<\varepsilon(r)\varepsilon(r+\Delta r)>$, where $<\cdots>$ represents ensemble average. When the medium is isotropic, the width of $K(\Delta r)$ is called the correlation radius R_c. The random medium is classified into two categories: long-range disorder for $R_c>>\lambda$ and short-range disorder for $R_c\sim\lambda$. Random lasers operate in the classical optics regime for the former and in the wave optics regime for the latter. The oscillation cavity in the both cases is irregular in cavity shape which resembles that in chaotic cavity lasers. In the classical optics regime, the spatial variation of the oscillation cavity is much larger than the emission wavelength, whereas the spatial variation of the oscillation cavity is comparable or less than the emission wavelength in the wave optics regime.

In random media, when the dielectric constant varies over the length scale much larger than the emission wavelength, geometrical optics or ray optics are used to

describe the propagation of light in terms of ray trajectories. Although most of ray trajectories are chaotic and open, unstable periodic orbitals may be formed when the sample size is large enough. Such unstable periodic orbitals may trap light for a longer time than chaotic orbitals. Thus, lower optical gain is needed to realize laser oscillation in certain "scar" modes that concentrate on some unstable periodic orbitals. On the contrary, when the dielectric constant varies in a length scale comparable to or less than the emission wavelength, the propagation of light in random media can not be described in terms of ray optics. Wave optics or quantum optics is more suitable since it not only describes light scattering in short-range disorder but also takes into account the interference effect of scattered waves. The interference effect plays a critical role in light localization; even when the transport mean free path is much larger than the emission wavelength, light may be trapped partially in random media via multiple scattering and wave interference. The incomplete confinement can be compensated by photon amplification when optical gain is introduced to random media. Random lasers with coherent feedback can occur in regimes of both ray optics regime and wave optics

Random lasers studied in this thesis operate in a regime where the transport mean free path is larger than the sample size. Hence, the scattering strength of the samples in this work is rather weak. It is necessary to review existing random lasers with coherent feedback in weakly scattering regimes in order to understand the results in this work.

(1) Polson's work: interference effect[2]

The first observation of random lasers with coherent feedback in weakly scattering media was reported by Polson et al.[2] on π-conjugated films and infiltrated opals. They derived the power Fourier transform from the single-shot emission spectrum and found the oscillation length was simply related to the power Fourier transform spectrum. In addition, the ensemble-averaged power Fourier transform spectrum have not smeared out the Fourier transform components but increased the peak intensity of the Fourier

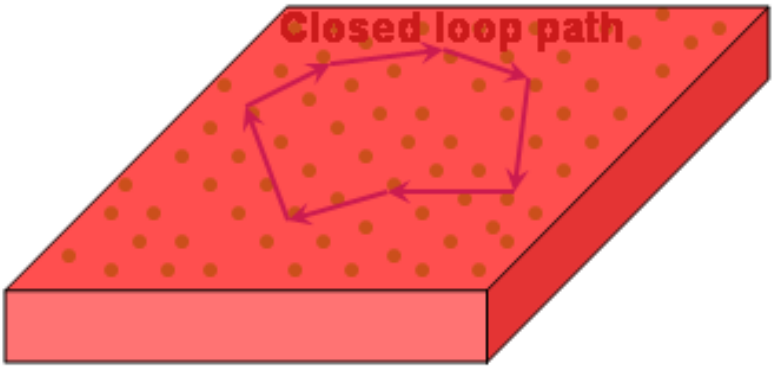

Fig. 4.17: The model of ring cavity in random media. The transport mean free path l_t and oscillation cavity length L_c should satisfy L_c~nl_t, where n is an integer.

transform components at the original positions. In their work, although the random media are weakly scattering, the scattering mean free path is still much less than the oscillation cavity length. Therefore, they proposed a model of ring cavity to interpret the emergence of random lasers with coherent feedback in weakly scattering regimes, as shown in Fig. 4. 17.

(2) Apalkov's work: almost localized modes [10]

Apalkov, Raikh, and Shapiro[10] have made a comprehensive theoretical analysis in order to understand random lasers with coherent feedback in weakly scattering systems. They propose that the lasing modes are the almost localized states in the passive medium. Such states are formed due to some rare disorder configurations that can trap light for a long time in a sub-mean-free-path region. The almost localized states are non-universal, i.e., their character and formation probability depend not only on the average strength of disorder but also on the microscopic details of disorder. They have investigated two-dimensional optically thin films in which a random resonator represents a ring-shaped area. Such a ring resonator resembles a waveguide that supports the modes of a whispering-gallery type, as shown in Fig. 4.18. The areal density of disorder-induced resonators with a high quality factor in such a film is

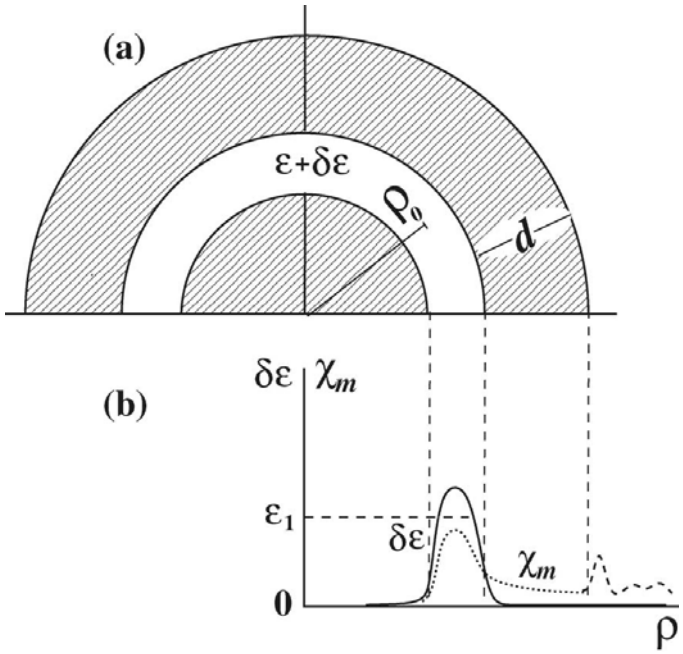

Fig. 4.18: (a) The structure of a two-dimensional resonator[10] is illustrated schematically; only half of the ring-shaped waveguide (blank region) is shown. (b) Optimal fluctuation of the dielectric constant, δε(ρ) (solid line), and the corresponding field distribution (dotted line) are shown. The dashed line outside the shaded region of a width, d, illustrates the evanescent leakage.

presented as $N_m(kl_t, Q)=N_0 exp[-S_m(kl_t, Q)]$, where k is the wavevector, l_t the transport mean free path, N_0 the prefactor, Q the quality factor. For larger R_c, $S_m \square R_c^{-2}$, thus the probability to find a random resonator increases dramatically with increasing the correlation radius of the disorder. Apalkov et al.[10] investigated the function of the random lasing threshold and predicted that the distribution of the threshold gain over the ensemble of statistically independent finite-size samples was universal. This universality stems from two results: (1) the lasing threshold in a given sample is determined by the highest quality mode of all the random resonators present in the sample; (2) the areal density of the random resonators decays sharply with the quality factor of the mode that they trap. In a two dimensional sample of an area S, the threshold excitation intensity I_{th} is given by

$$F_s(I_{th}) = \frac{\beta_s}{I_{th}} \left(\frac{I_{th}}{I_s} \right)^{-\beta_s} \exp\left[\left(\frac{I_{th}}{I_s} \right)^{-\beta_s} \right]. \quad (4.4)$$

The typical value of I_s is related to the sample area S:

$$I_s \propto \exp\left\{ -\left[\frac{\ln(S/S_0)}{G} \right]^{1/\alpha} \right\}, \quad (4.5)$$

where S_0 is the typical area of a random resonator. The parameters α and G are determined by the intrinsic properties of the disordered medium and are independent of S. The value of α is determined exclusively by the shape of the disorder correlator and G is a measure of the disorder strength.

(3) Yamilov's work: absorption induced localization[11]

Yamilov et al.[11] suggested that sharp peaks may be related to localization of light induced by absorption. This proposal arises from experimental observations that contradict the theory of almost localized states. For instance, wherever the sample is focused, lasing modes are almost spatially confined in the vicinity of the pump region. Furthermore, the lasing threshold does not fluctuate much as the pump spot moves across the entire system.

The FDTD method was used to simulate lasing in the transverse magnetic modes of two-dimensional random media. Fig. 4.19 (a) shows the Fourier transform of the electric field at the wavelength with the slowest decaying quasistate, revealing that this quasistate extends almost over the entire sample. When optical gain is introduced into the region marked by the circle in Fig. 4.19 (b), the lasing mode still extends over the entire system. This result implies that the lasing mode in an amplifying random medium is identical to an extended quasimode of a passive system, although the gain region is much smaller than the mode size. In most experiments, there is absorption outside the pumped region. This is particularly for laser dye based gain media because there is a significant overlap between absorption and emission spectra. Fig. 4.19 (c)

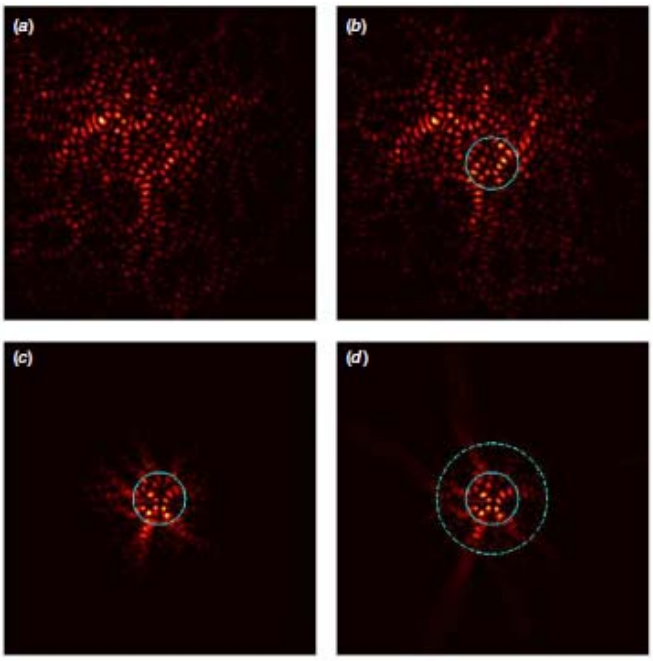

Fig. 4.19 Calculated spatial intensity distribution of (a) the quasimode with the least decay rate in a passive diffusive system, (b) the (first) lasing mode with gain inside the circular region near the centre and no absorption outside it, (c) the (first) lasing mode with gain inside the circular region near the centre and absorption outside it, and (d) the (first) lasing mode with random medium beyond one l_{abs} (dashed circle) removed. The random media are dielectric cylinders randomly placed in vacuum. The transport mean free path is $l_t \approx 1.3$ μm.

shows that the lasing mode is spatially confined in the vicinity of the locally pumped region when optical absorption is introduced into the unpumped region, revealing the emergence of a totally different mode from those in Fig. 4.19 (a) and (b). When the medium beyond one l_{abs} is removed, the lasing profile has not changed substantially, as revealed in Fig. 4.19 (d), indicating the reabsorption from the unpumped part of the sample effectively reduces the system size.

(4) Mujumdar's work: noise amplification[12]

Mujumdar et al.[12] took an opinion that sharp peaks in weakly scattering systems arose from noise amplification of photon. Such noise is frequently indicated as luck

photon, too. The sample studied therein was dye solution suspended with ZnO nanoparticles, which operated in weak scattering systems. They experimentally observed sharp peaks superimposed on the broad emission background. They modeled light transport through random amplifying media by a random walk using Monte Carlo simulation method and obtained similar results as those observed experimentally. The broad background originates from a large number of spontaneous emission events that perform a random walk and are moderately amplified, while each sharp peak corresponds to a single spontaneous emission event that experiences an extremely long light path in the sample and is consequently amplified strongly enough. Such long paths are rare and often neglected in passive disordered materials but they can dominate the emission spectrum from an amplifying disordered system. In this mechanism, shot-to-shot emission spectra should intrinsically different due to the inherent randomness in the spontaneous emission process even in static systems. Therefore, single-shot experiments are essential to observe the effect.

(5) The present work: possible surface plasmon resonance

The unique point of this work is that metal nanoparticles are used as scattering centers, which has been rarely reported previously. Sharp laser peaks in this work seem impossible to arise from closed loop path by recurrent scattering events, as described by Polson[2], since the scattering mean free path is much larger than the oscillation cavity length in our work. These sharp peaks can not be interpreted as extended modes proposed by Mujumdar[12] because these modes have not shown obviously chaotic behaviors from pulse to pulse. It is found in this work that the observed lasing modes are always spatially confined near the pump region. In addition, the lasing threshold does not fluctuate much as the pump spot moves across the entire system. The observations contradict the theory of almost localized states. Coherent feedback maybe results from localization induced by optical absorption, as proposed by Yamilov[11]. The problem is why sharp peaks can't be observed from samples

containing no silver nanoparticles if coherent feedback arises from the effect of optical absorption. The author intends to ascribe these sharp peaks to highly localized optical modes caused by SPR. One notable point in this work is that the scattering mean free path l_s is larger than the sample size L. It seems that only silver nanoparticles provide optical gain for light when light transports in such systems. The clarification of the mechanism responsible for coherent feedback needs to consider the interactions between silver nanoparticles and dye molecules by taking into account laser rate equation, which will be conducted in future work.

References

1. H. Cao, J. Y. Xu, S. H. Chang, and S. T. Ho, *Phys. Rev. E* **61**, 1985 (2000).
2. R. C. Polson, A. Chipouline, and Z. V. Vardeny, *Adv. Mater*. **13**, 760 (2001).
3. Y. Ling, H. Cao, A. L. Burin, M. A. Ratner, X. Liu, and R. P. H. Chang, *Phys. Rev. A* **64**, 063808 (2001).
4. G. D. Dice, S. Mujumdamar, and A. Y. Elezzabi, *Appl. Phys. Lett*. **86,** 131105 (2005).
5. O. Popov, A. Zilbershtein, and D. Davidov, *Appl. Phys. Lett*. **89**, 191116 (2006).
6. X. Wu, W. Fang, A. Yamilov, A. A. Chabanov, A. A. Asatryan, L. C. Botten, and H. Cao, *Phys. Rev. A* **74**, 053812 (2006).
7. S. Mujumdar, V. Turck, R. Torre, and D. S. Wiersma, *Phys. Rev. A* **76**, 033807 (2007).
8. B. Liu, A. Yamilov, Y. Ling, J. Y. Xu, and H. Cao, *Phys. Rev. Lett*. **91**, 063903 (2003).
9. R. C. Polson, G. Levina, and Z. V. Vardeny, *Appl. Phys. Lett*. **76**, 3858 (2000).
10. V. M. Apalkov, M. E. Raikh, and B. Shapiro, *Phys. Rev. Lett*. **89**, 016802 (2002).
11. A. Yamilov, X. Wu, H. Cao, and A. L. Burin, *Opt. Lett*. **30**, 2430 (2005).
12. S. Mujumdar, M. Ricci, R. Torre, and D. S. Wiersma, *Phys. Rev. Lett*. **93**, 053903 (2004).

Summary

In this thesis, fluorescence properties of glasses doped with d^0 ions and random lasing behaviors of polymer films containing silver nanostructures have been studied for a purpose of developing novel light emitting random systems. Tunable visible emissions have been observed in glasses doped with d^0 ions when excited by ultraviolet light and a near-infrared femtosecond pulsed laser, indicating potential applications in displays and nonlinear devices. Random lasers with coherent feedback have been achieved from highly transparent polymer films containing silver nanostructures for the first time. The demonstration of coherent random lasers induced by metal nanostructures is expected to open up new areas in random lasers. This thesis is summarized as follows.

In Chapter 1, the author briefly introduced fundamentals of interactions of light with matters that include light emission and absorption, multiphoton-excited fluorescence, light scattering, random lasers, and surface plasmon resonance. Light scattering can be divided into single scattering and multiple scattering. The history, development, and applications of random lasers, as well as fundamentals of light transport in amplifying random media, the effect of scattering strength on random lasers, and how to tell the coherent feedback were depicted in the section of random lasers.

In Chapter 2, the author described the sample preparation, characterization, and fluorescence properties of glasses doped with d^0 ions. Such glasses were prepared by using a conventional melt quenching method in air. Optical absorption, fluorescence, electron spin resonance, and fluorescence decays were used to characterize optical properties of d^0 ion-doped glasses. Two important observations were obtained in this work: tunable visible emissions caused by ultraviolet light excitation and tunable visible emissions induced by a near-infrared femtosecond pulsed laser excitation. The emission wavelength depends strongly on d^0 ions. The profiles of emission spectra

excited by ultraviolet light are almost identical to those excited by the near-infrared femtosecond laser for Ta^{5+}, Ti^{4+}, and Nb^{5+}-doped glasses. However, it is not the case for the other d^0 ion-doped glasses. The effect of host materials on optical properties of Ta^{5+} was examined. The results imply that the spectral profiles of optical absorption and emission were maintained but the emission intensity varies. The mechanisms for the observations of tunable visible emissions were discussed and a model of d^0 energy state responsible for such observations is proposed.

In Chapter 3, the author described the preparation and characterization of various silver nanostructures. Anisotropic silver nanoparticles and nanoprisms were prepared through sol-gel route and incorporated into polymer films using cell-casting technique. Polymer films in which anisotropic silver nanoparticles and nanoprisms were dispersed were prepared by spin coating or cell-casting technique. An *in situ* route was introduced to prepare polymer films including superfine silver nanoparticles, in which the distribution of silver nanoparticles could be easily controlled by the annealing temperature, annealing time, and initial concentrations of Ag^+ ions. The samples were characterized by optical absorption spectra, X ray diffraction, scanning electron microscopy, and transmission electron microscopy.

In Chapter 4, the author described random laser operation of three samples, i.e., polymer films containing anisotropic silver nanoparticles, polymer films including silver nanoprisms, and *in situ* synthesized polymer films with superfine silver nanoparticles. All the samples in this study are highly transparent so that the optical excitation is efficient. In other words, all the samples operate in rather weakly scattering regimes; nevertheless, coherent random lasers have been observed for all the samples. The effects of pump energy, the size of pump beam on the sample, concentration of R6G, and number density of silver nanoparticles, on properties of random lasers were discussed. The angular dependence of laser emission was examined. The Fourier transform spectrum was utilized to analyze the oscillation cavity length for lasing. The results indicate that the transport mean free path is much

larger than the oscillation cavity length, which has been rarely reported thus far. The mechanisms responsible for the coherent laser emission observed in this work were discussed. The author surmised that the lasing oscillation arises from silver nanocavities formed by surface plasmon resonance.

LIST OF PUBLICATIONS

Chapter 2

"Two-photon-excited fluorescence from silicate glass containing tantalum ions pumped by a near-infrared femtosecond pulsed laser"
Xiangeng Meng, Katsuhisa Tanaka, Shunsuke Murai, Koji Fujita, Kiyotaka Miura, and Kazuyuki Hirao
Opt. Lett. **31**, 2867 (2006).

"Intense blue emission from tantalum-doped silicate glass"
Xiangeng Meng, Shunsuke Murai, Koji Fujita, and Katsuhisa Tanaka
Appl. Phys. Lett. **89**, 061914 (2006).

"Intense greenish emission from d^0 transition metal ion Ti^{4+} in oxide glass"
Xiangeng Meng, Katsuhisa Tanaka, Koji Fujita, and Shunsuke Murai
Appl. Phys. Lett. **90**, 051917 (2007).

"Intense visible emissions from nd^0 ion-doped silicate glasses"
Xiangeng Meng, Katsuhisa Tanaka, Koji Fujita, and Shunsuke Murai
submitted to *J. Ceram. Soc. Jpn.*

"Blue emission from Ta^{5+}-doped borate glasses"
Xiangeng Meng, Shunsuke Murai, Koji Fujita, and Katsuhisa Tanaka
submitted to *Phys. Chem. Glasses*

Chapter 3

"Random lasers with coherent feedback from highly transparent polymer films embedded with silver nanoparticles"

Xiangeng Meng, Koji Fujita, Yanhua Zong, Shunsuke Murai and Katsuhisa Tanaka
Appl. Phys. Lett. **92**, 201112 (2008).

Chapter 4

"Random lasing actions in weak scattering regimes mediated by anisotropic silver nanoparticles"
Xiangeng Meng, Koji Fujita, Shunsuke Murai, and Katsuhisa Tanaka
to be submitted to *Phys. Rev. A*

"Random lasers from highly transparent polymer films containing superfine silver nanoparticles"
Xiangeng Meng, Koji Fujita, Yanhua Zong, Shunsuke Murai and Katsuhisa Tanaka
Phys. Stat. Sol. (c), in press

"Random lasers from polymer films embedded with silver prisms"
Xiangeng Meng, Koji Fujita, Shunsuke Murai, and Katsuhisa Tanaka
to be submitted to *Phys. Rev. A*

ACKNOWLEDGEMENTS

The present thesis has been carried out under the supervision of Professor Katsuhisa Tanaka at Graduate School of Engineering, Kyoto University.

The author would like to express and enlarge his deepest gratitude to his supervisor Professor Katsuhisa Tanaka for the insistent instructions in research and tremendous help in daily life. The author appreciates Professor Kazuyuki Hirao and Professor Toshinobu Yoko for carefully reading this thesis and valuable suggestions. The author is grateful to Associate Professor Koji Fujita and Assistant Professor Shunsuke Murai for their fruitful suggestions and experimental assistance in carrying out the research. Most experiments in chapter 2 of this thesis were conducted in Professor Kazuyuki Hirao's laboratory; the author appreciates Hirao group for numerous assistance during measurements.

The author thanks all the members (ever and present) in Tanaka laboratory for their care and help throughout the author's doctoral course in Japan, especially Dr. Akamatsu, Mr. Shiota, and Miss Ukon.

The author appreciates Professor Jianrong Qiu in Zhejiang University for encouragement and instructions that facilitate the author's research in Kyoto University. Also, appreciation is given to his friend Dr. Zhouen Zhang in Kyoto University who guided the author used to Japanese life.

The author is grateful to his wife Yanhua Zong for her considerations and persistent support mentally. Although they separated with each other in the author's first two years in Japan, they always understood each other and established a happy family now.

The author appreciates Japanese government for financial support (MEXT scholarship No.053242) during the doctoral course.

Finally, the author thanks his father Zhaoliang Meng and his mother Xianglan Wang for enduing the author with a fit body and active attitudes toward the world.

Xiangeng Meng in Kyoto University, 2008